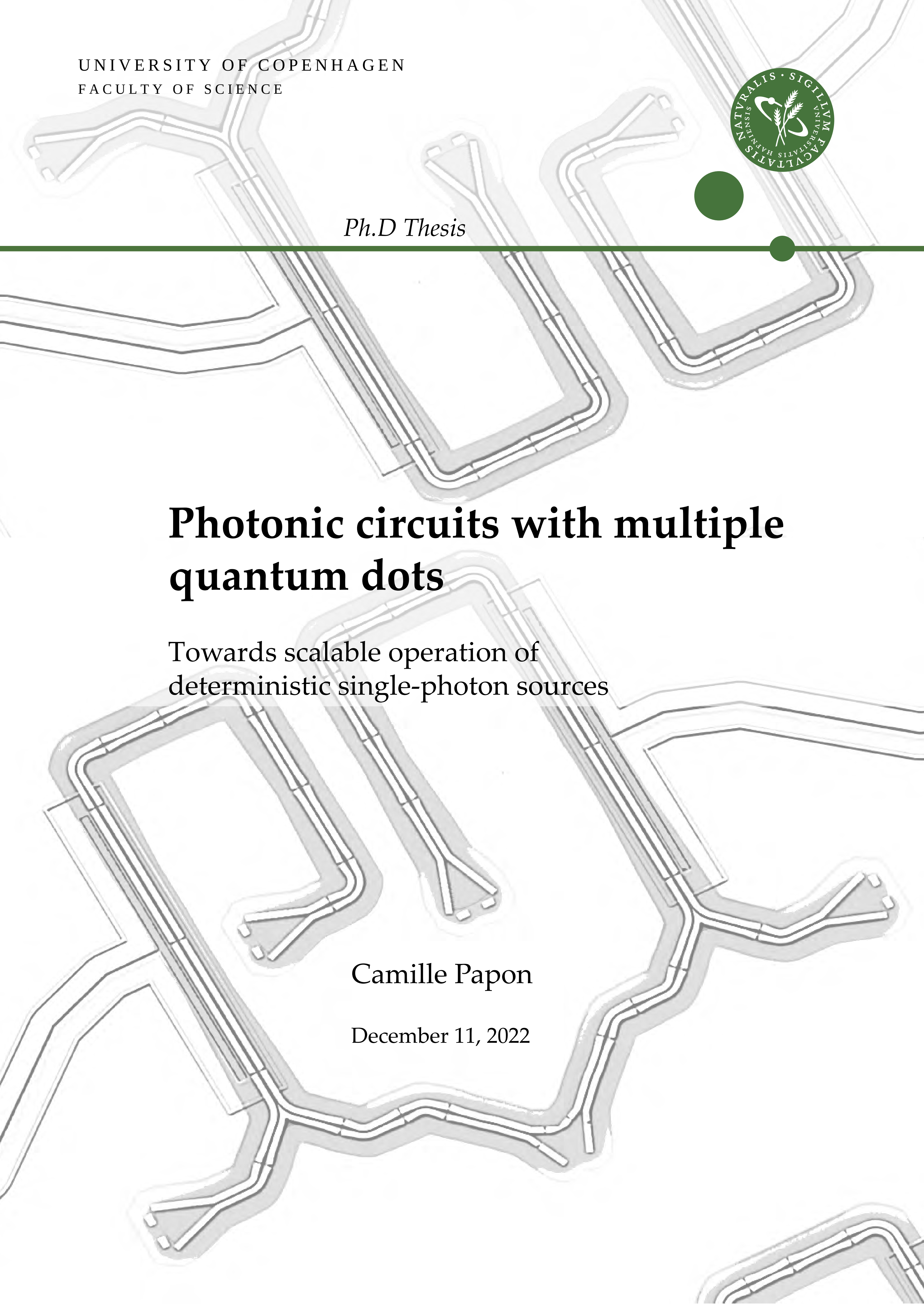

UNIVERSITY OF COPENHAGEN
FACULTY OF SCIENCE

Ph.D Thesis

Photonic circuits with multiple quantum dots

Towards scalable operation of deterministic single-photon sources

Camille Papon

December 11, 2022

Professor Peter LODAHL
Associate Professor Leonardo MIDOLO

Photonic circuits with multiple quantum dots

Towards scalable operation of deterministic single-photon sources

Camille PAPON-VEZZARO

UNIVERSITY OF
COPENHAGEN

Quantum Photonics
Center for Hybrid Quantum Networks
The Niels Bohr Institute

This thesis has been submitted to
the PhD School of The Faculty of Science
University of Copenhagen

December 11, 2022

Abstract

Single photons represent a major asset for the development of quantum technologies, owing to their compatibility with advanced photonic integrated circuits, ultimately enabling the realization of large-scale quantum processors. Generating the necessary large photonic resource requires scaling up integrated deterministic single-photon sources (SPS), a challenging task due to emitter-to-emitter disparity in wavelength and position. Here, we experimentally implement a strategy to control multiple solid-state quantum emitters directly integrated into photonic circuits, to generate multi-photon states on-chip.

More specifically, we employ low-noise InAs quantum dots (QD) integrated into p-i-n GaAs nanophotonic waveguides, which have been developed over the past few years to generate indistinguishable single photons. The strong-light matter interaction in nanophotonic structures ensures deterministic operation, leading to a high single-photon count rate. Additionally, the planar quantum photonic platform offers the opportunity to integrate the control of SPSs through dedicated circuits, ultimately enabling the realization of a multi-QD circuit.

We first demonstrate a small-scale multi-QD photonic circuit enabling the simultaneous operation of two waveguide-integrated SPSs. To do so, we make use of dual-mode waveguides, where one mode is used for excitation and the second one for collecting single photons, enabling fully waveguide-based resonant excitation and laser filtering. We optically address these two "plug-and-play" SPSs in parallel using a polarization diversity grating to perform on-chip distribution of a single laser to two QDs. The pair of quantum dots are brought into mutual resonance by applying independent bias voltages across the p-i-n diode with locally-isolated electrical contacts, thereby tuning the QDs emission wavelength individually. Each of the waveguide-integrated QDs exhibit excellent single-photon generation as characterized by $g^{(2)}(0) \ll 0.5$. Two-photon quantum interference between the two mutually resonant QDs is measured, with a peak visibility of $V = 79 \pm 2\%$, limited by imperfect laser suppression.

To overcome this limit, mainly caused by fabrication disorder, we investigate a novel scheme for preparing the mode for excitation in a dual-mode waveguide based on asymmetric directional couplers. Owing to the bi-directionality of the single-photon emission, this device represents a natural source of dual-rail encoded qubits emitted by a single QD. This is confirmed by measuring the second-order correlation at the device output ports, characterized by a $g^{(2)}(0) < 0.07$ in deterministic pulsed excitation. The results demonstrated in this thesis embody a strategy for integrating multiple quantum emitters in photonic integrated circuits, with foreseeable application in quantum simulation and quantum communication.

Sammenfatning

Enkelte fotoner repræsenterer en stor fordel for udviklingen af kvanteteknologier på grund af deres kompatibilitet med avancerede fotoniske integrerede kredsløb, hvilket i sidste ende muliggør realisering af kvanteprocessorer i stor skala. At skabe de nødvendige store fotoniske ressourcer kræver opskalering af integrerede deterministiske enkeltfotonkilder, en udfordrende opgave på grund af emitter-til-emitter-forskel i bølgelængde og position. Her implementerer vi eksperimentelt en strategi til at kontrollere flere faststof kvantemittere direkte integreret i fotoniske kredsløb for at generere multi-foton tilstande på en chip.

Mere specifikt anvender vi støjsvage InAs kvantepunkter integreret i p-i-n GaAs nanofotoniske bølgeledere, som er blevet udviklet i løbet af de sidste par år til at generere enkeltfotoner, der ikke kan skelnes. Det stærke lysstofinteraktion i nanofotoniske strukturer sikrer deterministisk drift, hvilket fører til hyppig enkelt-foton emission. Derudover muliggør den plane kvantefotoniske platform integration af styringen af enkeltfotonkilder gennem dedikerede kredsløb, hvilket i sidste ende muliggør realiseringen af et multi-kvantepunkter-kredsløb.

Vi demonstrerer først et mindre skala multi-QD fotonisk kredsløb, der muliggør samtidig drift af to bølgeleder-integrerede enkeltfotonkilder. Til dette formål bruger vi dobbelt-tilstande bølgeledere, hvor den ene tilstand bruges til excitation og den anden til at indsamle enkelte fotoner, hvilket muliggør fuldt bølgelederbaseret resonansexcitation og laserfiltrering. Vi adresserer optisk disse to "plug-and-play" enkeltfotonkilder parallelt ved hjælp af et polarisationsdiversitetsgitter, der muliggør på-chip distribution af en enkelt laser til to kvantepunkter. Parret af kvanteprikker bringes i gensidig resonans ved at anvende uafhængige forspændinger på tværs af en p-i-n dioden ved brug af lokalt isolerede elektriske kontakter, hvorved kvantepunkter emissionsbølgelængden indstilles individuelt. Hver af de bølgeleder-integrerede kvantepunkter udviser fremragende enkeltfotongenerering som karakteriseret ved $g^{(2)}(0) \ll 0.5$. To-foton kvanteinterferens mellem de to gensidigt resonante kvantepunkter måles med en maksimum synlighed på $V = 79 \pm 2\%$, begrænset af ufuldkommen laserfiltering.

For at overvinde denne grænse, hovedsageligt forårsaget af fabrikationsdefekter, undersøger vi et nyt skema til at forberede tilstanden for excitation i en dobbelt-tilstande bølgeleder, baseret på asymmetriske retningskoblere. På grund af to-direktionaliteten af enkelt-foton-emissionen repræsenterer denne enhed en naturlig kilde af dual-rail-kodede qubits, der udsendes af en enkelt QD. Dette bekræftes ved at måle andenordens korrelation ved enhedens udgangsporte, karakteriseret ved en $g^{(2)}(0) < 0.07$ i deterministisk pulseret excitation. Resultaterne demonstreret i denne afhandling repræsenterer en strategi for integration af flere kvantemittere i fotoniske

integrerede kredsløb, med forudsigelig anvendelse i kvantesimulering og kvantekommunikation.

Résumé

Les photons uniques représentent un atout majeur pour le développement des technologies quantiques, du fait de leur compatibilité avec les circuits photoniques intégrés, permettant à terme la réalisation de processeurs quantiques à grande échelle. Pour générer la large ressource photonique nécessaire, il est donc fondamental d'intégrer à large échelle des sources de photons uniques efficaces, une tâche difficile en raison de la disparité entre les émetteurs, en longueur d'onde et en position. Ici, nous mettons en œuvre expérimentalement une stratégie pour contrôler plusieurs émetteurs quantiques à l'état solide, directement intégrés dans des circuits photoniques semiconducteurs, pour générer des états photoniques multiple sur puce.

Plus précisément, nous utilisons des boîtes quantiques faîtes d'InAs, caracterisées par leur faible bruit, intégrées dans des guides d'ondes nanophotoniques, fabriqués dans une diode *p*-*i*-*n* de GaAs, qui ont été développés au cours des dernières années pour générer des photons uniques indiscernables. La forte interaction lumière-matière dans les structures nanophotoniques assure une large émission de photons uniques, conduisant à de brillantes sources. De plus, la plateforme photonique quantique planaire offre la possibilité d'intégrer le contrôle des sources de photons uniques à travers des circuits dédiés, permettant à terme la réalisation d'un circuit comprenenant multiple boîtes quantiques.

Nous réalisons d'abord un circuit photonique à boîte quantique multiples à petite échelle, permettant le fonctionnement simultané de deux sources de photons uniques intégrées dans un guide d'ondes. Pour ce faire, nous utilisons des guides d'ondes bi-modaux, où un mode est utilisé pour l'excitation de la boîte quantique et le second pour la collecte des photons uniques, permettant ainsi une excitation résonante et un filtrage du laser entièrement basés sur des systèmes photoniques. Nous adressons optiquement ces deux sources de photons uniques "plug-and-play" en parallèle à l'aide d'un réseau à diversité de polarisation qui permet la distribution sur puce d'un seul laser à deux boîtes quantiques. La paire de boîtes quantiques est mise en résonance mutuelle en appliquant des tensions indépendantes à travers la diode *p*-*i*-*n* avec des contacts électriques localement isolés, controllant ainsi individuellement la longueur d'onde d'émission des boîtes quantiques. Chacune des boîtes quantiques intégrées au guide d'ondes présente une excellente émission de photon unique, caractérisée par $g^{(2)}(0) \ll 0.5$. L'interférence quantique à deux photons entre les deux boîtes quantiques, mutuellement résonnantes, est mesurée, avec une visibilité maximale de $V = 79 \pm 2\%$, limitée par la suppression imparfaite laser.

Pour surmonter cette limite, principalement causée par le désordre dû à la fabrication, nous étudions un nouveau schéma de préparation du mode d'excitation dans un guide d'onde bi-modal, basé sur des coupleurs directionnels asymétriques. En raison de la bi-directionnalité de l'émission de photons uniques, ce dispositif représente une source naturelle de bits quantiques codés dans le chemin du guide d'onde emprunté par le photon unique. Ceci est confirmé en mesurant la corrélation de second ordre à la sortie des deux chemins du système, caractérisée par $g^{(2)}(0) < 0.07$ en excitation pulsée. Les résultats démontrés dans cette thèse incarnent une stratégie pour l'intégration de multiples émetteurs quantiques dans des circuits intégrés photoniques, en vue d'applications dans le domaine de la simulation quantique et la communication quantique.

Acknowledgements

This thesis is the final output of the research conducted for the past three years (and a little bit more) in the Quantum Photonics group at the Niels Bohr Institute, under the supervision of Professor Peter Lodahl and Associate Professor Leonardo Midolo. Over these years, I had the rare chance to deepen my knowledge in quantum optics, play with the fabrication of quantum photonic devices, learn from the best experimentalists how to tame optical setups, and grow as a person in the most inspirational environment.

For this scientific and human adventure, I sincerely thank all the people who accompanied me along the way.

I will start by thanking my supervisor, Peter, for allowing me to pursue the journey of a Ph.D. His sharp inputs to this project were highly formative, and his dedication to growing a quantum ecosystem is a true inspiration. I am deeply grateful to my co-supervisor, Leonardo, for inspiring this project and guiding me to make it my own. Through his creative and visionary mind, he is a real model of the scientist I would like to become. Thank you for your unconditional support all these years, you have truly helped me to shape a path for myself.

If I can present the results of this thesis, it is only thanks to the knowledge and the help that exceptional researchers shared with me. My deepest gratitude goes to Ravitej Uppu, for introducing me to the secrets of quantum dot spectroscopy and to the curiosity of solving problems. His passion for science has been a real motivation for me. I am thankful to the Source team-affiliated, Freja Thilde Østfeldt, Cecilie Toftdahl Olesen, Ying Wang, and Mikkel Mikkelsen for sharing the excitement about single photons and the tears from the 1.6K cryo altogether. My heart goes to the Fab team, past and present members, Tommaso Pregnolato, Ying, Zhe Liu, Aslı Dilara Uğurlu, Atefeh Shadmani, Celeste Qvotrup, along whom I learned fabrication skills and the pure meaning of magic. I tried to tell part of this never-ending story in Chapter 3. I am particularly indebted to Ying and Zhe for fabricating the samples presented in Chapters 4 and 5 after I left the cleanroom. None of these experiments would be possible without the excellent wafer material grown by Sven Scholz, in the group of Arne Ludwig and Andreas Wieck, University of Bochum. The measurements in Chapter 4 were conducted in a Corona time where the lab was depopulated, except for Alexey Tiranov, whom I thank for helping me in all my lab struggles. Finally, my deepest gratitude to Ying, Zhe, Alexey, and Leonardo for helping me shape this thesis in the best way.

I cannot stop without writing out loud how grateful I am for spending so many years in a community of people being thoughtful about each other, committed to creating an inclusive environment, and sharing the fun and tough times of doing science in solidarity. This goes beyond the border of the Quantum Photonics group and pertains to the Quantum Optics section as a whole, past and present members. My heartful thanks to Vasiliki Angelopoulou, for the trusted discussions, to Nils Hauff and Ming-Lai Chan, for being my Ph.D twin brothers, to Eva M^{a} González Ruiz, for being my bimbo, always, (and answering my quantum interference questions), to Carlos Faurby, for making people feel valued, to Patrik Sund, for never being short on facts and arguments, to Yijian Meng, for being so chill about everything, to Lucio Stefano, for his peaceful vibe, to Martin Hayhurst Appel, for singing under my window. My warmest thanks to Sjaak Van Diepen, Rodrigo Thomas, and Mads B. Kristensen, for making our office a safe haven of empathy. I would also like to express my gratitude to Anders S. Sørensen, for fostering diversity of opinions in the section, since he became its leader. To Hanna Le Jeannic, Xiaoyan Zhou, Vincent Elfving, Yegishe Tsaturyan, Nenad Krajl, Konstantin Tiurev, Yannick Seis, Arianne Brooks, and Beatrice Da Lio, thank you for the legendary times together. I am grateful to Thibault Capelle, for being such an inspiring friend. Thank you, Suzanne Clavairoly, for trying to teach me time management. The lunches with Raphaël Daveau these last years were true moments of sharing. To Maxime Bergamin, I thank you and Hermine for your sincere support throughout my writing time, once again. I am sorry that I probably skipped names, but please trust me that evolving into this vivid group of people has been a unique experience, which makes me the lucky one.

The time up to bringing a final end to this adventure has been challenging at times, but never ever have I felt alone facing it. I could not have done it without the bright presence of Aslı in my reality. Thank you for sharing your strength with me. To Stella, for standing by my side all these years, no matter what. To Bach Mai, your precious friendship suffers no distance. To the home base, *le socle*, Clotilde, Lorine, Baptiste, Pierre, Michaël, and Valentin, you are my pillars and make it all worthwhile. To my family, my parents, Magali and Christophe, and my brother, Axel, I feel your love and support no matter the kilometers. Thank you for believing in me unconditionally, you are the very reason I can travel this path. Alexey, sharing this life with you makes every single moment light and meaningful. Thank you for making me feel so brave.

Dans un jardin de rose, d'olivier et de bouleau

List of publications

The articles that have been published during this thesis are listed in chronological order.

Journal publications

A R. Uppu, F. T. Pedersen, Y. Wang, C. T. Olesen, C. Papon, X. Zhou, L. Midolo, S. Scholz, A. D. Wieck, A. Ludwig, & P. Lodahl, **“Scalable integrated single-photon source”** Science Advances 6, eabc8268 (2020)

B Y. Wang, R. Uppu, X. Zhou, C. Papon, S. Scholz, A. D. Wieck, A. Ludwig, P. Lodahl, & L. Midolo, **“Electroabsorption in gated GaAs nanophotonic waveguides”** Applied Physics Letters 118, 131106 (2021)

C A. Shadmani, R. A. Thomas, Z. Liu , C. Papon, M. Heck, N. Volet, S. Scholz, A. D. Wieck, P. Lodahl, & L. Midolo,**“Integration of GaAs waveguides on a Silicon substrate for quantum photonic circuits"** Optics Express 30, 37595-37602 (2022)

D C. Papon, Y. Wang, R. Uppu, S. Scholz, A. D. Wieck, A. Ludwig, P. Lodahl, & L. Midolo, **“Independent operation of two waveguide-integrated single-photon sources”** arXiv:2210.09826 (2022) (under peer-review)

Conference publications

E C. Papon, Y. Wang, R. Uppu, S. Scholz, A. D. Wieck, A. Ludwig, P. Lodahl, & L. Midolo, **"Quantum Interference between Integrated and Independently Controlled Quantum Dots"** , CLEO San José 2022

F L. Midolo, C. Papon, X. Zhou, R. Uppu, Y. Wang, S. Scholz, A. D. Wieck, A. Ludwig, & P. Lodahl, **" Scalable Quantum Dot Single-photon Sources Based on Dual-mode Waveguides "** , CLEO Pacific Rim 2022

Summer school

G Poster presentation, **Cargese School of Quantum Information and Quantum Technology**, June 2021

Seminar talks

H **"Circuit-based resonant excitation of multiple quantum dots"** MIT's Optics and Quantum Electronics Seminar 2022

I **"Scalable operation of two waveguide-integrated single-photon sources"**Quantum Light Control Lab seminar, Iowa University 2022

J **"Quantum emitters in coupled nanostructures: towards scaling single-photon sources on a chip"**, Hybrid Quantum Center retreat 2020

Outreach

K **"Video: mit PhD-projekt"** Video-KU

L **"Physicists criticise University of Copenhagen's new NATO ties"** Uniavisen

Contents

Multi-photon states for quantum information applications

The interplay between the fundamental research on Nature and the development of new technologies has played a crucial role in the shaping of today's societies and constantly brings promises of life quality improvements. Rightfully, modern electronics, based on semiconductor devices, and compact lasers used for high-speed communication, to name a few, are all based on the fundamental understanding of atoms, electrons, and photons behavior within the realm of quantum mechanics, initiated in the early XXth century.

Towards the 1980s, the fact that particles follow the superposition principle and may share non-classical correlation by entanglement was not a secret anymore. Bold physicists saw an opportunity to use the quantum systems as carriers of quantum information, called qubits (Feynman 1982). These qubits can be used in a processor or a quantum computer and solve problems intractable by classical computers. Numerous quantum algorithms were devised, such as the search algorithm (Grover 2001), the first quantum-based algorithm showing superpolynomial speed-up factorization in prime numbers (Shor 1997), and algorithms to simulate the dynamics of other quantum systems.

Perhaps one of the highest expectations of this decade resides in quantum technologies and in how quantum computing will solve long-standing challenges within life science and chemistry (Preskill 2022). This promise is what feeds the "quantum optimism", going way beyond scientific curiosity, as can be seen from government investment plans (Acín et al. 2018) and interest from the business world (Chow et al. 2022). It is still being determined which problems within quantum chemistry will be solved with exponential advantage (Lee et al. 2022) and which hardware will unleash this potential. However, here are a few things we can be sure about.

Single photons, fundamental light quanta, will play a significant role in developing quantum technologies. This is because of their property of carrying quantum information in different degrees of freedom and propagating efficiently without decoherence (O'Brien et al. 2009). They fulfill several of DiVincenzo's criteria for being compatible with constructing a quantum computer (DiVincenzo 2000), including a well-defined two-level system and single-qubit gate. However, the weak photon-photon interaction prohibits two-qubit gates for fully circuit-based computation. Luckily, schemes based on linear optics (Knill et al. 2001) enable universal quantum computing with a network of interferometers and phase shifters combined with detection. Multi-photon interference is also the testbed of quantum advantage over classical computers with specific tasks, such as boson sampling, a problem known to scale exponentially on a classical computer (Zhong et al. 2020; Madsen et al. 2022). Moreover, photons can form larger entangled states through light-matter interaction with quantum emitters or via the heralded scheme, representing a fantastic resource for measurement-based quantum computation (Raussendorf et al. 2001; Nielsen 2004).

Quantum computation nodes can be linked through the quantum internet (Kimble 2008), in analogy with high-speed classical communication over modern optical fiber networks, by distributing quantum information with single photons. However, unavoidable losses in optical fibers lead to the destruction of quantum information, which cannot be amplified due to the no-cloning theorem. Quantum repeaters provide a solution to this challenge by using entangled photonic states to transfer quantum information over large distances (Briegel et al. 1998). Moreover, single photons enable quantum cryptography through quantum key distribution protocols (Bennett 1984). It is an answer against the threat from a quantum computer to break the RSA algorithm, whose security is based on prime numbers factorization. Ultimately unbreakable security channels are possible with entangled photonic states with device-independent quantum key distribution (Acín et al. 2007).

Full-scale realization of quantum information applications requires a large number of photonic qubits, with a formidable scale of up to a million for full fault-tolerant quantum computing (Rudolph 2017), and a strong-light matter interaction with matter qubits. Solid-state quantum emitters can deterministically generate single photons directly on a chip, with prospects of scalability (Aharonovich et al. 2016). Among promising single-photon emitters lie quantum dots, artificial atoms grown in a semiconductor host material. Optimization of photonic structures integrated with the quantum dots enables deterministic light-matter interaction, providing a mature platform for the efficient generation of pure single photons (Lodahl et al. 2022). The high quality of the quantum dot growth and the control over the charge environment for low decoherence leads to the efficient emission of indistinguishable photons. Moreover, quantum dot states possess a spin, enabling deterministic light-matter entanglement (Warburton 2013). Quantum dots and the deterministic interaction with single photons, therefore, represent the cornerstone of advanced quantum networks (Buterakos et al. 2017; Borregaard et al. 2020).

Parallelly, maturing photonic integrated circuits led to the miniaturization and integration of thousands of optical components, making the control of photonic states scalable (Wang et al. 2020). Recent years have seen several demonstrations of the positive impact of quantum photonic integrated circuits (QPIC) on quantum information applications (Peruzzo et al. 2014; Huh et al. 2015; Sparrow et al. 2018), with on-chip processing (Carolan et al. 2015; Harris et al. 2017) and integrated detectors (Lomonte et al. 2021). However, most of the experiments involving multi-photon states have relied on probabilistic spontaneous-down conversion single-photon sources, with a low generation efficiency by nature, which in the long run, constraints the achievable size of the quantum processor. Therefore, advancing complex quantum information applications based on photonic quantum states requires interfacing multiple bright deterministic single-photon sources with photonic integrated circuits (Uppu et al. 2021; Moody et al. 2022; Li et al. 2022).

Significant challenges have so far hindered the large-scale integration of multiple quantum dots in photonic circuits. The main roadblocks are the random position of quantum dots in the chip, the disparate emission wavelength between emitters, called the inhomogeneous broadening, and uncorrelated slow noise processes due to the solid-state environment of each quantum dot (Vural et al. 2020). Moreover, developing a genuinely scalable photonic platform also demands integrating control over multiple single-photon sources in the circuit, where a viable strategy has yet to be formulated.

Is it then too unrealistic to envision multiple quantum emitters integrated and operated on the same photonic platform? In the present thesis, we demonstrate that specifically designed photonic circuits enable the control of multiple mutually resonant quantum dots. Developing such a strategy is a key enabling functionality towards the large-scale integration of deterministic single-photon sources in a QPIC, as depicted in Fig. 1.

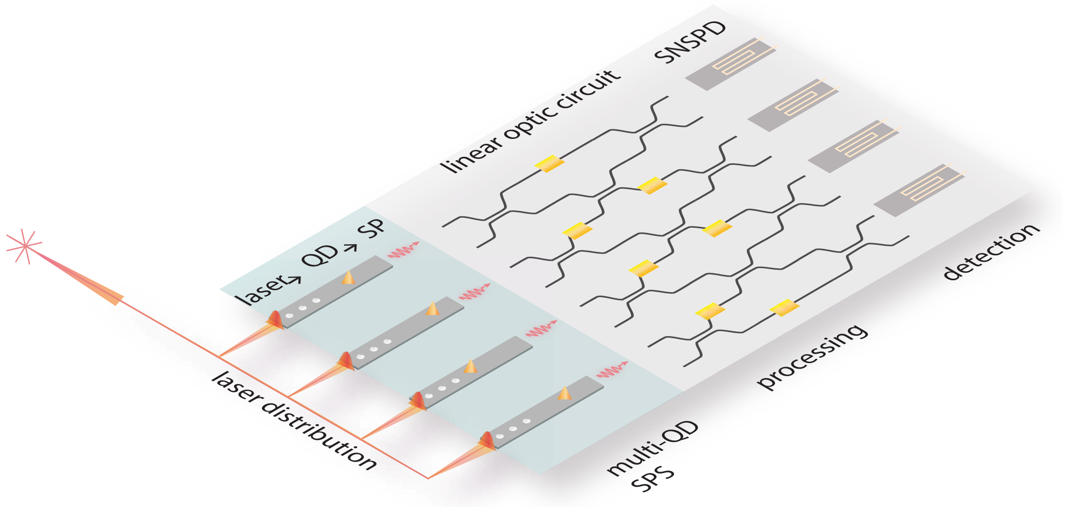

FIGURE 1: A quantum photonic integrated circuit with a multi-quantum dot (QD) single-photon source (SPS). Interfacing multiple deterministic SPSs operated simultaneously with a photonic integrated circuit, which performs on-chip processing and detection, will usher in a new era of advanced quantum information applications. This thesis aims to demonstrate scalable methods to excite multiple waveguide-integrated QDs.

To this end, we focus on developing nanophotonic devices enabling simultaneous resonant excitation of multiple waveguide-integrated quantum dots. We employ the waveguide-assisted excitation technique (Uppu et al. 2020a) as a scalable method for integrating laser distribution and filtering as a part of the photonic circuit. Moreover, electrical access allows to individually frequency-tune quantum dots through the DC-Stark shift, mitigating the effect of inhomogeneous broadening. We successfully apply this strategy to the simultaneous operation of $N = 2$ single-photon sources and lay a roadmap for next-generation multi-QD circuits.

More precisely, the thesis is built on the following layout:

- Chapter 1 covers the optical properties of self-assembled InAs quantum dots in GaAs, the quantum emitter investigated throughout this thesis. We also outline the theory of resonance fluorescence of a two-level system to describe the properties and statistics of the emitted photons.
- Chapter 2 introduces nanophotonic devices for realizing deterministic light-matter interaction and, more specifically, details the waveguide-assisted device enabling circuit-based resonance fluorescence.
- Chapter 3 gives an overview of the nanofabrication techniques and challenges to realize scalable quantum photonic circuits. We then highlight specific designs developed for multiple single-photon sources of excitation.
- Chapter 4 demonstrates the simultaneous resonant excitation of two waveguide-integrated quantum dots and the two-photon quantum interference between the resonant pair.
- Chapter 5 focuses on the characterization of an improved device for circuit-based resonant excitation using an asymmetric directional coupler. We finally introduce few-photons applications for generating two-photon heralded entanglement.
- Finally, Chapter 6 contains conclusive remarks and outlook to further research directions.

1 Quantum optics on a chip

Single photons are fundamental elements of the larger infrastructure of quantum technologies, as they can be used advantageously in the different applications of quantum mechanics, in quantum communication, quantum cryptography, or quantum simulation (Flamini et al. 2018). Pioneer experiments testing the laws of quantum mechanics used single photons emitted by atoms and ions (Aspect et al. 1982), which requires resource-demanding methods for trapping and controlling these species, limiting the system's scalability. Development in the heterogeneous growth of III-V semiconductors led to the fabrication of *quantum dots*, which are a few tens of nanometer-scale assemblies of matter featuring three-dimensional quantum confinement and quantized energy level (Arakawa et al. 2020). These solid-state quantum emitters, naturally trapped on a chip, present excellent atom-like optical properties, as described in this chapter. We will review the main results of resonance fluorescence of a two-level system which are necessary to explain the quantum dot optical transition. Finally, we will introduce the noise sources inherent to the solid-state platform and a way to remediate them.

1.1 Light emission in III-V semiconductors

III-V semiconductors are constituted of a crystal assembly of atoms from the third and fifth group of the periodic table, where each atom shares two electrons of opposite spin with its nearest neighbors. An extensively studied semiconductor is GaAs, owing to its high electronic mobility (Sze et al. 2007). The resulting covalent bonds between the atoms of gallium and arsenide follow a disposition called the zincblende primitive cell, showed in Fig. 1.1(a), where each specie follows a face-centered crystal cell that is shifted in space and is common to most of the III-V materials. In real space, a distinctive metric of the crystal structure is the lattice constant a, the distance after which the disposition of atoms repeats itself. This simple parameter has a significant implication for predicting which semiconductors can be grown epitaxially since a too large lattice mismatch will induce strains and defects in the crystal. The relaxing strain can be used advantageously, as we will see in the next section.

In reciprocal space, the primitive cell of the zincblende lattice takes the form shown in Fig. 1.1(b), called the first Brillouin zone, which follows a body-centered cubic lattice. It is centered at $\Gamma = (0, 0, 0)$ and the main axis

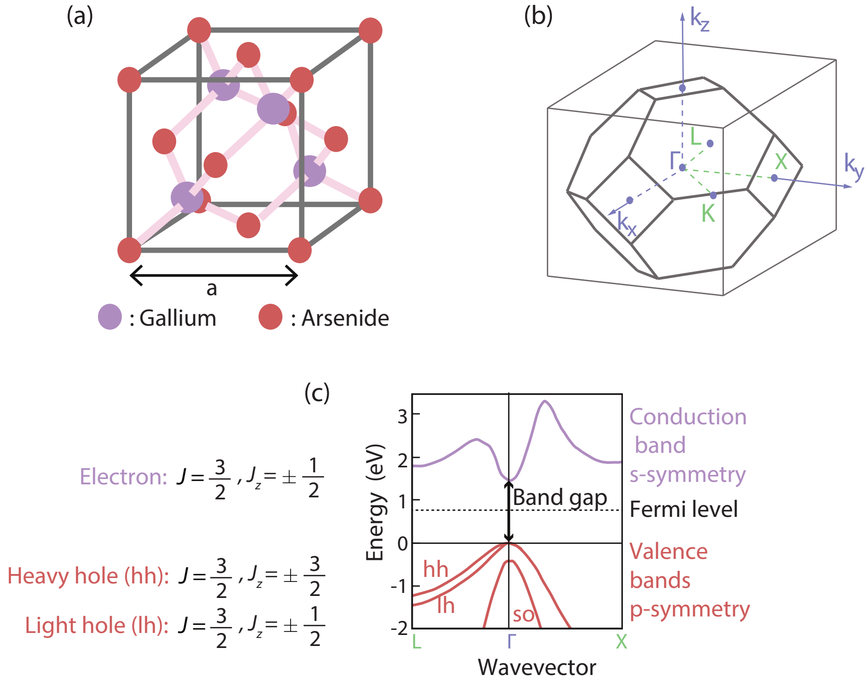

FIGURE 1.1: Crystal structure of Gallium Arsenide. (a) GaAs crystallize in a zincblende lattice like many of the III-V semiconductors. The lattice constant a is the minimum separation between the repeated assembly of atoms. (b) First Brillouin zone in reciprocal space, showing the main symmetry points (c) Dispersion of electrons in bulk GaAs gives rise to an energy band diagram, where the valence band is filled with electrons, and the conduction band is empty. The direct bandgap at the Γ-point ensures that a photon can be emitted. The total angular momentum J and projection quantum number J_z of the different bands are shown. All figures are adapted from (Sze et al. 2007).

and points of the reciprocal lattice are shown, which are bounded by a cube of the edge of $\frac{4\pi}{a}$ (Kittel 2005). Understanding the energy-momentum relationship of carriers in semiconductors is essential to understand their optical properties, which can be done by solving the Schrödinger equation for a periodic potential. As an example, the energy-band structure of GaAs is shown in Fig. 1.1(c) (Sze et al. 2007). The first striking feature is the presence of a range of energies for which no charge state is allowed, called the *energy band gap*, which is around $E_g = 1.42$ eV at room temperature for GaAs. The presence of this band gap is a feature characterizing all semiconductors.

Charge states are then arranged in bands of two types, called the *valence band* (bottom) and the *conduction band* (top). The valence band is filled with electrons and only participates in conduction when an electron is removed from this band and is promoted to the conduction band. This event leaves a *hole* behind in the valence band, which is a quasi-particle with a positive charge. The conduction band is, in general, empty and can be populated by excited electrons. In an intrinsic semiconductor characterized by the absence of extra doping species, the Fermi energy is located between the valence band's maximum and the conduction band's minimum. A particular feature of the valence band is the presence of three bands, where two degenerate at the Γ-point, the heavy hole (hh) and the light hole (lh). The third one, called the split-off (so) band, is shifted down in energy due to spin-orbit coupling.

While the full description of the band diagram is complex, the behavior of particles close to the Γ-point can be well explained by a free electron model $E(k) = \frac{\hbar^2 k^2}{2m^*}$. There different effective masses $m^* = \hbar^2 \left(\frac{d^2 E}{dk^2}\right)^{-1}$ proper to each quasi-particle, the electron, the heavy hole, and the light hole are used. A particular feature of GaAs is that the minimum of the conduction band is aligned at the Γ-point with the maximum of the valence bands, a configuration called *direct* bandgap. In this way, a photon can be emitted efficiently without exchanging momentum after the promotion of an electron from the valence band to the conduction band, leaving a hole behind and forming an electron-hole complex. Contrarily to Si, which is an indirect band gap semiconductor, GaAs possesses active optical properties, making it an interesting optoelectronic material. Moreover, combining direct bandgap semiconductors in heterostructure leads to the modification of the density of electronic states, such as in quantum well, and is the fundamental working principle of today's diode lasers. If chosen wisely, the heterostructure of semiconductors can lead to full quantization of the charge states in a semiconductor.

1.2 Quantum dots and their optical properties

The light emission properties of direct band gap semiconductors have been exploited extensively to create classical states of light. Non-classical states of light can also be created by using heterostructures of semiconductors and creating solid-state quantum emitter in the form of *quantum dot* (QD).

1.2.1 Self-assembled quantum dots

A well-studied example is the InAs quantum dot embedded in GaAs, which is grown by ultra-high quality epitaxial growth (Bart et al. 2022) in a molecular beam epitaxy chamber. Due to the smaller band gap of InAs compared to GaAs, the electronic potential is confined in three dimensions. It gives rise to discrete energy levels, which grant QDs similar optical properties as atoms, although composed of a tenth of thousands of atoms. As described in Fig. 1.2(a), InAs is grown on GaAs, and due to the 7% lattice mismatch, the strain will release in the shape of islands after the growth of a monolayer of InAs called the wetting layer. This self-assembled growth method, the Stranski-Krastanov technique, leads to randomly positioned quantum dots. A capping layer of GaAs further terminates the growth.

Looking at the energy landscape along the growth direction, shown in Fig. 1.2(b), we see that the three-dimensional confinement leads to the quantization of electron and hole states in the quantum dot. The state lowest in

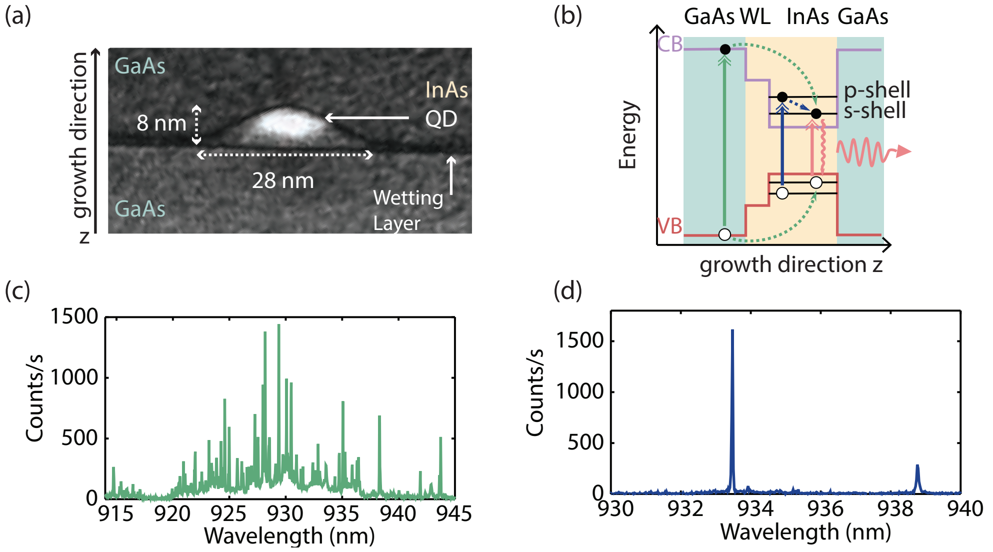

FIGURE 1.2: Self-assembled InAs quantum dots (QD). (a) Transmission electron microscope image of a QD. InAs QDs nucleate randomly on top of a GaAs substrate due to lattice mismatch and are further capped by GaAs. Adapted from (Zabel et al. 2013) (b) Three-dimensional confinement of the electronic potential in InAs surrounded by GaAs leads to quantized energy levels. An exciton is created when an electron is trapped in the lowest conduction band and a hole in the highest valence band. Different optical excitation is possible, but direct resonant excitation leads to the most coherent emission. c) Spectrum of excitonic transitions excited with an above-band laser, revealing the inhomogeneous broadening of quantum dots. (c) A similar measurement performed under p-shell excitation.

energy is called the *s-shell*, and if populated by an electron in the conduction band and a hole in the valence band, gives rise to a charge complex called the *neutral exciton*. The latter decays with a time constant called *lifetime*, typically $T_1 = 1$ ns for QDs in bulk, and emits a photon upon recombination of the electron and hole. To observe this effect, it is necessary to cool down the quantum dot platform to cryogenic temperatures, between 1.6-4 K, to ensure that the thermal energy is smaller than the confinement potential.

One way to create this exciton is to promote an electron of the valence band to the conduction band, creating a hole in the valence band, using a laser with higher energy than the GaAs bandgap, a technique called *above-band excitation*. Such a measurement is shown in Fig. 1.2(c) and reveals the spread in wavelength of the emitted photons, in the range of $915 - 945$ nm, all depending on the size of the quantum dot. This wavelength distribution is called *inhomogeneous broadening* and highlights the uniqueness of each quantum dot, originating from the randomness of the self-assembled growth. The two charges will diffuse to the s-shell by releasing energy to the environment and exciting phonon states. Alternatively, a laser can create charges on the p-shell, which then decay non-radiatively to the s-shell, creating the exciton complex. This off-resonant excitation method has been used extensively due to the possibility of filtering the laser frequency from the QD emission. This excitation scheme also enables to address single excitonic transitions, as shown in Fig. 1.2(d). The non-radiative decay through phonon processes happens over a picosecond time scale but is enough to diminish the coherence of the emission. Finally, fully resonant laser light can be directly absorbed to create the exciton. This is a *resonant* process, which does not require interaction with phonons. Recent optimization of the wafer growth included a thin AlAs layer (0.3 nm) before the growth of the capping GaAs layer, resulting in the removal of unwanted coupling to the wetting layer continuum states, to enhance the exciton optical performance (Löbl et al. 2019).

Regarding the band diagram of the charges involved in the exciton creation, the heavy hole and light hole band degeneracy is lifted due to the quantization along the growth direction (Lodahl et al. 2015). The exciton complex is constituted of an electron from the conduction band and a heavy hole from the valence band, with the atomic orbitals properties shown in Fig .1.1(c). The electron from the conduction band inherits the s-symmetry of the atomic orbitals and has total angular momentum $J = \frac{1}{2}$ and projections on the quantization axis $J_z = \pm\frac{1}{2}$. The heavy hole inherits the p-symmetry of the valence electrons of Ga and As $J = \frac{3}{2}$ and projections $J_z = \pm\frac{3}{2}$. We note the two electron states as spin-up $|\uparrow\rangle$ and $|\downarrow\rangle$ spin-down, and $|\Uparrow\rangle$ and $|\Downarrow\rangle$ for the heavy hole. They are four possible exciton states, with $J = 2$ and the four projections $J_z = \{-2, -1, 1, 2\}$. The two states with $J_z = \pm 1$ are called *bright excitons* as they can decay radiatively, and the two states with $J_z = \pm 2$ are dark states with forbidden radiative recombination. The bright and dark states are non-degenerate due to the Coulomb interaction, on the order of a few hundred μeV (Zieliǹski 2021).

1.2.2 Decay dynamics

In self-assembled quantum dots, the inherent strain in the growth leads to asymmetry along the crystallographic axis, which has the effect of creating a coherent superposition of the two bright states, leading to two optical dipoles with lifted degeneracy, as shown in Fig. 1.3(a). Each dipole presents a dark state, which decays non-radiatively at a rate $\gamma_{\mathrm{nrad,d}}$. The transition between bright and dark states is allowed by spin-flip at a rate γ_{sf}. Each dipole can decay to the ground state, with radiative decay rate γ_{rad}, emitting a photon with linear polarization and slightly detuned by Δ_{FSS} in energy, due to the fine structure splitting of around 10-100 μeV (Lodahl et al. 2015). The bright excitons can also decay non-radiatively with the decay rate $\gamma_{\mathrm{nrad,b}}$.

If only one of the bright exciton is excited, the coupling to the other is suppressed as this effect would require two spin flips, likely improbable. The dynamic of the population ρ_b of the bright exciton is then generic for both dipoles. Assuming an equal initial population of the dark and bright states, possible for non-resonant excitation of the quantum dot, the bright state population, described by a biexponential decay (Wang et al. 2011), reads

$$\rho_b(t) = A_f e^{-\gamma_f t} + A_s e^{-\gamma_s t}, \tag{1.1}$$

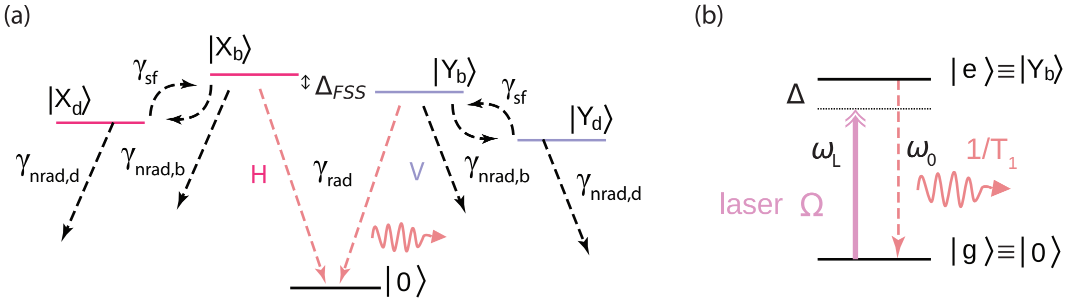

FIGURE 1.3: Neutral exciton in self-assembled quantum dots. (a) Schematic of the energy level of the neutral exciton with four dipoles. Two bright dipoles allow radiative recombination with decay rate γ_{rad} and are non-degenerated by Δ_{FSS}. Each bright dipole can couple to its related dark state through a spin-flip process. The dark excitons decay non-radiatively, leaving the quantum dot in its ground state, and a similar process is possible for the bright excitons. (b) If one bright dipole is isolated, for example, $|Y_b\rangle$, we may treat the system bright exciton-empty quantum dot as a two-level system between ground and excited state with energy ω_0. A laser of frequency ω_L may drive the transition with a Rabi frequency Ω, and the excited state decays radiatively at a rate $\gamma = 1/T_1$.

with the fast and slow decay rates given by $\gamma_{f/s} = \gamma_{\text{rad}}/2 + \gamma_{\text{nrad,b}} + \gamma_{\text{sf}} \pm \sqrt{\gamma_{\text{rad}}^2/4 + \gamma_{\text{sf}}^2}$. If the spin-flip rate is slower than the radiative decay, the fast decay will be $\gamma_f = \gamma_{\text{rad}} + \gamma_{\text{nrad,b}}$ (Johansen et al. 2010). The advantage of quantum dots as quantum emitters is that they are characterized by a large quantum efficiency, defined as $\eta = \gamma_{\text{rad}}/(\gamma_{\text{rad}} + \gamma_{\text{nrad,b}})$. Moreover, as we shall introduce in Chapter 2, the radiative decay rate can be enhanced by the environment of the quantum dot, which inhibits the effect of non-radiative decay. The latter may also be strongly suppressed by high-quality material limiting the non-radiative decay channels, which ensures close to unity quantum efficiency (Lodahl et al. 2015). As a final consideration, if both bright excitons are excited, for example, with a laser pulse of bandwidth larger than Δ_{FSS}, the time-resolved measurement of the population may exhibit a non-trivial decay, with contributions from both radiative decay channels. Oscillations may be observed on a timescale given by Δ_{FSS}^{-1} (Schwartz et al. 2016).

A quantum dot can host more charge states than the neutral exciton. Indeed, the quantum dot may trap an extra electron or an additional hole, leading to a negatively or positively charged exciton, respectively. These states present a spin that can be coherently controlled (Warburton 2013) and entangled with photons (Appel et al. 2022). Additionally, two excitons may be trapped in the quantum dot, a biexciton state. Due to their cascaded emission, these states are particularly interesting for deterministically generating entangled states (Østfeldt et al. 2022). The charged exciton and biexciton present different decay dynamics than the neutral exciton (Lodahl et al. 2015) but are not covered here.

Although the neutral exciton presents two dipoles, it is possible to address a single one with a narrow band laser, and in this sense, we consider the exciton as a two-level system, as pictured in Fig. 1.3(b). In this picture, the ground state corresponds to an empty quantum dot, and the excited state corresponds to one exciton. A laser with frequency ω_L can be detuned by $\Delta = \omega_L - \omega_0$ to the excited state energy ω_0 and drive the two-level system at a Rabi frequency Ω. A photon is emitted with frequency ω_0 after spontaneous emission of the populated excited state with a decay rate $\gamma = 1/T_1$.

1.3 Resonance fluorescence of quantum dots

In the picture of a two-level system, all the results from well-studied resonance fluorescence under excitation with a continuous-wave (cw) laser (Scully et al. 1997) hold. In this section, we will highlight the key properties of resonance fluorescence of a two-level system in terms of excited state population and coherence of the emission. For this, we closely follow the derivation given in (Muller 2007).

1.3.1 Master equation and population of the excited state

A two-level system is characterized by a ground state $|g\rangle$ and an excited state $|e\rangle$ and the operators $\hat{\sigma}_- = |g\rangle \langle e|$ and $\hat{\sigma}_+ = |e\rangle \langle g|$ describe the transitions between the two states, with energy difference ω_0. We now consider a monochromatic laser field described as $\mathcal{E} = \mathcal{E}_0(e^{-i\omega_L t} + e^{i\omega_L t})/2$, where $\mathcal{E}_0^2$ is proportional to the intensity of the field. Light-matter interaction can be described by $H_{\text{int}} = -\vec{d} \cdot \vec{\mathcal{E}}$, valid in the dipole approximation, where $\vec{d}$ is the dipole moment operator expressed as $\vec{d} = \vec{d}_{eg}(\hat{\sigma}_+ + \hat{\sigma}_-)$, $\vec{d}_{eg}$ being the transition dipole moment aligned on the dipole orientation. The strength of the interaction can be written in terms of the Rabi frequency Ω defined as $\Omega = (\vec{d}_{eg} \cdot \vec{\mathcal{E}})/\hbar$, which denotes that only components of the electric field aligned with the dipole transition will contribute to the interaction. Finally, the full-time-independent Hamiltonian describing the non-interacting part and the interaction with the laser in the rotating-wave approximation and in a frame rotating at the laser frequency reads

$$\hat{H} = \hbar\Delta\omega\hat{\sigma}_+\hat{\sigma}_- - \frac{\hbar\Omega}{2}(\hat{\sigma}_+ + \hat{\sigma}_-). \tag{1.2}$$

In a closed system, i.e. not interacting with a reservoir, the time evolution of an arbitrary state of the system $|\Psi\rangle = c_e(t)\,|e\rangle + c_g(t)\,|g\rangle$ will be given by the Schrödinger equation $i\hbar\frac{\partial|\Psi\rangle}{\partial t} = \hat{H}\,|\Psi\rangle$. After solving the equation of motion, the coefficient describing the population amplitude in each state will oscillate as a function of the Rabi frequency and detuning without any damping. Another way to describe the system is through the density matrix $\hat{\rho}(t) = \rho_{ee}(t)\hat{\sigma}_+\hat{\sigma}_- + \rho_{eg}(t)\hat{\sigma}_- + \rho_{ge}(t)\hat{\sigma}_+ + \rho_{gg}(t)\hat{\sigma}_-\hat{\sigma}_+$ which obeys the equation of motion $\frac{d}{dt}\hat{\rho}(t) = \frac{-i}{\hbar}[\hat{H}, \hat{\rho}(t)]$, where the off-diagonal terms describe the coherence of the system.

Real systems interact with a reservoir, leading to spontaneous emission from the excited state to the ground state at a rate γ, which provokes a population decay. Interaction with a reservoir contributes to the loss of coherence due to pure dephasing characterized by a rate γ_d, which does not affect the population. These effects can be added phenomenologically to the equation of motion through the Liouvillian operators (Meystre et al. 2007), giving

$$\frac{d}{dt}\hat{\rho}(t) = -\frac{i}{\hbar}[\hat{H}, \hat{\rho}(t)] + \mathcal{L}[\gamma, \hat{\sigma}_-] + \mathcal{L}[\frac{1}{2}\gamma_d, \hat{\sigma}_z], \tag{1.3}$$

where $\hat{\sigma}_z = [\hat{\sigma}_+, \hat{\sigma}_-]$ and the operators have the Lindblad form $\mathcal{L}[\alpha, \hat{O}] \equiv \alpha(\hat{O}\hat{\rho}\hat{O}^\dagger - \frac{1}{2}\hat{O}^\dagger\hat{O}\hat{\rho} - \frac{1}{2}\hat{\rho}\hat{O}^\dagger\hat{O})$. We can develop Eq. 1.3 and write the equations of motion of each element of the density matrix $\hat{\rho}(t)$

$$\frac{d}{dt}\begin{pmatrix} \rho_{gg} \\ \rho_{ge} \\ \rho_{eg} \\ \rho_{ee} \end{pmatrix} = \begin{pmatrix} 0 & i\Omega/2 & -i\Omega/2 & \gamma \\ i\Omega/2 & -\gamma/2 - \gamma_d + i\Delta & 0 & -i\Omega/2 \\ -i\Omega/2 & 0 & -\gamma/2 - \gamma_d - i\Delta & i\Omega/2 \\ 0 & -i\Omega/2 & i\Omega/2 & -\gamma \end{pmatrix} \begin{pmatrix} \rho_{gg} \\ \rho_{ge} \\ \rho_{eg} \\ \rho_{ee} \end{pmatrix}, \tag{1.4}$$

where we dropped the explicit time dependence. From the equations of motion, we see that the change of population of the excited state is governed by the spontaneous emission through the decay rate γ, while the loss of coherence happens at a total rate $\gamma_2 = \gamma/2 + \gamma_d$.

If the two-level system is driven continuously, we can look at the equations of motion in the steady state regime ($t \to \infty$), for which $\frac{d}{dt}\hat{\rho}(t) = 0$ and more particularly the population of the excited state reads

$$\rho_{ee}(t \to \infty) = \frac{\Omega^2}{4\gamma}\frac{2\gamma_2}{\Delta^2 + \gamma_2^2 + \Omega^2\gamma_2/\gamma}. \tag{1.5}$$

One can probe the population of the excited state by tuning the frequency of a narrow-band laser across the transition and recording the scattered intensity. Such a measurement reveals a Lorentzian absorption spectrum as a function of detuning Δ as shown in Fig. 1.4(a), at a Rabi frequency of $\Omega = 0.2\gamma$. The maximum absorption is achieved for $\Delta = 0$ and $\gamma_d = 0$, and increasing γ_d enlarges the linewidth of the spectrum. In the low-power regime, the full-width half-maximum (FWHM) of the Lorentzian spectrum is given by $\Delta_{\mathrm{FWHM}} = 2\gamma_2$, which is called the transform-limited value. In the absence of dephasing, the FWHM is simply $\Delta_{\mathrm{FWHM}}(\gamma_d = 0) = \gamma$, as shown in Fig. 1.4(b), called the lifetime-limit, reaching the time-energy uncertainty. The power through the Rabi frequency also influences the FWHM through $\Delta_{\mathrm{FWHM}} = 2\sqrt{\gamma_2^2 + \Omega^2\gamma_2/\gamma}$, an effect called *power broadening*. Increasing the Rabi frequency also increases the maximum population of the excited state, as shown in Fig. 1.4(c), until it saturates at the value of 0.5. This result also holds for increasing dephasing, but more power will be necessary to reach saturation.

These key results of resonance fluorescence will be helpful throughout the thesis to understand the optical properties of the quantum dot transitions investigated in Chapter 4. One step further into the analysis is to

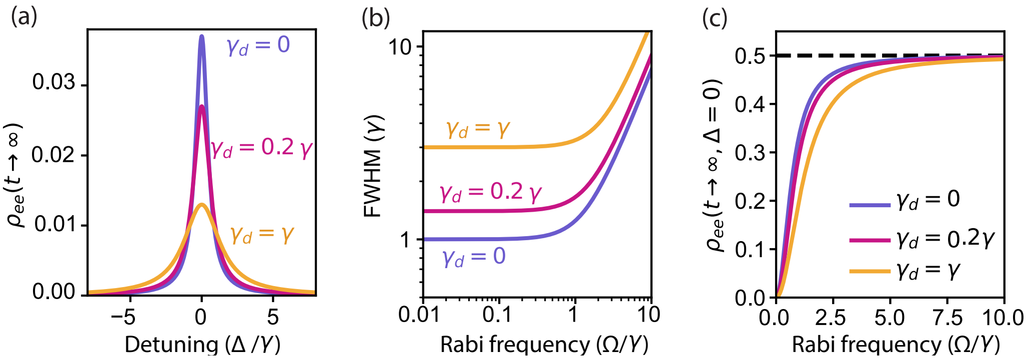

FIGURE 1.4: Resonance fluorescence of a two-level system. (a) The absorption spectrum of a two-level system driven at a Rabi frequency $\Omega = 0.2\gamma$, subjected to different pure dephasing rates γ_d. (b) Full-width half-maximum (FWHM) of the Lorentzian of the absorption spectrum as the Rabi frequency is increased. In the low power limit, with no dephasing, the linewidth is limited by the decay rate γ. With the pure dephasing, the FWHM goes as $\gamma + 2\gamma_d$. Power broadening is seen as the increase in linewidth with the Rabi frequency. (c) The maximum population in the excited state at the steady-state, for no detuning of the laser, shows a saturation behavior as the Rabi frequency increases. In the presence of pure dephasing, saturation appears for higher Rabi frequencies, proportional to the optical power.

probe the first-order and second-order coherence of the light scattered by a two-level system.

1.3.2 Coherence functions

The first-order coherence function describes the ability of the field to interfere with itself, regarded as the correlation of the field amplitude, and the two-times functions reads

$$G^{(1)}(t,\tau) = \left\langle E^{(-)}(t)E^{(+)}(t+\tau)\right\rangle , \tag{1.6}$$

where $E^{(-)}(t)$ and $E^{(+)}(t)$ are the negative and positive frequency components of the radiated electric field, respectively (Meystre et al. 2007). Since the electric field of an oscillating dipole is proportional to the dipole moment itself in the far field limit, we may use $E^{(+)}(t) \propto \hat{\sigma}_-(t)$. Consequently, the coherence functions can be written in terms of the atomic operators, such that the dynamic of the emitter will predict the coherence of the scattered photons. In the stationary limit, the two-time variables can be changed into single-time such that

$$G^{(1)}(\tau) = \langle \sigma_+(0)\sigma_-(\tau)\rangle , \tag{1.7}$$

where we need to calculate the two-times correlation of system operators. The quantum regression theorem comes in handy to perform this task since it states that the two-times correlation of system operators follows the same time evolution as one-time average (Steck 2007), meaning that correlations can be found through solutions of the master equation. More precisely, if the one-time average of a system operator B can be written as

$$\langle B(t)\rangle = \sum_j g_j(t)\,\langle B_j(0)\rangle \tag{1.8}$$

where the coefficients $g_j(t)$ are found by solving the full dynamics of the master equations given some initial conditions, then the two-time correlation between two operators reads

$$\langle A(t)B(0)\rangle = \sum_j g_j(t)\,\langle AB_j\rangle\,. \tag{1.9}$$

The equations of motion of the density matrix, which can be written as $\frac{d}{dt}\rho(t) = \mathbf{M}\rho(t)$, have solutions in the form $\rho(t+\tau) = \mathbf{U}(\tau)\rho(t)$, where $\mathbf{U}(\tau) = e^{\mathbf{M}\tau}$. The matrix elements $\mathbf{U}_{m,n}$ can be extracted by calculating the power series. Now, the two-time average boils down to calculating the one-time average given the solutions to the master equation such that

$$\begin{aligned} G^{(1)}(\tau) &= \langle\sigma_+(0)\sigma_-(\tau)\rangle \\ &= \mathbf{U}_{21}(\tau)\,\langle\sigma_+\sigma_-\sigma_+\rangle + \mathbf{U}_{22}(\tau)\,\langle\sigma_+\sigma_-\rangle + \mathbf{U}_{23}(\tau)\,\langle\sigma_+\sigma_+\rangle + \mathbf{U}_{24}(\tau)\,\langle\sigma_+\sigma_+\sigma_-\rangle \\ &= \mathbf{U}_{21}(\tau)\rho_{ge} + \mathbf{U}_{22}(\tau)\rho_{ee}, \end{aligned} \tag{1.10}$$

and in the steady state limit, the first-order coherence reads and in the absence of detuning ($\Delta = 0$) (Muller 2007)

$$\begin{aligned} G^{(1)}(\tau) = \frac{\Omega^2}{2\Omega^2+\gamma^2+2\gamma\gamma_d}\Bigg[&\frac{\gamma^2}{2\Omega^2+\gamma^2+2\gamma\gamma_d} + \frac{1}{2}e^{-\left(\frac{\gamma}{2}+\gamma_d\right)\tau} \\ &+ e^{-\left(\frac{3\gamma}{4}+\frac{\gamma_d}{2}\right)\tau}\big(A\cos(\mu\tau) - B\sin(\mu\tau)\big)\Bigg] \end{aligned} \tag{1.11}$$

where

$$\begin{aligned} \mu &= \sqrt{\Omega^2-(\gamma/4-\gamma_d/2)^2}, \\ A &= \frac{1}{2}\frac{2\Omega^2-\gamma^2+2\gamma\gamma_d}{2\Omega^2+\gamma^2+2\gamma\gamma_d}, \\ B &= \frac{1}{4\mu}\frac{\Omega^2(2\gamma_d-5\gamma)+\gamma^3/2+2\gamma_d\gamma-2\gamma_d\gamma^2}{2\Omega^2+\gamma^2+2\gamma_d\gamma}. \end{aligned} \tag{1.12}$$

The normalized expression is obtained by $g^{(1)}(t,\tau) = \frac{G^{(1)}(t,\tau)}{\sqrt{\langle\sigma_+(t)\sigma_-(t)\rangle\langle\sigma_+(t+\tau)\sigma_-(t+\tau)\rangle}}$ and the denominator in the steady-state is the maximum population $\rho_{ee}(t\to\infty)$. The normalized first-order coherence is shown in Fig. 1.5(a) in the case of no dephasing but increasing Rabi frequency. We note that in the low-power regime, the coherence is close to the one of a coherent state, which highlights the coherent part of the QD emission, or more precisely, coherent scattering in the Rayleigh regime. As the Rabi frequency is increased, the coherence decays and starts oscillating for large driving. This is linked to the probability of populating the excited state increasing and leading to a higher contribution of photons spontaneously emitted, which is an incoherent process. Loss of coherence also arises from the presence of dephasing in the system, as seen in Fig. 1.5(b), even at low power driving ($\Omega = 0.1\gamma$), where most of the scattered field originates from a coherent process. This shows that dephasing processes in QD are the limiting factor of coherence.

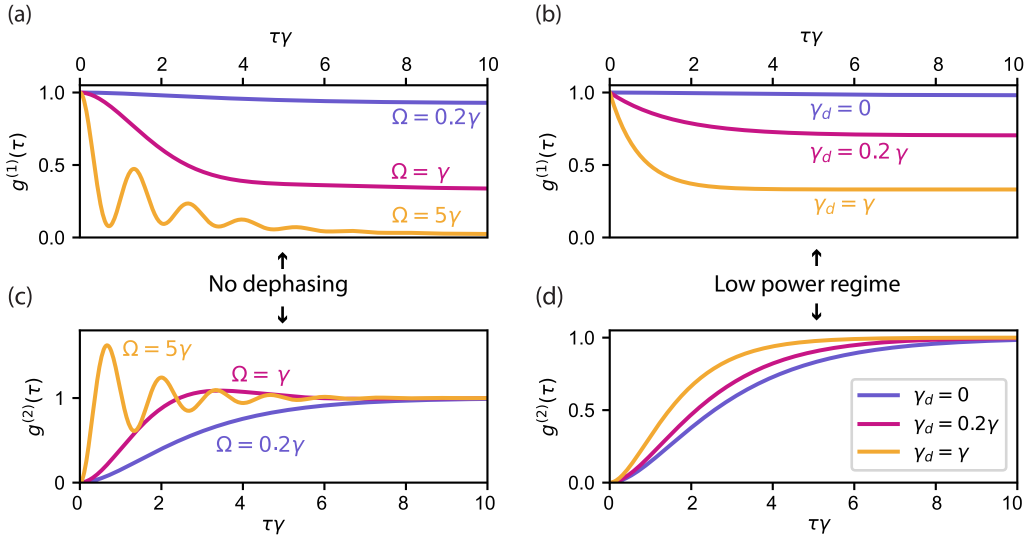

FIGURE 1.5: Coherence functions of a two-level system. The first-order coherence function is shown (a) in the absence of dephasing at increasing Rabi frequency and (b) at $\Omega = 0.2\gamma$ and increasing dephasing rate. The second-order coherence function is shown (c) in the absence of dephasing and increasing Rabi frequency and (d) at a fixed Rabi frequency $\Omega = 0.2\gamma$ and increasing dephasing rate. The antibunching at zero time delay is insensitive to Rabi frequency or dephasing, only the width of the dip narrows. Rabi oscillations are seen as the Rabi frequency increases.

The spectrum of the emission can be calculated by calculating the Fourier transform of the first-order coherence. The low power regime shows a narrow line centered at the laser frequency, with the width given by the laser bandwidth. In the high power regime, the interaction with the driving laser gives rise to sidebands in the shape of the Mollow triplet. In the intermediate power regime, the spectrum comports a single peak of width given by the total coherence of the system, corresponding to the radiative limit $2\gamma_2$ (Michler 2017). The spectrum can be directly measured with a Fabry-Perot interferometer (Matthiesen et al. 2012) and the first-order coherence function can be extracted from a Michelson interferometer (Makhonin et al. 2014).

Another interesting coherence function is the one measuring the degree of correlation in the intensity of the scattered field or, in other words, the probability of detecting a second photon at time $t + \tau$ given that a first one was detected at time t. The second-order correlation function is expressed as

$$G^{(2)}(t, \tau) = \langle \hat{\sigma}_+(t)\hat{\sigma}_+(t+\tau)\hat{\sigma}_-(t+\tau)\hat{\sigma}_-(t) \rangle \tag{1.13}$$

Similarly, this two-time average can be conveniently reduced to one-time averages by applying the quantum regression theorem $\langle A(t+\tau)B(\tau)C(t+\tau)\rangle = \sum_j g_j(\tau)\,\langle A(t)B_j(t)C(t)\rangle$. We can then compute the second-order correlation function as

$$\begin{aligned} G^{(2)}(\tau) &= \mathbf{U}_{41}(\tau)\,\langle\hat{\sigma}_+\hat{\sigma}_-\hat{\sigma}_+\hat{\sigma}_-\rangle + \mathbf{U}_{42}(\tau)\,\langle\hat{\sigma}_+\hat{\sigma}_-\hat{\sigma}_-\rangle \\ &+ \mathbf{U}_{43}(\tau)\,\langle\hat{\sigma}_+\hat{\sigma}_+\hat{\sigma}_-\rangle + \mathbf{U}_{44}(\tau)\,\langle\hat{\sigma}_+\hat{\sigma}_+\hat{\sigma}_-\hat{\sigma}_-\rangle \\ &= \mathbf{U}_{41}(\tau)\rho_{ee}, \end{aligned} \tag{1.14}$$

such that in the steady-state and in the absence of detuning ($\Delta = 0$), after normalization by $\rho_{ee}^2(t \to \infty)$, we get (Muller 2007)

$$g^{(2)}(\tau) = 1 - e^{-\left(\frac{3\gamma}{4}+\frac{\gamma_d}{2}\right)\tau}\left(\cos(\mu\tau) + \frac{3\gamma + 2\gamma_d}{4\mu}\sin(\mu\tau)\right). \tag{1.15}$$

We show the second-order correlation in Fig. 1.5(c) in the absence of dephasing and increasing Rabi frequency and notice $g^{(2)}(0) = 0$ in all cases. This stems from the photon *antibunching* and is a purely non-classical effect which proves that the emission source is a single quantum emitter. Once a photon is emitted and detected, the two-level system is brought to its ground state, and it takes some time, given by μ^{-1} before the two-level system can be excited again and emit a second photon. A pronounced bunching is seen at a short time delay and with amplitude and frequency increasing with the Rabi frequency due to Rabi oscillations. This is a sign of coherent interaction between the two-level system and the driving field. The dephasing will also impact the second-order correlation function by narrowing the antibunching time window, as shown in Fig. 1.5(d). This effect can be understood by considering the dip in the second-order correlation function as the result of the interference between the coherent and incoherent parts of the field (Hanschke et al. 2020). Dephasing modifies the contribution of coherent scattering to the field and inherently changes the interference setting. The second-order correlation function is measured with a Hanbury Brown and Twiss experiment (Brown et al. 1956), where the photons impinge one input of a balanced beamsplitter, and the detection events at the outputs are time-correlated. Implications of the $g^{(2)}(\tau = 0)$ value will be discussed in Chapter 2.

The presented results of resonance fluorescence hold for continuous-wave excitation in the steady-state limit, which is a probabilistic excitation method and gives an averaged picture of the quantum dot dynamics. In turn, the two-level transition can be excited with a pulsed laser following a Gaussian distribution in time, which allows triggering the emission of photons. The Rabi frequency is then also time-dependent and allows to coherently control the two-level system. For example, population inversion can be achieved with a π-pulse, leading to the deterministic generation of single-photon states. In general, coherent driving of the two-level system is realized with resonant pulsed excitation through Rabi oscillations. An experimental demonstration will be shown in Chapter 5, while theoretical results of resonance fluorescence with pulsed excitation need to be evaluated numerically.

1.4 Two-photon quantum interference

When two indistinguishable single photons emitted by two identical quantum emitters or originating from a single emitter, meet at the inputs of a $50:50$ beamsplitter, they will always coalesce in one or the other output and never be registered as going out both ways. This effect is known as the two-photon quantum interference Hong-Ou-Mandel (HOM) effect and is a salient feature of non-classical systems, measured for the first time in (Hong et al. 1987). This destructive interference only occurs if the photons are indistinguishable in all degrees of freedom and is, therefore, a measure of the identity of single-photon sources. Photon interference is also a fundamental effect enabling photons to be a resource for quantum computation.

An intuitive picture is given in the Fock state basis, where the input fields at ports 1 and 2 of a perfect $50:50$ beamsplitter, indicated in Fig. 1.6(a), are considered pure single-photon states. In this case, the initial state is described as $|1_1 1_2\rangle = \hat{a}_1^\dagger \hat{a}_2^\dagger |0\rangle$, where $\hat{a}_j^\dagger$ is the creation operator acting on mode j (Legero et al. 2003). The beamsplitter performs the following unitary transformation

$$\begin{pmatrix} \hat{a}_3^\dagger \\ \hat{a}_4^\dagger \end{pmatrix} = \frac{1}{\sqrt{2}} \begin{bmatrix} 1 & i \\ i & 1 \end{bmatrix} \begin{pmatrix} \hat{a}_1^\dagger \\ \hat{a}_2^\dagger \end{pmatrix}, \tag{1.16}$$

from which the input field operators can be expressed in terms of the output field creation operators $\hat{a}_3^\dagger$ and $\hat{a}_4^\dagger$. From this transformation follows $\hat{a}_1^\dagger \hat{a}_2^\dagger |0\rangle = \frac{1}{2}(\hat{a}_3^\dagger - i\hat{a}_4^\dagger)(-i\hat{a}_3^\dagger + \hat{a}_4^\dagger)|0\rangle = \frac{-i}{2}([\hat{a}_3^\dagger]^2 + [\hat{a}_4^\dagger]^2)|0\rangle = \frac{-i}{\sqrt{2}}(|2_3 0_4\rangle + |0_3 2_4\rangle)$, where we use $\hat{a}^\dagger |n\rangle = \sqrt{n+1}\,|n+1\rangle$. Due to destructive interference between the cross-output-ports probability amplitudes, the simultaneous detection of two photons at the output ports vanishes. Two pure indistinguishable single photons always coalesce at the same output port, with equal 50% probability.

To extract a more functional description of the two-photon interference, it is interesting to describe the intensity correlation of the two fields at the output of the beamsplitter by calculating the second-order correlation function as

$$G_{ab}^{(2)}(t,\tau) = \left\langle \hat{E}_b^{(-)}(t)\hat{E}_a^{(-)}(t+\tau)\hat{E}_a^{(+)}(t+\tau)\hat{E}_b^{(+)}(t) \right\rangle. \tag{1.17}$$

The second-order correlation function is expressed in terms of the field operators of the output modes $\hat{a}$ and $\hat{b}$ radiated by a two-level system A, with frequency $\omega_0 + \Delta\omega/2$ and a two-level system B, with frequency $\omega_0 - \Delta\omega/2$, respectively. Each two-level system is driven by a cw-laser resonant at ω_0 and $\Delta\omega$ accounts for a small static frequency detuning of the optical transition from the central frequency (Woolley et al. 2013). For compactness, we replace the field operators by $\hat{E}_j^{(+)}(t) \equiv \hat{j}(t)$ and $\hat{E}_j^{(-)}(t) \equiv \hat{j}^\dagger(t)$, with $j \in \{a, b, a', b'\}$. We perform a modified beamsplitter operation than shown

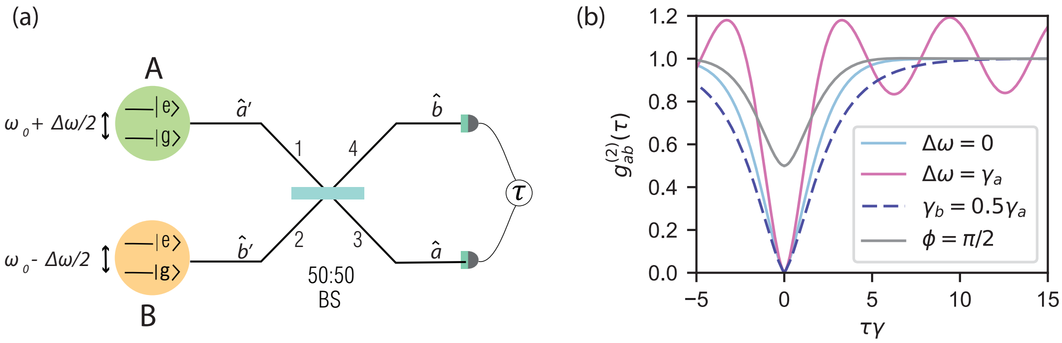

FIGURE 1.6: Two-photon quantum interference between two remote quantum emitters. (a) The fields emitted by two quantum emitters A and B are sent to one input of a $50:50$ beamsplitter (BS) each. Two detectors at the outputs of the BS record coincidence counts as a function of time delay τ. (b) Calculated second-order correlation function between mode a and b. The result is shown for different mutual detuning $\Delta\omega$ and radiative decay γ. For each measurement, the Rabi frequency is $\Omega_j = \gamma_j$, where $j \in \{a, b\}$. The curve with $\phi = \pi/2$ accounts for the configuration where the outputs are cross-polarized.

in Eq. 1.16, reading $\hat{a} = (\hat{a}'(t) - \hat{b}'(t))$ and $\hat{b} = (\hat{a}'(t) + \hat{b}'(t))$, to avoid an additional global phase. Without loss of generality, the second-order correlation function in terms of the input field operator reads

$$
\begin{aligned}
G^{(2)}_{ab}(t,\tau) = \frac{1}{4} \sum_{(\hat{c},\hat{d})\in\Pi\left(\hat{a}',\hat{b}'\right)} \Bigg[& \underbrace{\left\langle \hat{c}^\dagger(t)\hat{c}^\dagger(t+\tau)\hat{c}(t+\tau)\hat{c}(t)\right\rangle}_{1} + \underbrace{\left\langle \hat{c}^\dagger(t)\hat{c}(t)\right\rangle \left\langle \hat{d}^\dagger(t+\tau)\hat{d}(t+\tau)\right\rangle}_{2} \\
& - \underbrace{\left\langle \hat{c}^\dagger(t+\tau)\hat{c}(t)\right\rangle \left\langle \hat{d}^\dagger(t)\hat{d}(t+\tau)\right\rangle}_{3} - \underbrace{\left\langle \hat{c}^\dagger(t+\tau)\hat{c}^\dagger(t)\right\rangle \left\langle \hat{d}(t+\tau)\hat{d}(t)\right\rangle}_{4} \\
& + \underbrace{\left\langle \hat{d}(t)\right\rangle \left\langle \hat{c}^\dagger(t)\hat{c}^\dagger(t+\tau)\hat{c}(t+\tau)\right\rangle}_{5} + \underbrace{\left\langle \hat{d}^\dagger(t)\right\rangle \left\langle \hat{c}^\dagger(t+\tau)\hat{c}(t+\tau)\hat{c}(t)\right\rangle}_{6} \\
& - \underbrace{\left\langle \hat{d}(t+\tau)\right\rangle \left\langle \hat{c}^\dagger(t+\tau)\hat{c}^\dagger(t)\hat{c}(t)\right\rangle}_{7} - \underbrace{\left\langle \hat{d}^\dagger(t+\tau)\right\rangle \left\langle \hat{c}^\dagger(t)\hat{c}(t+\tau)\hat{c}(t)\right\rangle}_{8} \Bigg] .
\end{aligned}
\tag{1.18}
$$

The correlations are performed for each system separately, for example, $\left\langle \hat{c}^\dagger(t+\tau)\hat{c}(t)\hat{d}^\dagger(t)\hat{d}(t+\tau)\right\rangle = \left\langle \hat{c}^\dagger(t+\tau)\hat{c}(t)\right\rangle \left\langle \hat{d}^\dagger(t)\hat{d}(t+\tau)\right\rangle$, since the two systems are independent.

The field operators can be described as a slowly varying envelope with an oscillating term at the emitter frequency. Moreover, there can be a phase offset θ between the fields $\hat{a}'$ and $\hat{b}'$, such that $\hat{c}(t) = \bar{c}(t)e^{i(\omega_0+\Delta\omega/2)t+i\theta}$ and $\hat{d}(t) = \bar{d}(t)e^{i(\omega_0-\Delta\omega/2)t}$. These phase-dependent terms enter in the cross-correlation function $G^{(2)}_{ab}(t,\tau)$ through correlation terms 4 to 8, for example, correlation 5 reads $\langle\hat{d}(t)\rangle\left\langle\hat{c}^{\dagger}(t)\hat{c}^{\dagger}(t+\tau)\hat{c}(t+\tau)\right\rangle=\langle\bar{d}(t)\rangle\left\langle\bar{c}^{\dagger}(t)\bar{c}^{\dagger}(t+\tau)\bar{c}(t+\tau)\right\rangle e^{-i\Delta\omega t-i\theta}$. However, repeating the correlation measurement with a varying phase and further averaging over the several runs eliminate the phase-dependent correlations terms 4 to 8. In practice, in the absence of active phase stabilization of the two optical paths, even if exciting with a single coherent laser, the phase information is certainly randomized, and correlation terms 4 to 8 vanish.

Since the radiated field is proportional to the lowering operator, we may replace the slowly varying field $\bar{c}(t)\propto\sigma_-^c(t)$. The correlation between the output fields after the beamsplitter simplifies to

$$\begin{aligned}G_{ab}^{(2)}(t,\tau)\propto\frac{1}{4}\Big[&\left\langle\sigma_+^{a'}(t)\sigma_+^{a'}(t+\tau)\sigma_-^{a'}(t+\tau)\sigma_-^{a'}(t)\right\rangle+\left\langle\sigma_+^{b'}(t)\sigma_+^{b'}(t+\tau)\sigma_-^{b'}(t+\tau)\sigma_-^{b'}(t)\right\rangle\\&+\left\langle\sigma_+^{a'}(t)\sigma_-^{a'}(t)\right\rangle\left\langle\sigma_+^{b'}(t+\tau)\sigma_-^{b'}(t+\tau)\right\rangle+\left\langle\sigma_+^{b'}(t)\sigma_-^{b'}(t)\right\rangle\left\langle\sigma_+^{a'}(t+\tau)\sigma_-^{a'}(t+\tau)\right\rangle\\&-\mathrm{e}^{i\tau\Delta\omega}\left\langle\sigma_+^{b'}(t+\tau)\sigma_-^{b'}(t)\right\rangle\left\langle\sigma_+^{a'}(t)\sigma_-^{a'}(t+\tau)\right\rangle\\&-\mathrm{e}^{-i\tau\Delta\omega}\left\langle\sigma_+^{a'}(t+\tau)\sigma_-^{a'}(t)\right\rangle\left\langle\sigma_+^{b'}(t)\sigma_-^{b'}(t+\tau)\right\rangle\Big].\end{aligned}\tag{1.19}$$

Taking the steady-state limit, we recognize the first- and second-order correlation functions that were introduced in Eqs. 1.11 and 1.15, respectively, which are used to express the cross-correlation function as

$$\begin{aligned}G_{ab}^{(2)}(\tau)\propto\frac{1}{4}\Big\{&G_{a'}^{(2)}(\tau)+G_{b'}^{(2)}(\tau)+2G_{a'}^{(1)}(0)G_{b'}^{(1)}(0)\\&-\mathrm{e}^{\mathrm{i}\tau\Delta\omega}G_{a'}^{(1)}(\tau)\left[G_{b'}^{(1)}(\tau)\right]^*-\mathrm{e}^{-\mathrm{i}\tau\Delta\omega}\left[G_{a'}^{(1)}(\tau)\right]^*G_{b'}^{(1)}(\tau)\Big\}\end{aligned}\tag{1.20}$$

From Eq. 1.20, we conclude that the vanishing probability of detecting coincidences, $G_{ab}^{(2)}(0)=0$, is a combined effect of the single-photon statistics of each source, with $G^{(2)}(0)=0$, and of photon interference by the cancellation of the second term with the third and fourth terms through the first-order coherence. The distinguishability in frequency can be added with $\Delta\omega\neq 0$, which leads to oscillations known as quantum beats. However, the vanishing detection probability at $\tau=0$ is not impacted.

This expression can be further approximated if assuming that the sources show approximately the same first-order coherence

$$G_{ab}^{(2)}(\tau)\propto\frac{1}{4}\Big[G_a^{(2)}(\tau)+G_b^{(2)}(\tau)+2G_a^{(1)}(0)G_b^{(1)}(0)-2\cos(\Delta\omega\tau)|G_a^{(1)}(\tau)||G_b^{(1)}(\tau)|\Big].\tag{1.21}$$

The result of Eq. 1.21 is shown in Fig. 1.6(b) for two identical sources defined by a decay rate $\gamma_a=\gamma_b$, which are perfectly resonant with $\Delta\omega=0$, and driven at $\Omega=0.5\gamma$ (solid blue curve). The second-order correlation function is normalized by a value at a long time delay. Adding a detuning $\Delta\omega=\gamma_a$ leads to oscillations in the second-order correlation (pink curve). This frequency detuning will be used in Chapter 4 to describe the effect of random detuning on two-photon quantum interference. We show the impact of different emitter properties by letting $\gamma_b=0.5\gamma_a$, which leads to a broadening of the HOM dip due to the slower radiative decay (dashed blue curve). For all calculations, the dephasing rate is set to $\gamma_d = 0.1\gamma_a$. The HOM dip at $\tau = 0$ is robust to emitter properties disparities. By adding a polarization-dependent factor, $\propto \cos^2(\phi)$, in front of the last term of Eq. 1.21, the fields are configured to be fully distinguishable in polarization by setting $\phi = \pi/2$. In this case, the probability of coincident detection at $\tau = 0$ reaches the classical value of 0.5 (gray curve). The second-order correlation for cross-polarized fields is used experimentally to normalize the second-order correlation function for co-polarized fields and extract the visibility of the HOM interference.

1.5 Source of decoherence

As introduced in the previous section, the ability of two photons to interfere is intimately linked to their degree of coherence, which must be maximized. It is, therefore, necessary to understand the origin of decoherence effects. By performing purely resonant excitation, the pump induced decoherence is suppressed since the direct interaction with the two-level system allows the exciton population without interaction with phonons. The quasi-resonant excitation method also causes a time jitter in the excitation and therefore reduces coherence.

Other decoherence mechanisms come into play and directly impact the quantum emitter's dynamics. Through previous sections, we introduced the main results of resonance fluorescence of a two-level system, for example, the neutral exciton of the quantum dot, and showed the influence of pure dephasing on the absorption linewidth and on the coherence functions. The interaction with phonon states is the primary origin of pure dephasing and is eventually the ultimate limit to photon indistinguishability. Other stochastic noise, such as spin and charge noise, can also impair the emission properties, an effect known as spectral diffusion, and we will illustrate its impact.

1.5.1 Pure dephasing

After removing the pump-induced decoherence, the main source of pure dephasing for self-assembled quantum dots originates from elastic phonon scattering. This noise is inherent to the solid-state platform, as residual lattice vibrations are unavoidable. The two-level system can then interact with a manifold of phononic states. The linear electron-photon coupling results in the photon emission into the *zero phonon line* (ZPL), a process occurring without emission of phonons, and a weaker emission into a broad red-detuned *phonon sideband* (PSB). The latter process involves the emission of a phonon, described by a density of state leading to the broad Gaussian sideband (Santori et al. 2010). In the quantum dot platform, the emission into the PSB is strongly suppressed, unlike in other solid-state emitters such as color centers in diamond, leading to $> 95\%$ of photons emitted in the ZPL (Uppu et al. 2020b). The presence of PSB may be used advantageously by performing phonon-assisted excitation (Thomas et al. 2021). In this case, a laser is tuned to the absorption sideband and excites the ZPL by emission of a longitudinal-acoustic phonon.

The electron-phonon interaction is also subjected to linear and quadratic coupling that leaves the energy of the emission unchanged, ensuring that photons are emitted in the ZPL but broaden the emission spectrum. This effect is known as pure phonon dephasing and depends on the temperature and dimensionality of the quantum dots host material (Tighineanu et al. 2018). While the emission in the PSB may be filtered and therefore not alter the wavepacket of the emission, pure dephasing sets the limitation on indistinguishability with $V = \gamma/(\gamma + 2\gamma_d)$ (González-Ruiz et al. 2022), as it limits the coherence of the emitted photons. Moreover, the interaction with acoustic phonon deteriorates the coherent driving of the two-level system highlighted by the damping of Rabi oscillations (Ramsay et al. 2010).

The pure dephasing rate usually represents a small fraction of the decay rate at cryogenic temperatures (Uppu et al. 2020b) and can be modified by the nanostructure dimensions (Tighineanu et al. 2018) or reducing phonon occupation with clamping (Dreeßen et al. 2018). Another way to mitigate the effect of phonon dephasing is to enhance the decay rate through Purcell enhancement by modifying the local density of states with photonic nanostructure, introduced in Chapter 2.

1.5.2 Spectral diffusion

Pure dephasing arising from elastic phonon scattering and occurring within the lifetime of the quantum dot does not change the frequency of the emitted photon in the ZPL. In contrast, noises occurring over a slower timescale can randomly shift the energy level of the two-level system with respect to the driving laser and leads to the emission of slightly detuned photons. Such random slow noise originates from surface traps (Liu et al. 2018), charge noise, or nuclear spin noise (Kuhlmann et al. 2015). The averaged effect of this stochastic noise can be seen in countrate fluctuations beyond the shot noise (Konthasinghe et al. 2012a), linewidth broadening, and narrowing of the second-order coherence function.

In all the functions derived in section 1.3, the laser detuning Δ can be used to include a normal distribution of detuning with average $\overline{\Delta} = 0$ and standard deviation σ, and perform an ensemble average over the quantity of interest. For example, we show in Fig. 1.7(a) the absorption lineshape of a two-level system driven at $\Omega = 0.2\gamma$, with a dephasing rate of $\gamma_d = 0.2\gamma$ and spectral diffusion of width $\sigma = \gamma$. The maximum population of the excited state decreases, and the spectra width increases. This can be modeled with a Voigt function, which is the convolution of a Lorentzian with a Gaussian curve, with Lorentzian linewidth given by $\Gamma_{\text{Lor}} = \Delta_{\text{FHWM}}/2 = \gamma/2 + \gamma_d$ in the low-power limit. Spectral diffusion also impacts the saturation behavior of the two-level system, as shown in Fig. 1.7(b), by increasing the power needed to reach saturation. Finally, to assess the impact on the second-order coherence function, the Python Qutip package (Johansson et al. 2012) is employed to solve the master equation dynamic with $\Delta \neq 0$. The result is shown in Fig. 1.7(c) and reveals that a system undergoing spectral diffusion shows a narrower antibunching dip in the steady-state limit. When measuring the second-order correlation function with cw-excitation, the value at zero time delay is strongly dependent on the time response of the detection system, and in this case, a narrowing of the antibunching dip may lead to non-zero $g^{(2)}(0)$ (Konthasinghe et al. 2012b).

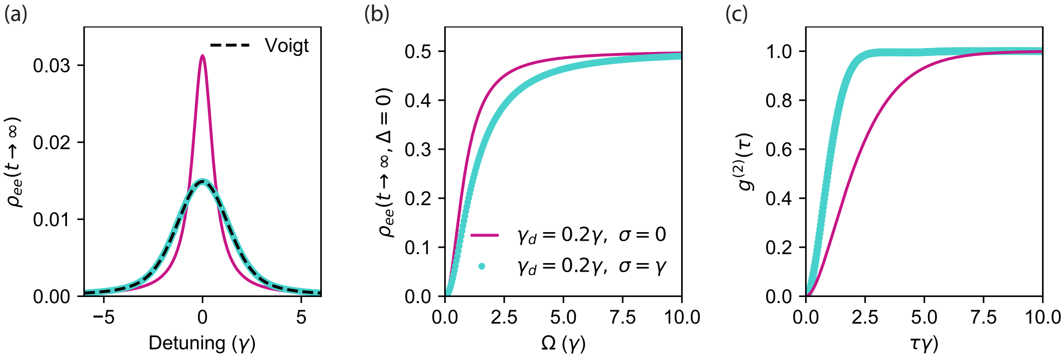

FIGURE 1.7: Effect of spectral diffusion on the resonance fluorescence of a two-level system. (a) The absorption spectrum broadens to a Voigt function, for $\Omega = 0.2\gamma$, when spectral diffusion, characterized by $\sigma = \gamma$, impacts the system. (b) The saturation plateau is reached for higher power in the presence of spectral diffusion. (c) The second-order correlation function for a two-level system is affected by spectral diffusion (blue dots), which shows a narrowing of the antibunching dip.

Spectral diffusion is, of course, a noise source that is not desirable because it reduces the coherence of the emission in the long term and limits the scalability of the quantum dot platform. As mentioned earlier, spin and charge noise are the main sources of spectral diffusion. It has been shown that the neutral exciton is only sensitive to spin noise to the second order, as opposed to the charged excitons (Kuhlmann et al. 2015). This is the positive impact of the fine structure of the neutral exciton since the optical dipoles possess zero net magnetic spin. Throughout this work, we, therefore, focus on single-photon sources based on neutral exciton. Moreover, the emission of the neutral exciton is linearly polarized, even at zero magnetic field, in opposition to the charge excitons. This makes the interaction with photonic nanostructures efficient, as will be developed in Chapter 2.

Neutral excitons are, however, sensitive to charge noise in the same way as charged excitons. The microscopic description of the charge noise is still not fully understood, but it can be visualized as random charges being trapped close to the quantum dot. Being embedded in a solid-state platform has the drawback that the background environment is not quiet, and quantum dots are sensitive to time-varying electric fields due to their electrical dipole. However, the GaAs platform also brings a solution to this problem, as it is possible to apply a controlled electric field to suppress the flow of charges across the quantum dot.

1.6 Electrical tuning of quantum dots

A quantum dot can be embedded in a p-i-n junction by the epitaxial growth of doped layers of GaAs on top and below a layer of intrinsic GaAs, as shown in Fig. 1.8(a), which pins the Fermi level at the n-contact. As a result, there is a built-in voltage in the thin membrane of $V_{\mathrm{bi}} = 1.54$ V at 4 K. When no external field is applied, the electric field across the quantum dot is too high to trap a charge state (Löbl et al. 2017). Applying a positive bias will lower the diode's built-in field and allow the quantum dot's loading with a single charge state. This regime is called the Coulomb blockade (Warburton 2013), and due to Coulomb interaction, only individual charge states can be loaded at a time. This can be done without having a flow of charges through the quantum dot in forward bias, thanks to a thick AlGaAs barrier.

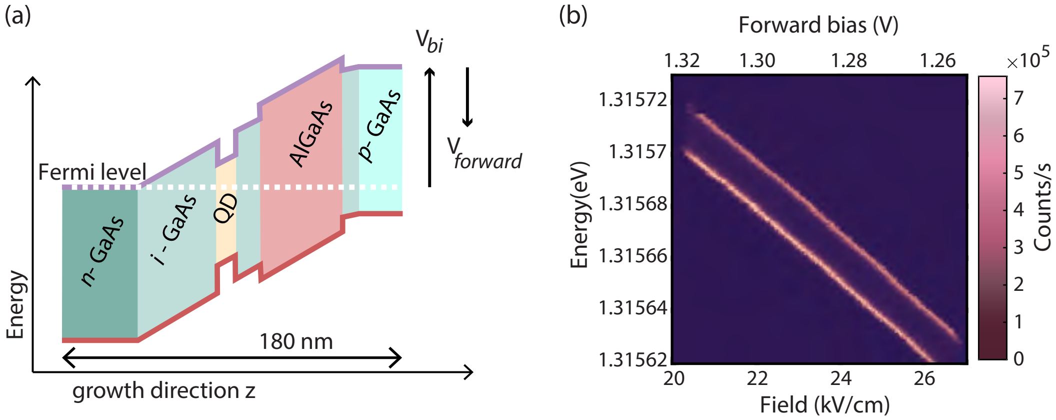

FIGURE 1.8: Electric field across a quantum dot (QD). (a) Band diagram of a QD embedded in a p-i-n junction. An external bias is applied to modify the band bending and is used to load the charge state in the QD. (b) Example of the resonance fluorescence spectra as a function of the bias voltage applied on the p-i-n diode. The two dipoles of a neutral exciton of a single QD are visible. Their energy can be tuned by applying a voltage or changing the field across the QD through the quantum-confined Stark effect.

Another advantage to this mechanism is the possibility to tune the energy of the quantum dot, due to the band bending, through the quantum-confined Stark effect in quantum dots (Warburton et al. 2002). The shift of energy as a function of an external field is written as

$$\delta E = -pF + \beta F^2, \tag{1.22}$$

where $F = (V_{bi} - V)/h_i$, with h_i being the thickness of the intrinsic part, p is the permanent dipole given by $e.r$, e being the electron charge and r the separation between the electron and the hole, and β is the polarizability, which indicates how easy it is to pull the hole and the electron wavefunction apart from each other. An example of such tuning is shown in Fig. 1.8(b), where we performed resonance fluorescence of a neutral exciton exhibiting two dipoles. The energy of each transition tunes as the voltage increases (field decreases) over an energy range $\approx 80\ \mu$ eV. This tuning range is limited by the lack of a second AlGaAs barrier after the QD, which is needed to increase the tuning range to a couple of nanometers (Kiršanskė et al. 2017). Moreover, the two lines tune parallelly, a typical effect of the two optical dipoles (Högele et al. 2004), which helps identify the charge state excited. The lever effect on the frequency is on the order of $0.4 - 0.7$ GHz/mV. The tuning mechanism can also be used to charge the quantum dot with single extra charges, like a hole or electron (Warburton 2013), but it is not investigated in this thesis.

* * *

In this chapter, we introduced the solid-state emitter enabling quantum optic experiment on a chip, generating highly coherent single photons through resonant excitation. In practice, realizing resonant excitation can be challenging since the laser is at the same frequency as the single photons and must be filtered from the signal. Other techniques have relied on quasi-resonant excitation (Thomas et al. 2021) or cascaded emission (Sbresny et al. 2022) for generating single photons with a large signal-to-noise ratio. In the next chapter, we will introduce the modifications to the dielectric environment of the quantum dot that enable controlling the emission dynamics and realizing efficient and convenient resonant excitation.

2 Integrated deterministic single-photon sources

In the previous chapter, we introduced the atom-like optical properties of quantum dots, resulting in the emission of single photons upon interaction with a laser field. There we assumed that the quantum dot decays over a given lifetime, but we lack an understanding of the influence of the dielectric environment on the emission time constant. As quantum dots are embedded in a chip, the engineering of the dielectric environment is possible by integrating them into a photonic nanostructure. The light-matter interaction is enhanced, thereby mitigating the effect of pure dephasing (Lodahl et al. 2015). Moreover, defining nanostructures allows us to isolate a single guided mode, such that the quantum dot emits single photons into a chosen channel with a probability close to unity (Arcari et al. 2014). Photonic structures are, therefore, an efficient method to capture emission from a quantum dot, which otherwise emits photons in the 4π-solid angle.

In this chapter, we introduce the coupling to optical modes and the link to the different photonic nanostructures in suspended membranes. We will go over the current state-of-the-art on a deterministic generation of pure and indistinguishable single photons, which spans quantum dots combined with photonic crystal waveguides, micro- and nano-cavities. We will then assess these platforms on their potential to scale up to multiple integrated single-photon sources and introduce the fully waveguide-based single-photon source.

2.1 Deterministic light-matter interaction in suspended waveguides

A fascinating result of the theory of light-matter interaction is that an excited atom, or any two-level system, even undisturbed, will eventually emit a photon due to the vacuum fluctuations through spontaneous emission. In Chapter 1, we treated the interaction of a two-level system with a semi-classical field, neglecting the reservoir modes. Here the coupling to radiation modes can be formally introduced by describing the interaction of a dipole emitter with an ensemble of quantized optical modes with different wavevectors k at the dipole's position through the dipole interaction. Without covering the full derivation, available in (Lodahl et al. 2015), in the Wigner-Weisskopf approximation, where the reservoir frequency response is assumed to vary insignificantly over the emitter linewidth, the excited state decays exponentially at a radiative rate

$$\gamma = \frac{\pi d^2}{\hbar \epsilon_0} \omega_0 \rho(r_0, \omega_0, \hat{\mathbf{e}}_\mathbf{d}), \tag{2.1}$$

where d is the dipole of the optical transition, ω_0 its frequency, and $\rho(r_0, \omega_0, \hat{\mathbf{e}}_\mathbf{d})$ is the local density of state, *LDOS*, a metric to quantify the number of available modes per unit mode volume at the position and frequency of the optical transition. The LDOS depends explicitly on the projection of the dipole polarization $\hat{\mathbf{e}}_\mathbf{d}$ on the normalized mode functions $\mathbf{u}_\mathbf{k}$ of the electric field, $\rho \propto |\hat{\mathbf{e}}_\mathbf{d} \cdot \mathbf{u}_\mathbf{k}|^2$, such that knowing the profile of the mode along the different dipole orientations indicates the coupling strength. Modifying the LDOS, therefore, either enhances or inhibits the decay rate through the Purcell factor, defined as

$$F_p(r_0, w, \hat{e}_d) = \frac{\gamma(r_0, \omega_0, \hat{e}_d)}{\gamma^{\text{hom}}(\omega_0)}, \tag{2.2}$$

where the denominator expresses the decay rate of a dipole within a homogeneous medium of refractive index n, given by $\gamma^{\text{hom}}(\omega_0) = \frac{n\omega_0 d^2}{3\pi\epsilon_0\hbar c^3}$. In bulk GaAs, with $n = 3.48$ for $2\pi c/\omega_0 = 930$ nm and a temperature of 10 K, the homogeneous decay rate is around $\gamma^{\text{hom}} = 1\ \text{ns}^{-1}$. Large Purcell factors are possible in nanostructures where the LDOS is enhanced.

2.1.1 Photonic crystal waveguide

Photonic crystal waveguides are excellent structures to enable large Purcell enhancement. The LDOS is modified by defining a periodic modulation of the refractive index with lattice constant a by removing holes of material of radius r around a strip of material, called a waveguide, as shown in Fig. 2.1(a). The modes propagating in this waveguide can be defined by Bloch mode. Similarly to the band diagram of semiconductors, the dispersion relation shown in Fig. 2.1(b) reveals a bandgap in energy for TE modes, where no light can propagate (Joannopoulos et al. 2008). At these frequencies, the LDOS is strongly suppressed, and the emission from QDs is inhibited (Julsgaard et al. 2008). The dispersion relation is shown for the first Brillouin zone and projected onto the direction of propagation along the waveguide. Due to the bandgap, individual bands host a guided mode, and the in-plane propagation is confined to the waveguide area. By embedding the QDs in the center of a GaAs membrane, given the in-plane orientation of the optical dipole, the light-matter interaction is restricted to the TE-like modes of the nanostructures. The TM-like modes are therefore neglected in the calculations, as they only come into play for large strains contributing to light hole-heavy hole mixing (Yuan et al. 2018). The total internal reflection restricts the out-of-plane propagation, which, together with the lateral bandgap, forces the TE-mode to propagate along the waveguide direction, confined within its core. In this context, the LDOS $\rho(\omega)$ is proportional to the group index n_g, meaning $\rho(\omega) \propto n_g = \frac{c}{v_g} = c\frac{d\omega}{dk}^{-1}$. As a consequence, considering the fundamental mode M0 at the band edge of the Brillouin zone, where the dispersion relation is flat, the group index can reach large values, simulated to $n_g = 58$ (Javadi 2015). Experimentally, a Purcell factor $F_p = 9$ has been measured (Arcari et al. 2014).

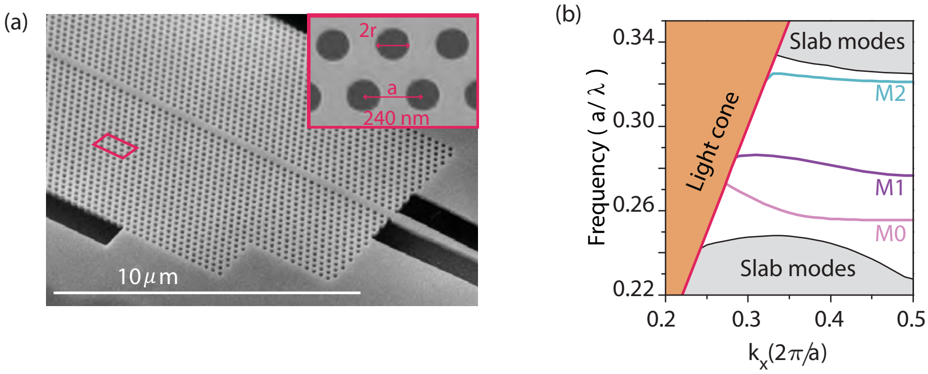

FIGURE 2.1: Photonic crystal for guiding light on a chip. (a) Scanning electron micrograph (SEM) of a photonic crystal where one row of holes is left out to define a waveguide. The lattice constant a and hole radius r influence the dispersion relation. (b) The periodicity of the refractive index modulation gives rise to a dispersion relation in bands, with a photonic bandgap in between allowed guided modes. The supported TE-like modes are shown, starting from the fundamental M0. Slab modes are not confined in the waveguide but are still bounded to the membrane. Reproduced from (Javadi 2015).

Defining a waveguide nanostructure supporting a single confined and guided mode restricts the possible decay channels for the quantum dot emission to a single, chosen one. Single photons can then be efficiently captured and routed for further experiments. The probability of emission into the waveguide mode is expressed by the β-factor as

$$\beta = \frac{\gamma_{\text{wg}}}{\gamma_{\text{wg}} + \gamma_{\text{rad}} + \gamma_{\text{nrad}}}, \tag{2.3}$$

where γ_{wg} is the decay rate into the waveguide mode, γ_{rad} the radiative decay rate into non-guided modes, e.g. leaky out-of-plane modes, and γ_{nrad} the non-radiative decay rate. The first decay rate γ_{wg} is enhanced in photonic crystal waveguides due to Purcell enhancement, while γ_{rad} is partially inhibited due to the photonic crystal bandgap. In this setting, β-factor $> 98\%$ has been achieved (Arcari et al. 2014) over a large bandwidth. As a consequence, quantum dots emit deterministically into the guided mode, leading to high photon countrates (Uppu et al. 2020b).

2.1.2 Nanobeam waveguide

In a simple photonic structure, a *nanobeam* waveguide, shown in Fig. 2.2(a), mode confinement is achieved by total internal reflection. Moreover, the width of the waveguide dictates the number of supported guided modes, as shown in Fig. 2.2(b). Unlike photonic crystals, nanobeam waveguides are continuously invariant under translation, so there is no energy bandgap. Therefore, the displayed dispersion relation is truncated and not related to a Brillouin zone. There are, however, energies for which no index-guided mode is supported, meaning that light with long wavelength is not bounded to the waveguide, they are in *cut-off*. A nanobeam waveguide of width $w = 450$ nm presents three TE-like modes, with each an effective refractive index n_{eff}, indicating how the wave is guided in the structure. The fundamental mode presents an effective refractive index closer to the material index, while the higher order modes will approach that of the cladding, in our case $n_{\text{air}} = 1$. The light cone represents the points of the dispersion relation where light is not bounded to the waveguide mode and is free to travel in all directions in the air.

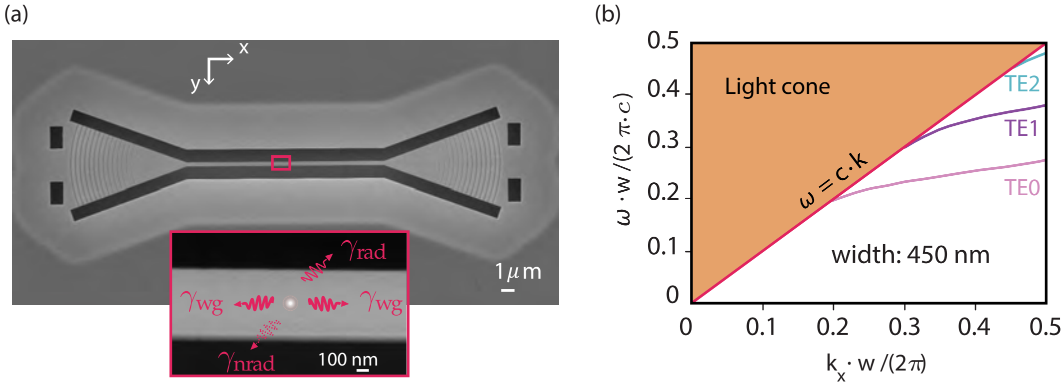

FIGURE 2.2: Nanobeam waveguide for guiding light on a chip. (a) SEM of a suspended nanobeam waveguide, the semiconductor analog of optical fiber. The inset indicates the different decay rates for evaluating the β-factor in Eq. 2.3.(b) Dispersion relation of a multimode waveguide of width $w = 450$ nm. Only TE-modes are shown and are each characterized by a refractive index n_{eff}, giving a linear relation dispersion. Reproduced from (Prindal-Nielsen 2017).

In a single-mode waveguide, corresponding to a width of 300 nm, only the TE0 is guided, and the other modes are set in the cut-off. In this configuration, a maximum β-factor of $96\ \%$ (Kiršanskė et al. 2017) can be achieved if the emitter is situated at the center of the waveguide, with a dipole oriented along the y-direction of the basis shown in Fig. 2.2(a). These structures do not provide a large Purcell factor, which can be slightly inhibited for y-dipole in the center of single-mode waveguides (Daveau 2016) and can reach $F_p = 1.7$ for large multimode waveguides (Thyrrestrup et al. 2018). They, however, offer a playground to vary the coupling to different guided modes depending on the position of the QD. This can be used to perform resonant excitation with one mode and collect single photons in another one, as will be introduced later in this chapter.

To illustrate the different coupling, we calculate the β-factors for a y-oriented and x-oriented dipole in a dual-mode waveguide of width 450 nm, meaning a waveguide sustaining the TE0 and TE1 mode. We then scan the position of the dipole across the waveguide, as depicted in Fig. 2.3(a). To this purpose, we follow the method used in (Rotenberg et al. 2017) to calculate the β-factor of a dipole in a slot waveguide ring. In this method, the power radiated by the dipole in one of the modes after propagation and the total power radiated by the dipole is simulated, and the ratio gives the β-factor. The calculation is performed using a three-dimensional finite-difference time-domain simulation (Taflove et al. 2005) with the open-source software package MEEP (Oskooi et al. 2010). The result is shown for different positions across the waveguide, for the y- and x-dipole, in Fig. 2.3(b). In the insets, the different projections of the modes are shown, which gives an indication of the expected β-factor, as the coupling is proportional to the projection of the electric field on the dipole orientation.

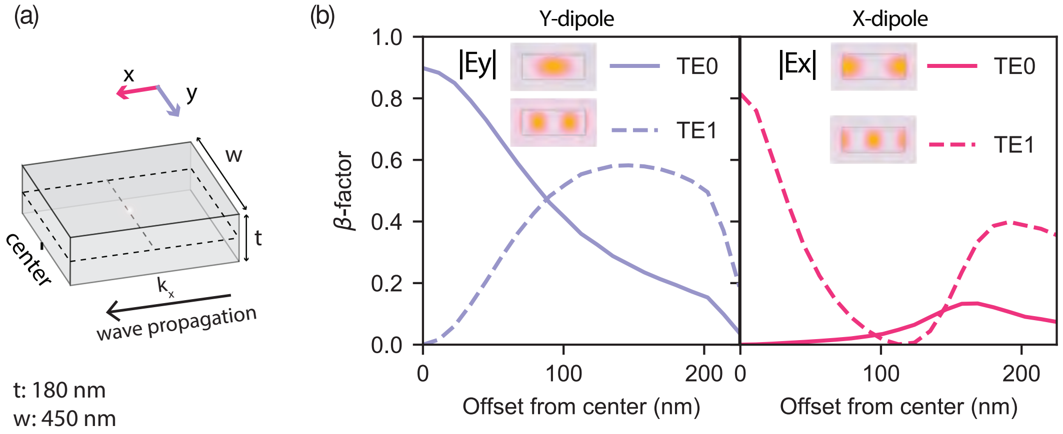

FIGURE 2.3: β-factor for a dual-mode waveguide. (a) A linear dipole, aligned along the x- or y- direction, is swept across the waveguide width. The radiated power is calculated in a three-dimensional finite-difference time-domain simulation. (b) Calculated β-factor for the y-dipole (left) and x-dipole (right) as a function of the offset from the waveguide center and for the TE0 and TE1 modes. The modes projection on the relevant axis is shown in the insets.

The y-dipole shows maximum coupling to the TE0 in the center of the waveguide, while the x-dipole is strongly suppressed at this position. An inverse tendency is observed for the coupling to the TE1 mode. Interestingly, this calculation shows that it should be possible to interact with the y-dipole with light coupled in the TE1 mode and collect single photons emitted in the TE0 if the quantum dot is off-centered (up to 100 nm). This effect has been exploited in Ref. (Uppu et al. 2020a) to enable a fully waveguide-based single-photon source, and we will introduce in detail the working principle in section 2.3.

Photonic nanostructures are a strong asset of the solid-state platform as they enable the control of the emitter dynamic and ensure strong light-matter interaction, leading to the deterministic generation of single photons. Photonic crystals and waveguides are significant structures of the planar photonic platform, and we will now cover the state-of-the-art of single-photon sources. To do so, we will introduce key properties necessary to compare different platforms to each other.

2.2 Single-photon sources based on quantum dots

From the first demonstration of single photons emitted by a quantum dot (Michler et al. 2000) to the first measurement of indistinguishability between two photons emitted by the same quantum dot (Santori et al. 2002), the properties of the QD-based (quantum dot-based) single-photon sources are constantly improving. An ideal source should be bright, or efficient, so that a single photon is detected each time the quantum dot is triggered with a laser pulse. The deterministic character of the photon-emitter interaction offers high brightness of the single-photon stream and can be quantified with the β-factor. Together with high single-photon purity, linked to the probability of emitting at most one photon, and photon indistinguishability, which is the degree to which the wavefunction of each emitted photon overlaps, it makes this platform especially promising for applications within quantum information. We will here review the key enabling properties and give an overview of the leading quantum photonic platform based on InAs quantum dots (Michler 2017).

2.2.1 Key properties

Out of all requirements, **brightness** is where QD-based single-photon sources excel. Indeed, due to the large dipole moment, quantum dots present a significant oscillator strength, contributing to the high generation rate of single photons. Moreover, due to the strong-light matter interaction, the effect of coupling to non-radiative states is strongly suppressed and ensures a high quantum efficiency (Uppu et al. 2020b). Finally, the interface with strongly confined guided modes in nanophotonic devices enables deterministic emission into a chosen mode. In summary, from the quantum dot perspective, fundamental aspects contributing to brightness are well understood and are not limiting factors. The remaining challenge resides in interfacing the photons coupled to the guided mode to measurement channels, e.g. optical fibers for detection. Most of the photon loss happens at the outcoupling stage due to mode mismatch between the sub-micrometer mode field diameter of the nanophotonic structures and the optical fibers. Bridging this gap has been the focus of optimization over recent years. This interface is also needed since GaAs is a high-refractive-index material, so light is strongly confined and is therefore difficult to extract out of the material. Typically the source efficiency is evaluated by comparing the photon countrate in the collection fiber to the repetition rate of the pulsed laser used for excitation. Efficiency is an essential feature for quantum photonic technologies to ensure a high success rate of multi-photon protocols (Wang et al. 2019a; Uppu et al. 2020b).

The collected signals must be constituted solely of **pure** single photons, as otherwise, the advantage given by this resource will be spoiled for quantum information applications. The correct quantity to evaluate is the value of the second-order correlation function at zero time delay, $g^{(2)}(\tau = 0)$. It is best evaluated in pulsed excitation, as it encompasses how well the pulsed excitation laser is filtered and also the probability of multi-photon emission due to re-excitation within the pulse duration (Fischer et al. 2017). Accordingly, the value $g^{(2)}(\tau = 0)$ indicates the probability of detecting more than one photon within the same excitation pulse, and the purity can be defined as $P = 1 - g^{(2)}(0)$. This quantity is, however, not impacted by the loss of photons, or in other words by the presence of vacuum states, and is therefore not equal to the fidelity to a pure Fock-state $|1\rangle$.

Finally, for most quantum information applications, the generated single photons must be as **indistinguishable** as possible, pair-wise. This measurement is the ultimate test of the suppression of decoherence on the quantum dot, and on a short time scale, it is mainly sensitive to phonon dephasing. Other noise sources, such as charge noise, happen over a long time scale and therefore do not impair the indistinguishability of two consecutively emitted photons from a single quantum dot. Slow noise will, however, limit how many photons can be emitted with high indistinguishability. The latter is best measured with pulsed excitation, as in this case it is given by the visibility of the Hong-Ou-Mandel interference. Additionally to decoherence, the measured indistinguishability is limited by the non-perfect purity, which reflects the signal-to-noise ratio. A correction to the raw indistinguishability can be made such that multi-photon contribution and setup imperfection can be accounted for (Santori et al. 2002; Ollivier et al. 2021).

These are the three requirements we will base our review of QD-based single-photon sources that are available to date, or in development.

2.2.2 State-of-the-art

We can distinguish two types of single-photon sources, those relying on vertical cavities and those based on planar waveguides. We will start from the latter, as a natural continuation of the introduction about waveguides.

Resonant excitation of quantum dot embedded in a **photonic crystal waveguide**, shown in Fig. 2.4(a), was recently performed and demonstrated the generation of a string of more than 100 photons with 93% raw indistinguishability from the neutral exciton transition (Uppu et al. 2020b). The advantage of this nanophotonic structure is that the Purcell enhancement, which allows for mitigating the effect of pure dephasing, is relatively broadband, so tuning the resonance of the transition is unnecessary. Another advantage is that the emitted photons are coupled with high probability, β-factor, to the guided mode and can be collected at a different port through a shallow-etched grating coupler (Zhou et al. 2018), which allows scattering light vertically. More device about this detail is given in Chapter 3. The spatial separation of the excitation laser, exciting the quantum dot from the top, and the collection port ensures high laser suppression without sacrificing counts due to polarization filtering, highlighted by the low $g^{(2)}(0) = 0.015 \pm 0.005$. After correcting for the multi-photon contribution and setup imperfection, the intrinsic visibility is 96%. The in-fiber source efficiency is limited to 7%, where the most significant loss contribution arises from the setup efficiency, which can be directly tackled, while the on-chip source efficiency is estimated to be 84%.

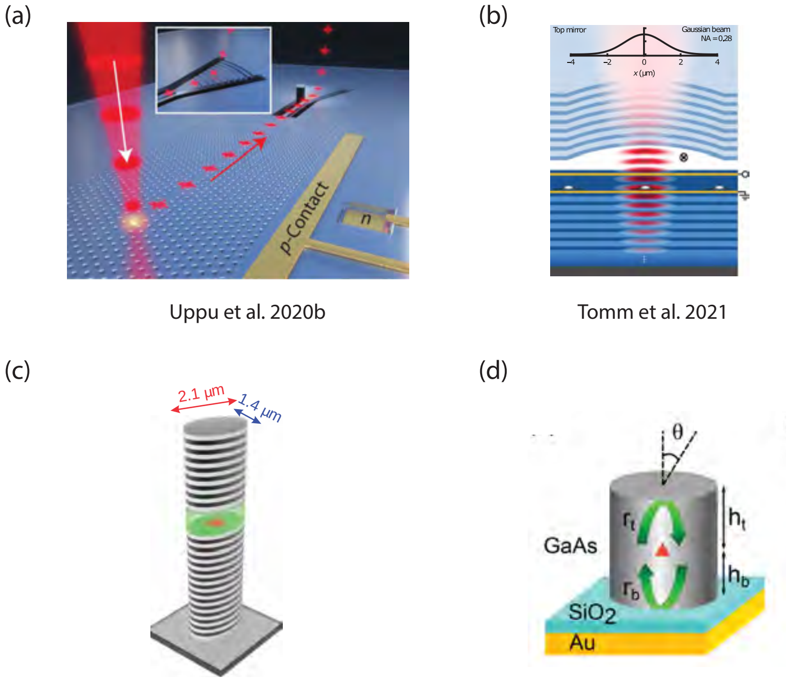

Uppu et al. 2020b

Tomm et al. 2021

Wang et al. 2019

Kotal et al. 2021

FIGURE 2.4: Single-photon sources based on InAs quantum dots. (a)Photonic crystal waveguide. (b) Open microcavity. (c) Vertical pillar with microcavity. (d) Nanowire with nanocavity.

Another demonstration exploits the resonant excitation of a positively charged exciton embedded in an **open microcavity**, shown in Fig. 2.4(b). This photonic structure comprises distributed Bragg gratings (DBR) at the bottom and a coated concave glass mirror at the top (Tomm et al. 2021). This assembly forms a cavity mode with a maximum at the location of the quantum dot and, in the weak coupling regime, allows strong Purcell enhancement of 10 in the Gaussian mode of the cavity. This leads to high extraction efficiency, with 57% coupling of single photons in the fiber, the current world record in in-fiber brightness. By externally controlling the position of the top mirror, it is possible to bring the quantum dot into spectral and spatial resonance. In these conditions, low multi-photon generation was demonstrated ($g^{(2)}(0) = 0.021$) with a high corrected indistinguishability of 97.5%. The birefringence of the cavity allows the use of the mode that is weakly coupled to the quantum dot to excite the transition resonantly while collecting in the orthogonal cavity mode, hence ensuring good laser suppression without sacrificing counts. The β-factor is, however, limited in this realization to 86%.

The birefringence of a microcavity is also exploited in **micropillars cavity**, shown in Fig. 2.4(c). The resonant excitation of a negatively charged exciton was performed with a $g^{(2)}(0) = 0.025$ (Wang et al. 2019b) but with a more modest extraction efficiency. Moreover, the lack of electrical gates limits the indistinguishability between consecutively emitted photons. Other works on micropillars have implemented electrical gates to ensure higher indistinguishability (Somaschi et al. 2016). The presence of the p-i-n junction also allows frequency-tuning of the quantum dot transition in resonance with the narrow-band cavity.

Finally, **nanocavities** in nanowires, sketched in Fig. 2.4(d), are good candidates to provide strong Purcell enhancement with a broadband response, with a calculated β-factor of 95% over 100 nm (Kotal et al. 2021), leading to a robust extraction efficiency. As experiments were done with above-band excitation, photon purity and indistinguishability have not yet been measured.

These works, in their vast majority, have achieved strong light-matter interaction such that most of the excitation pulses convert into the emission of single photons in the nanostructure. The challenge of achieving higher extraction efficiency is still present, but it boils down to classical photonic and optic engineering. The control over noise sources is getting better, mainly due to the diode for mitigating the effect of charge noise (Kuhlmann et al. 2015; Thyrrestrup et al. 2018), highlighted by the long string of single photons emitted without loss of coherence (Uppu et al. 2020b). Given the size of the fabricated chips, typically 10×10 mm^2 , there is space for hundreds of devices, which could be operated simultaneously, thus leading to multiple strings of single photons generated in parallel.

2.2.3 Prospect for scaling up single-photon sources on chip

One roadblock towards the on-chip generation of multi-photon states from multiple bright single-photon sources is that quantum dots nucleate randomly. Therefore, the position in the nanostructure will not always be optimal to ensure a high β-factor and the best extraction efficiency. Moreover, the emission wavelength varies from quantum dot to quantum dot, which implies a need for individual wavelength tuning. The alternative method relies on the temporal-to-spatial demultiplexing of a train of single photons emitted by a single quantum dot source (Hummel et al. 2019), which has been realized for $N = 20$ photons with bulk optics (Wang et al. 2019a). However, increasing the number of modes (Zhong et al. 2020) is complex due to switching losses and the size of the required setup. Integrated circuits seem then a natural solution for performing the demultiplexing experiment (Lenzini et al. 2017). But here again, we encounter upscaling challenges due to switching losses and, more importantly, losses linked to on-chip optical delays, which are necessary for full integration with the source.

Recent demonstrations of large-scale integration on different planar photonic platforms give a hopeful prospect. To name a few, eight color centers in diamonds were reproducibly integrated into SiN circuits (Wan et al. 2020), while six quantum dots in nanowires were interfaced successfully with AlN waveguides (Elshaari et al. 2017). These experiments demonstrate that improvement in fabrication yield allows to realistically integrate more than one single-photon source. Deterministic fabrication around pre-localized quantum dots (Ollivier et al. 2020; Pregnolato et al. 2020) can also be used to boost the integration yield, which in turn demands a large experimental overhead in device design around pre-localized quantum dots. Instead, the success probability of integrating multiple low-noise quantum dots can rely on moderate quantum dots density and broadband nanostructures (Pedersen et al. 2020).

To mitigate the effect of inhomogeneous broadening and to bring multiple quantum dots in resonance, a tuning mechanism is necessary. A solution is to employ individual dc-Stark tuning of different quantum dots (Petruzzella et al. 2018; Ellis et al. 2018). Other tuning mechanisms, such as strain tuning (Grim et al. 2019), can also be exploited. Finally, slow random noise also compromises the upscaling of single-photon sources, which can be tackled with active feedback on the dc-voltage applied to the quantum dots (Hansom et al. 2014).

A missing requirement is a possibility of exciting resonantly multiple sources in a compact way. Indeed, in all the works introduced above, the resonant excitation relies on the careful alignment of a pump laser's spatial position and polarization to ensure good laser suppression. Moreover, distributing a single laser to multiple sources is a non-trivial task and can be realized only with several external controls (mirrors, waveplate) and spatial light modulators. Therefore, a device that takes into account the distribution and filtering of the pump laser is needed for truly scalable single-photon sources.

2.3 Scalable waveguide-based single-photon sources

Recent work demonstrated a fully waveguide-based single-photon source that incorporates the distribution of a pump laser (Uppu et al. 2020a). Resonant excitation of a quantum dot is performed through the waveguide, and the laser is filtered in the circuit to ensure excellent laser suppression. The device is based on a dual-mode waveguide, supporting two orthogonal modes TE0 and TE1. This allows exciting quantum dots in the waveguide with the latter and to collect the single photons emitted in the former, as shown in Fig. 2.5(a). The pump laser, coupled in the TE1, is subsequently filtered by tapering the waveguide width and setting the mode in the cut-off.

The calculation of the β-factor for the two modes was shown in Fig. 2.3 and revealed a strong dependence of the coupling strength on the lateral position of the quantum dot and its dipole orientation. This contrast is used to excite an off-centered quantum dot with the TE1 mode while ensuring a high emission probability into the TE0 mode. The probability of this event is shown as the product of the two β-factors in Fig. 2.5(b). It is dominant for the y-dipole as long as it is within ± 100nm from the waveguide center. We discard the gray region, as we want the coupling to the TE0 mode to be higher than the coupling to the TE1, to ensure high efficiency of the single-photon collection.

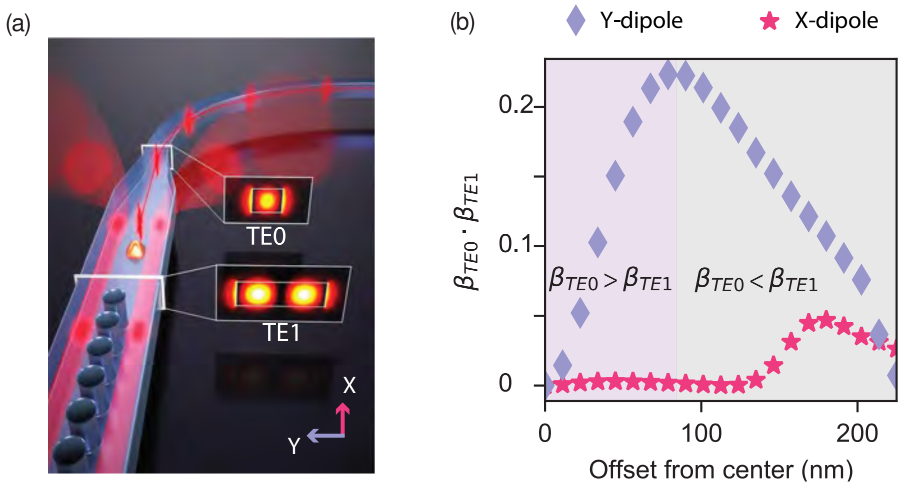

FIGURE 2.5: "Plug-and-play" device for the resonant excitation of quantum dots in a dual-mode waveguide. (a) Artistic image of the device demonstrated in (Uppu et al. 2020a). The two orthogonal modes of a dual-mode waveguide are employed. The TE1 mode excites the quantum dot and is afterward filtered. The single photons are predominantly emitted in the TE0 mode. (b) The probability of such an event is proportional to the product of the β-factors to the TE0 and TE1 modes. This product depends on the lateral position of the quantum dot. The purple region shows the region of interest.

The success of this device relies on the possibility of coupling the laser to the TE1 mode, propagating at the emitter section, without coupling to the TE0 mode. To achieve this, a y-splitter followed by a photonic crystal filter is used, as depicted in Fig. 2.6. The laser is launched through a shallow-etched grating into the single-mode waveguide of a symmetric y-splitter, which excites a superposition of the TE0 and TE1 modes of the dual-mode waveguide attached at the output of the y-splitter. It is followed by a photonic crystal which, from design ($r = 70$ nm and $a = 210$ nm), allows the TE1 mode to propagate further while the TE0 mode is reflected back. The left inset of Fig. 2.6 shows the simulated transmission after a photonic crystal with 20 holes. We note the strong suppression of the TE0 transmission compared to TE1 transmission over a 20 nm bandwidth around 950 nm, quantified by T_p.

The pump laser in TE1 reaches the emitter section and excites an off-centered quantum dot. The laser photons are then filtered by combining an adiabatic taper and a bend. In this condition, the TE1 mode reaches cut-off and leaks out of the structure. Single photons emitted in the TE0 mode are free to propagate loss-less. The impurity ξ, defined as the ratio between the residual pump photon and the single photons emitted, is calculated at the end of the circuit as $\xi = \frac{2T_p}{\beta_{\text{TE1}}\beta_{\text{TE0}}}$. It is shown in the right inset of Fig. 2.6 for a y-dipole and a laser pump suppression $T_p = 2.10^{-5}$. From this calculation, the optimal position of the quantum dot is between $50 - 100$ nm from the center. Finally, the photonic crystal also has the function to reflect back to the output port the single photons that are traveling backward. In this way, the single-photon emission is unidirectional, and efficiency is preserved. Further details on design and simulation can be found in Ref. (Uğurlu 2021).

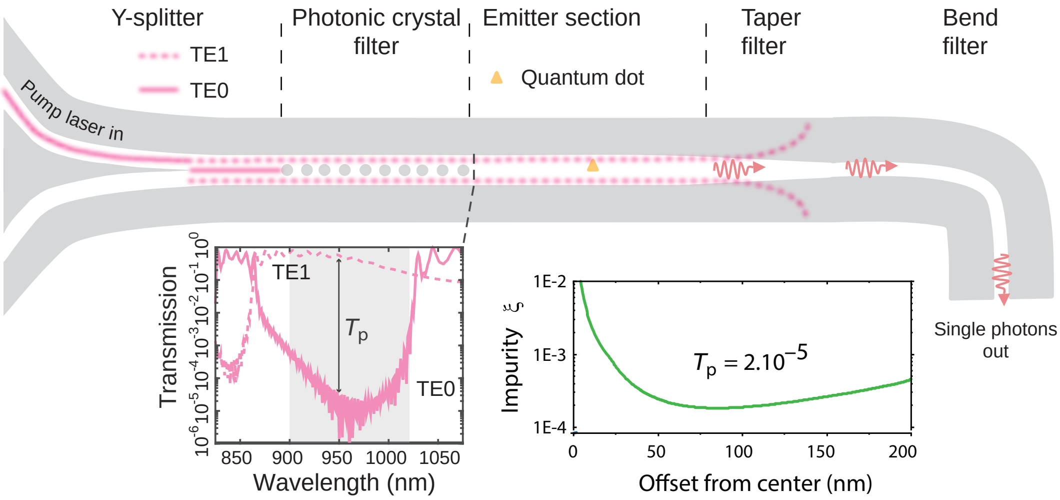

FIGURE 2.6: Working principle of the waveguide-assisted resonant excitation scheme. A pump laser, pulsed or continuous-wave, is coupled into one branch of a y-splitter. At its output, the laser is prepared into a superposition of TE0 and TE1. The photonic crystal filter reflects the TE0 and transmits the TE1 mode with low loss. The transmission of the TE0 mode compared to the TE1 is shown in the left inset. The laser interacts with the quantum dot at the emitter section. The quantum dot re-emits predominantly in the TE0 mode of the waveguide, with a β-factor depending on the lateral position. The laser in TE1 is filtered by adiabatically tapering the waveguide followed by a bend. The impurity ξ, the ratio between laser photons and single photons emitted at the device output, is given as a function of the quantum dot position (right inset). Calculations adapted from (Uppu et al. 2020a).

This device provides a simple way to distribute a laser for exciting quantum dots in a waveguide without having to explore a parameter space of position, angle, and polarization of the laser. Finding resonant quantum dots boils down to scanning the frequency of the resonant laser after coupling it into this "plug-and-play" device. This was successfully achieved in (Uppu et al. 2020a) with the resonant excitation of one dipole of a neutral exciton with a low $g^{(2)}(0) = 0.020 \pm 0.005$, at π-pulse. The quantum dot coupling efficiency to the TE0 mode was 80%, and a high degree of indistinguishability, 91% without correction, was measured. In this case, the output of the device was terminated by a grating coupler such that light can be scattered off chip and detected.

* * *

This "plug-and-play" device allows the compact distribution of a resonant pump laser to scale up the number of addressable single-photon sources. In the traditional top excitation, a laser's position, angle, and polarization must be adjusted for each quantum dot, as illustrated in Fig. 2.7(a). Instead, a single laser may be distributed on-chip to several waveguide-based single-photon sources, thereby greatly reducing the overhead of laser alignment and quantum dot search, as pictured in Fig. 2.7(b).

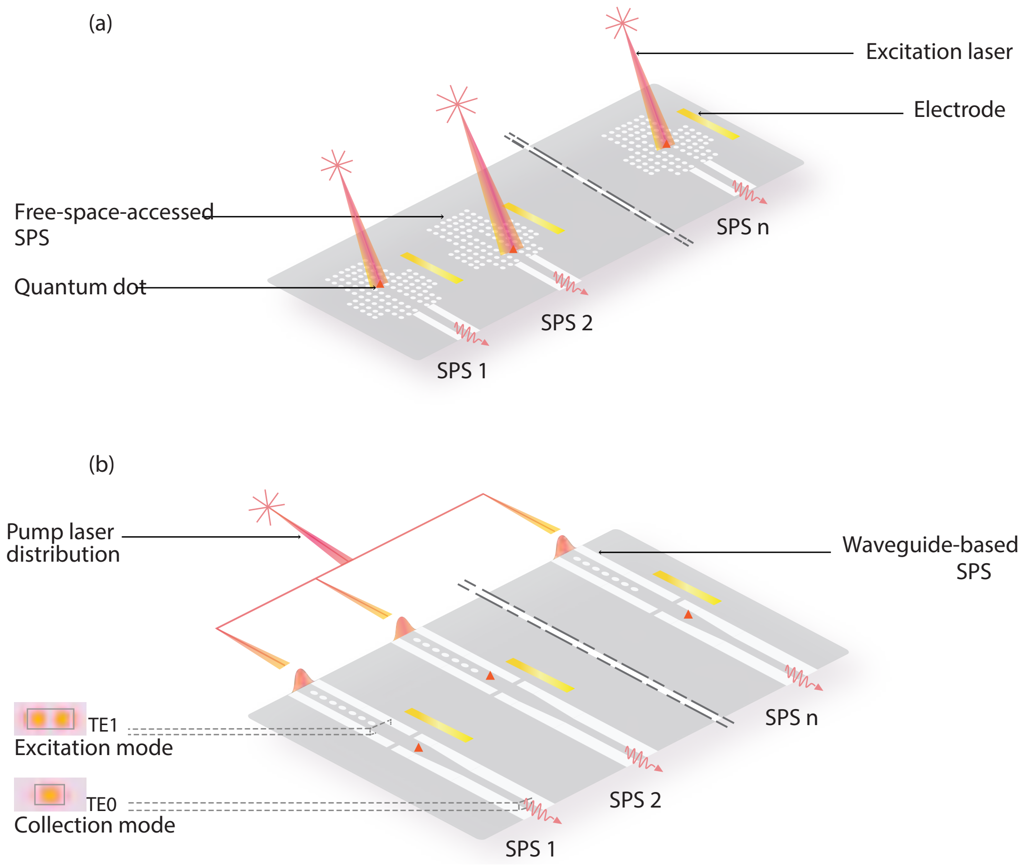

FIGURE 2.7: Resonant excitation and operation of multiple waveguide-integrated single-photon sources for a multi-photon generation. (a) Sketch of the standard top excitation approach. Each quantum dot (QD) is excited with individual laser pulses coupled from the top through leaky waveguide modes. (b) A fully circuit-based scheme, where a single laser source is distributed on-chip (not shown) to n waveguide-based single-photon sources (SPS). Resonant excitation is performed via parallel "plug-and-play" devices. Independent electrical tuning of the QDs is implemented to account for spectral inhomogeneities. This scheme provides a spatially demultiplexed source of single photons, readily available for multi-photon experiments.

We utilize this scheme in Chapter 4 for the simultaneous resonant excitation of two waveguide-based single-photon sources as a showcase towards the scalable generation of demultiplexed single-photon streams. To this end, we need to develop the circuit element enabling the on-chip laser distribution. Moreover, we need to implement individual tuning of quantum dots. These specific requirements and other generic considerations for fabricating scalable devices are covered in the next chapter.

3 Design and fabrication of scalable quantum photonic circuits

The realization of advanced quantum photonic circuits relies greatly on the optimization of nanofabrication techniques. Beyond the requirement of the excellent quality of the wafer growth, during which quantum dots nucleate, photonic nanostructures must be fabricated with high resolution and in a reproducible fashion. To do so, we use a soft-mask method to fabricate patterns with electron-beam lithography (Midolo et al. 2015), described in this chapter. We also dedicate some time to fabrication and design optimization, focusing on decreasing fabrication-induced optical losses. Finally, we introduce tailored designs to realize the simultaneous excitation of multiple waveguide-based single-photon sources.

3.1 Fabrication at the nanometer scale

In Chapter 2, several types of photonic structures were introduced, which provide light-matter interaction at the nanometer scale. In Fig. 3.1, we show the sketched cross section of a nanophotonic device fabricated in doped GaAs membrane ≈ 180 nm-thick (top). Such a device can be, for example, a nanobeam waveguide terminated by a photonic crystal at one end and shallow-etched gratings at the other end (bottom). Several steps are required to define such a device in the p-i-n GaAs membrane. Most of the techniques rely on a top-down approach. First of all, to apply an electric field across the membrane, it is necessary to fabricate metallic contacts on the p- and n- layers, so vias need to be opened to access the buried doped layer. Then, shallow-etched gratings and other shallow-etched features necessitate depth-controlled material removal. The target depth is approximately 50 nm in the last groove of the shallow-etched gratings. Nanobeam waveguides and photonic crystals are features presenting a large aspect ratio and therefore need to be transferred to the membrane with a highly-directional etching. Finally, the index contrast must be maximized all around the waveguides for the best light confinement within the photonic structures. The structures are therefore suspended by removing a sacrificial layer below the membrane containing the quantum dots.

To transfer patterns, a stencil is defined by lithography on a resist, followed by material removal through etching. Due to the diffraction limit, UV-photolithography techniques cannot reach the level of precision necessary to fabricate nanometer-scale photonic structures. Deep-UV techniques are only found in large-scale foundries due to the overhead these methods require. For research applications, electron beam lithography (EBL) allows going beyond the diffraction limit since the electron follows the de Broglie limit. In this way, depending on the energy provided to the electrons and the magnetic lens aberrations, a beam size of a few nanometers can define patterns on an electron-sensitive polymer resist. In our cleanroom, the EBL tool has an acceleration voltage of 125 keV, providing nanometer beam spot size. The resist used in this work is a positive resist (ZEP520), meaning that in the exposed areas the polymer chain breaks. Patterns are revealed after development in a cold developer (-5°C) for increased sensitivity, resolution, and edge smoothness (Ocola et al. 2006). A minimal electron dose is necessary to open a pattern and is provided by choosing the current for the acceleration of the electron and the time spent by the beam on each point of the pattern, called dwell time. Care is taken to calculate the exact dose necessary to open a certain pattern given the contribution of back-scattered electrons and secondary electrons, called proximity effect [1].

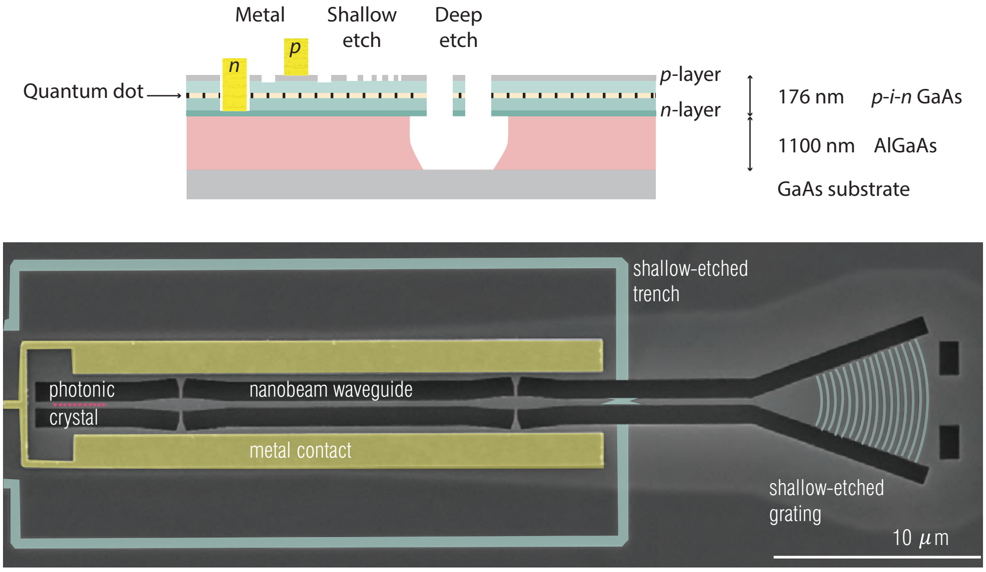

FIGURE 3.1: Top: Sketch of the wafer cross-section. It is composed of a p-i-n GaAs membrane with InAs quantum dots in its center, grown on top of a thick AlGaAs sacrificial layer. Bottom: Scanning electron micrograph (SEM) of a nanobeam waveguide with a localized metal contact, isolated from the rest of the chip using a shallow-etched trench. The metal contact is highlighted in yellow, the shallow-etched parts in light blue, and the photonic crystal in red.

Once the pattern is opened, different steps can be taken to transfer the patterns from the mask to the membrane. One of them consists of removing materials by depth-controlled dry etching for opening n-vias and shallow-etched features. This is done in a reactive-ion etcher (RIE), which creates a

---

[1] The Beamfox Proximity software is used for calculating the corrected dose.

plasma in a vacuum chamber and accelerates the ions towards the sample. The gas employed is halogen-based mixed with Argon, which ensures a contribution of selective chemical etching to GaAs with vertical profiles (Baca et al. 2005). The combination of chemical etching and physical ion bombarding removes layers of GaAs at a slow rate. The etch depth is controlled with laser interferometry, and approximately 50 nm is removed within 1 minute. This process ensures smooth sidewalls, which are necessary for defining shallow-etched gratings and trenches.

The transfer of waveguide and photonic crystals necessitates a larger contribution of physical etching to ensure high verticality of the patterns throughout the membrane, for features as narrow as 100 nm. This is achieved within the same RIE system, with an added inductively coupled plasma (ICP). A second large RF power is turned on to increase the kinetic energy of the dissociated ions. With a similar halogen-gas plasma, features with a large aspect ratio are defined before the soft-mask is sputtered away. This leads to a high anisotropic etching rate of 800 nm/min for GaAs.

As featured in Fig. 3.1, metallic pads need to be fabricated on p and n layers, together with narrower p-electrodes reaching the photonic structures. Again, a resist-mask is used after e-beam lithography to shadow the GaAs areas where metal should not be deposited. An electron-beam evaporator in a vacuum chamber is used to evaporate metal stacks onto the chip. The resist is subsequently removed, and with it, the unwanted metal part. The metalization step is performed before the lithography of the photonic devices.

Finally, the photonic structures are suspended by removing the AlGaAs sacrificial layer underneath the GaAs membrane. The AlGaAs layer is grown by molecular beam epitaxy before the GaAs membrane, and thanks to the matching lattice constant of the two semiconductors, this can be done close to strain-free. An AlGaAs layer with a high Al content is selectively etched by a hydrofluoric acid solution without etching the GaAs membrane. The isotropic etch rate depends on the HF concentration and Al percentage. An undercut of $3\,\mu$m is achieved by etching 25 s in 10% HF. This undercut length is necessary to suspend the photonic waveguides and shallow-etched gratings fully. The undercut is visible in Fig. 3.1 as they are with light gray contrast. Due to the fragility of suspended structures, the samples are dried with a critical point dryer (CPD) to avoid surface tension by eluding phase transition.

All fabrication details and exact recipes can be found in Ref. (Wang 2021) and constitute a standard workflow for the reproducible fabrication of gated quantum photonic devices. This level of control makes a vision of a large-scale planar quantum photonic platform possible. We need, however, to first address limiting factors in the photon loss and fabrication yield.

3.2 Efficiency optimization for scalability

The photonic chips developed on this quantum photonic platform find their purpose in generating single photons, carriers of quantum information, which implies stringent requirements on the efficiency (Bartolucci et al. 2021). The efficiency includes the generation of single photons, propagation on-chip, and outcoupling into fibers. Once the single photons are emitted from the quantum dots, which can be done with high efficiency as covered in Chapter 2, we need to track down loss sources, originating from propagation in the waveguide and outcoupling loss from the chip to an optical fiber. Also, to claim a scalable platform, the yield of fabrication of high quality structures is complementary to efficiency. Both the photonic and electrical parts of the device should be reproducible within the same chip and among different batches. In this section, we will cover the main challenges faced by the GaAs platform and a way to remediate them.

3.2.1 Propagation loss

GaAs is not the least lossy material to transmit light, as the smallest reported loss shows 1.6 dB/cm at a wavelength of 1550 nm. At this task, other materials, such as SiN and Silicon-on-insulator, are showing higher performance, with loss of approximately 2 dB/m (Liu et al. 2021) for the former material, and 30 dB/cm (Dong et al. 2010) to 4 dB/m (Bera et al. 2022) for the latter, characterized in the C-band. Of course, the strong advantage of quantum emitters in GaAs is undeniable, but the short emission wavelength, far from the ideal telecommunication band of 1550 nm, presents higher material absorption loss. Starting from this fact, we do not expect propagation loss on our platform to be low. In previous work, for a multimode ridge waveguide fabricated with a similar method as the one described in the previous section, the propagation loss of 6.6 dB/mm was measured at 920 nm (Reithmaier et al. 2015).

To characterize the propagation loss on our platform, we fabricated on an undoped wafer a series of concentric waveguides with increasing length, as shown in Fig. 3.2(a). In this way, by measuring the transmission as a function of waveguide length, we can extract a propagation loss value per unit length. We design the waveguides such that the two grating couplers are equidistant, to ensure reliable alignment between each measurement. We then couple a continuum laser (SuperK) to one shallow-etched grating and record the collected signal at the output grating on a spectrometer. The optical setup used for performing this characterization is shown in Appendix A. We measure the transmission for all waveguides, as shown in Fig. 3.2(b). The three bending parts of the waveguides may add extra loss, but as the number is kept constant between each structure, propagation loss is the main effect on transmission. By extracting the maximum transmission T at the peak wavelength as a function of the waveguide length L, the propagation loss α_{PL} is extracted as the slope of $\log_{10}(T) = -\alpha_{\mathrm{PL}}L + T_0$, the intercept

T_0 representing the transmission limited by other loss sources. At a temperature of 10 K, a minimum propagation loss of 5.6 ± 0.4 dB/mm is extracted, comparable to a typical value of 7 dB/mm (Papon et al. 2019; Shadmani et al. 2022).

To identify the origin of this loss, we first investigate the effect of tether density. Tethers are needed to attach the suspended waveguides to the membrane. To minimize scattering loss, the single-mode waveguide is tapered to 650 nm to reduce mode overlap with the tether. We investigate the effect of tether density by varying the separating distance (5,10, and 20 μm) and repeat the propagation length measurement. The result is shown in Fig. 3.2(c), as the dark purple crosses. Within the errorbars, the measured propagation loss is compatible with the typical value of 7 dB/mm. The observed variation is not large enough to pinpoint the loss origin to the tethers.

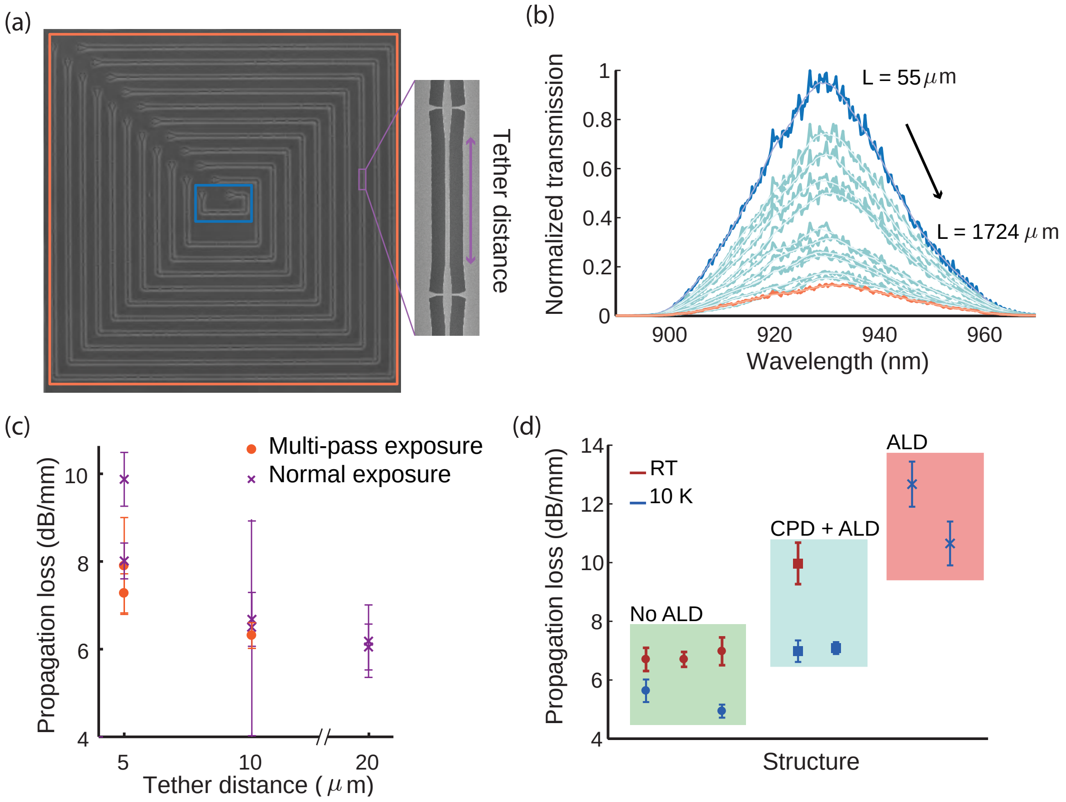

FIGURE 3.2: Propagation loss in undoped nanobeam waveguides. (a) SEM image of concentric waveguides to measure propagation loss as a function of waveguide length. (b) Measured transmission of a continuum laser light source across the waveguides. The dark blue curve corresponds to the shortest waveguide, and the red curve to the longest waveguide. (c) Measured propagation loss as a function of tether distance. We also compare the result from multi-pass exposure (orange circles) and normal exposure (single-pass, dark purple crosses). (d) For a tether distance of 15 μm, propagation loss is measured at room temperature (red data points) and 10 K (blue data points). We compare the process without passivation (green area), to processes with passivation (blue and red areas).

We attribute the loss to sidewall roughness, leading to scattering loss

(Parrain et al. 2015). The stochastic variation of the waveguide widths is characterized by a normal distribution with a width of $\approx 3.5 - 5$ nm, measured from SEM analysis. As a first hypothesis, we assume that the roughness comes from the e-beam lithography mask and is transferred to the waveguide after dry etching. To ensure smooth sidewalls of the resist mask, we performed e-beam lithography using the **multi-pass exposure** method (Pu et al. 2016). The dose needed to clear the patterns is $350\ \mu$C/cm^2, which leads to a dwell time of $0.056\ \mu$s for an exposure current of 1 nA, for a single-pass exposure (normal exposure). We, therefore, divide the dwell time by 4 and schedule the exposure of the waveguide patterns 4 times. We measure propagation loss for different tether distances, shown in Fig. 3.2(c) as orange data points. There is no striking improvement compared to the results with normal exposure, so another method is needed to smooth the sidewall of the resist. A promising method is the reflow of the electron-sensitive resist, which ensures the absence of cracks in the developed resist and hence smoothness of the transferred patterns (Benevides et al. 2020).

Work on the **surface treatment** of GaAs disk resonators demonstrated a significant quality-factor improvement (from mid-10^5 to 6×10^6) by diminishing surface absorption and scattering losses with the deposition of an alumina layer using atomic layer deposition (ALD) (Guha et al. 2017). We investigate this method. After the wet etching in HF, a sample is dipped in ammonia (6% NH_4OH, 30s) for surface preparation and loaded into an ALD chamber after drying. A layer of 5 nm alumina is then deposited at 150°C, this deposition temperature is chosen for higher film quality. Prior to ALD deposition, the native oxide is reduced by 5 pulses of trimethylaluminium at 300°C. The results of our tests, in terms of propagation loss, are shown in Fig. 3.2(d). The green area is the witness sample with no surface treatment. The samples that were dried by CPD show a better film quality (blue area) and hence lower propagation loss than the ones that were dried with a N_2 flow prior to ALD deposition (red area). This indicates that drying with CPD participates to the overall cleanliness of the sample surface. We notice, however, that the surface treatment with ALD has no impact on the propagation loss. In all cases, the loss is smaller at cryogenic temperatures due to the shift in the refractive index. In Ref. (Guha et al. 2017), the main improvement in propagation loss was attributed to the decrease of absorption loss, and the diminished scattering loss was more a side improvement. Given the poor results of the surface treatment, we conclude that the current main limitation of our platform is the sidewall roughness. Future tests will show improvements with the resist reflow technique. Wider waveguides can also be tested, which would decrease the overlap between the optical modes and the waveguide edges.

For completeness, we must highlight that these optimization trials were pursued on the undoped wafer. A recent study characterized the propagation loss in p-i-n membranes (Wang et al. 2021) and showed that electro-absorption is increased by pinning of the Fermi level due to surface defects. As a result, propagation loss as high as 20 dB/mm is measured due to the

Franz-Keldysh absorption, mainly caused by the p-layer. A proposed solution is to selectively etch the layer for light propagation after the emitter section. We can also investigate surface passivation to remove surface states, unpinning the Fermi level below the band gap (Kuruma et al. 2020).

3.2.2 Outcoupling efficiency with shallow-etched gratings

Once the photons are emitted and propagate on-chip with a loss characterized above, they must be outcoupled with a high efficiency. Different methods have been developed in the past years: some pursued lateral outcoupling by spot-size conversion of the waveguide mode to optical fibers (Daveau et al. 2017; Uğurlu et al. 2020), others exploited vertical diffraction to a microscope objective (Zhou et al. 2018). The latter presents the advantage of easy and reliable fabrication, as it only requires a single shallow-etching step. Moreover, it can be optimized for coupling efficiently TE-polarized modes exclusively. The method consists in periodically changing the refractive index according to the Bragg conditions by forming shallow-etched grooves, ensuring diffraction upwards. The small fraction diffracting downwards is reflected back by the GaAs substrate and the distance between the membrane is optimized to ensure constructive interference. Such a shallow-etched grating (SEG) provides coupling into an optical fiber with $> 60\%$ efficiency (Zhou et al. 2018) with low back-reflection into the structure.

The total percentage of the diffracted light is limited by the poor reflectivity of the GaAs substrate, which only reflects down-scattered light with a reflectivity of 0.31, given by the Fresnel equation at normal incidence. The SEG efficiency can be readily boosted by implementing a highly refractive surface instead of the GaAs substrate. This is done by epitaxially growing 15 layers of AlAs/GaAs ($79/66$ nm), forming a stack of distributed Bragg reflectors (DBR), as depicted in Fig. 3.3(a). Before fabrication of the SEGs, the reflectance of the chip is measured with a thin-film thickness measurement tool, as shown in Fig. 3.3(b) (green curve). This measurement shows a reflectance at room temperature (RT) of 95% for a wavelength range of 900-944 nm. We calculate the reflectivity with the transfer matrix method (TMM) at 10 K (blue curve) which indicates an expected shift in wavelength of around 14 nm compared to RT.

Structures with two SEGs connected by a waveguide of length $L_{\text{wg}} = 15\,\mu$m are fabricated, shown in the inset of Fig. 3.3(c). The sample is mounted into the chamber of a He-flow cryostat and cooled down to 10 K. The optical setup, depicted in Appendix A, has a beam expander in the input path to optimize the beam size for coupling into the SEG. The output path is equipped with a zoom fiber collimator for the same reason. The alignment to the nanobeam structure is optimized by maximizing the intensity collected at the output fiber and detected on a spectrometer while changing the angle and position of the excitation and collection paths. We use a continuously tunable laser for this experiment.

We first characterize the SEG efficiency in the same way as in Ref. (Zhou

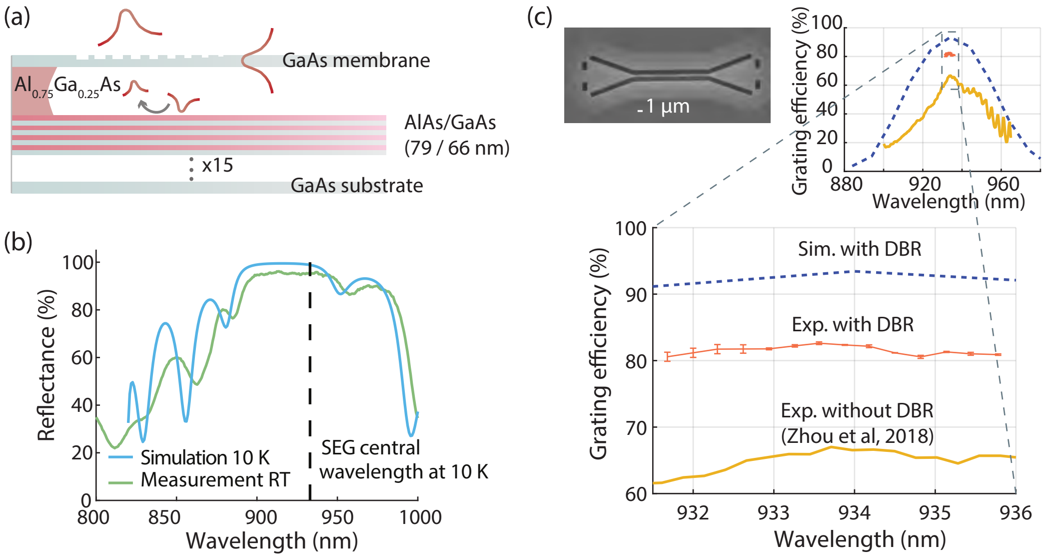

FIGURE 3.3: Boosted efficiency of the shallow-etched gratings. (a) Schematic of the working principle of shallow-etched gratings with boosted efficiency. The light traveling in the waveguide towards the grating is partly diffracted downwards. The distributed Bragg reflectors (DBR) reflect $> 95\%$ of the downwards diffracted light. (b) Reflectance measurement at room temperature (green curve) of a wafer containing DBR. Simulated reflectance spectrum at 10 K (the blue curve). (c) The grating efficiency is characterized by measuring the transmission across a nanobeam waveguide (inset). The result is shown around the central wavelength of the gratings (red data points). As a reference, we show the simulated efficiency (dashed line) and the grating efficiency without DBR from Ref. (Zhou et al. 2018) (yellow curve).

et al. 2018), where the intensity transmitted through the nanobeam waveguide is normalized by a reference measurement, in this case, the direct reflection on an unpatterned surface of the chip. Assuming that both gratings are identical and neglecting the loss in the short waveguide, we extract the grating efficiency in the following way

$$\eta_{\mathrm{SEG}} = \sqrt{\frac{P_{\mathrm{SEG}} \cdot R_{\mathrm{DBR}}}{P_{\mathrm{Ref}}}}, \tag{3.1}$$

with $R_{\mathrm{DBR}} = 95\,\%$ extracted from Fig. 3.3(b). This yields a maximal grating efficiency, averaged over three structures, of $\eta_{\mathrm{DBR}} = (85.1 \pm 0.1)\%$ at the peak wavelength transmission.

Another way of calculating the grating efficiency is by comparing the power P_{SEG} measured in the fiber after transmission through the SEG structure to the power at the input. The advantage of such a method is that the exact knowledge of the reflectivity of the bulk surface is not required. We calibrate the efficiency of the different optical elements of the setup, listed in Appendix A, to correctly account for all losses. We then calculate the grating transmission efficiency from the normalized peak values of the transmission through three different structures, with the mean values shown in

Fig. 3.3(c) (red data points). We obtain a maximal transmission efficiency of $\eta_{\text{SEG}} = (82.6 \pm 0.2)\%$ at 933.6 nm.

The simulated efficiency, overlapped with a perfectly symmetric Gaussian mode, lies above 90% (purple dashed line). The measured efficiency may be limited in practice by the imperfect mode matching and the ellipticity of the diffracted mode. This can be accounted for in future experiments by tailoring the SEG geometry to reduce the asymmetry or using beam circularizing optics. The numerical optimization of the DBR and the calculation of the outcoupling efficiency were performed by Dr. Xiaoyan Zhou.

To appreciate the improvement in outcoupling efficiency, we compare in Fig. 3.3(c) the results obtained on a wafer without DBR (Zhou et al. 2018) (yellow line) and the efficiency extracted in the present experiment. From this comparison, we conclude that the additional DBR boosts the SEG efficiency by at least $20\,\%$. This improved outcoupling method combined with an efficient single-photon source will help to generate a large photonic resource (Uppu et al. 2020b).

3.2.3 Metalization and wirebonding

When considering the yield and reproducibility of the fabrication process, it is necessary to evaluate not only the photonic part but also the electrical part, especially the reproducibility of the metalization on the ultra-thin heterostructure. The expected diode behavior should be proportional to the Shockley equation (Sze et al. 2007). Ideal IV-curve behavior shows suppressed current in reverse bias and turn on of the diode in forward bias, at bias larger than 1.5 V at cryogenic temperatures. In this way, the quantum dots can be operated at these voltages without current flowing. Deviation from this behavior is attributed to defects on the surface, which open vias from the p-layer to the n-layer, leading to short cut upon metal deposition.

Impressive progress has been made to avoid such defects by miniaturizing the area of the p-electrode and hence decreasing the probability of a shortcut between the p- and the n- layers (Wang 2021). Two examples of the high yield are shown in Fig. 3.4(a,b). We report IV curves measured at room temperature for two different samples, measured with a probe station after fabrication (plain curves). Successful diodes to our standards will show low leakage current in reverse bias, limited by the measurement noise of the sourcemeter. Moreover, the turn-on should not occur for voltage below 0.5 V at room temperature. With this criteria, we estimate a fabrication yield of 90%.

After fabrication, we need to interface the sample with the electrical equipment of the cryostat, which is done by wirebonding from the sample bonding pads to a printed circuit board (PCB). In this process, a metallic gold ball is welded on a bonding pad, with a thick gold layer, by use of heat, pressure, and ultrasonic energy. The wirebonding step can decrease the yield, as shown in Fig. 3.4(a) (dashed curves). In this case, we used a bonding force of 400 mN, which we chose to solve a problem of adhesion to the bonding pads. The high force applied on the bonding pad resulted in

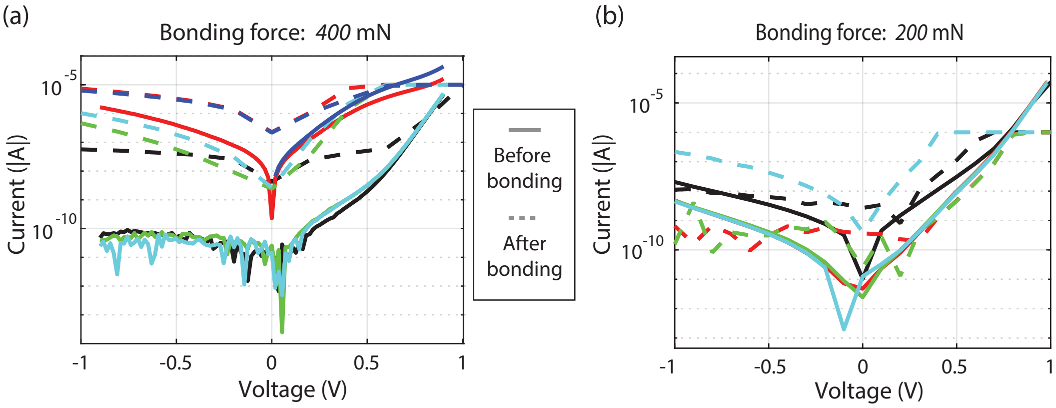

FIGURE 3.4: Comparison of the diodes' behavior before (plain curves) and after wire-bonding (dash curves) with a bonding force of (a)400 mN, (b) 200 mN.

punching through the p-layer and, thus, higher current flow.

We performed different bonding tests and identified that, given a thicker layer of gold on the p-pads (≈ 200 nm), a force as small as 50 mN is sufficient to bond on the pad. A more reliable force of $150 - 200mN$ is used for the chip bonding shown in Fig. 3.4(b), yielding a higher yield of successful IV curves.

We also conducted a test with polymer pillars deposited prior to the p-metal, with the idea that bonding on protected areas of the bonding pads would prevent damaging the p-layer. However, the adhesion of the metal-semiconductor interface turned out very poor. Another solution could be to deposit an oxide insulating layer, but again we might face an adhesion problem. Finally, we could test increasing the Cr adhesive layer underneath the Au layer of the p-metal, from 50 to 100 nm, to protect the surface.

In conclusion, the quantum photonic platform based on InAs quantum dots embedded in GaAs presents fabrication challenges that currently limit its efficiency. Throughout this thesis, we participated in the generic effort of efficiency optimization. While we could not solve all issues, we presented directions to move forward. Although propagation loss currently limits the size of the full integrated circuit that can reasonably be fabricated, this platform presents a number of salient features that are appealing for scaling up to more single-photon sources. In this direction, we will present and develop the necessary hardware to scale up to two single-photon sources.

3.3 Optimized design for simultaneous operation of two quantum dots

In this section, we introduce the necessary designs missing in the quantum photonic toolbox to build a device for simultaneously exciting two waveguide-based single-photon sources. First, a compact way to distribute the pump laser is needed. Using an on-chip tunable beamsplitter (Papon et al. 2019) can be a way forward, and cascading several beamsplitters could be used for exciting a larger number of single-photon sources. The challenge, however, is that the current fabrication of such devices necessitates a cleaning procedure with hydrogen peroxide and phosphoric acid to ensure the complete removal of resist residues. This cleaning step is incompatible with doped layers in gated samples (Wang 2021). Alternatively, we take inspiration from silicon photonics and adapt the design of polarization diversity gratings (PDG) to GaAs. With this device, optical power can be distributed to two orthogonal waveguides with a ratio controlled by the polarization of the input light (VanLaere et al. 2009).

Another necessary functionality is the individual tuning of quantum dots embedded in two waveguide-based single-photon sources. This is implemented with shallow-etching of isolation trenches on each waveguide. Finally, we consider the impact of quantum dot density on the probability of exciting two mutually resonant quantum dots.

3.3.1 Polarization diversity grating

In classical communication, the light coupling in the fiber may have two polarizations, not necessarily known in advance. Integrated circuits designed and fabricated in silicon possess, however, a strong polarization dependence because of the high refractive index. As a consequence, devices designed for a given polarization will be lossy for the other one. Polarization diversity gratings bring a solution since they can couple each polarization with close to equal efficiency to the TE modes of two identical waveguides using a two-dimensional diffraction grating (Roelkens et al. 2010). In quantum information, this device is also useful to convert on-chip path-encoded quantum information to the free-space polarization-encoded basis (Olislager et al. 2013; Wang et al. 2016).

In adapting the PDG to our platform, we follow the design presented in Ref. (VanLaere et al. 2009). In this work, the realization of a two-dimensional focusing grating, desired for the compactness of the design, is done by superimposing the ellipses of two orthogonal one-dimensional focusing gratings. In our case, we superimpose the ellipses of two orthogonal shallow-etched gratings (SEG) (Zhou et al. 2018) and define holes at the intersection. In the design presented in Ref. (Zhou et al. 2018), the width of the ellipses varies to apodize the diffracted light and ensure better overlap with a Gaussian mode. In our design of the PDG, we have a set with apodization, meaning with varying hole size, from 76 nm to 45 nm, and without apodization, applying a constant hole size of 76 nm. The PDGs are then fabricated during the same lithography and shallow-etching steps as for the SEG, and a detail of the PDG shallow-etched holes is shown in Fig. 3.5(a,bottom).

To characterize the transmission of the PDG, a simple test structure is defined, where each waveguide is terminated by SEG, as shown in Fig. 3.5(a,top). To account for the difference in the wavevector between the waveguide and the diffraction grating (Luo et al. 2018), we find experimentally the angle α between the waveguides that will maximize transmission. The PDG is designed for coupling a light field with an optical axis along the bisection of the PDG and tilted by $10\circ$ with respect to the normal. The last point is necessary to ensure the absence of back reflection from the second-order modes of the gratings (Zhou et al. 2018).

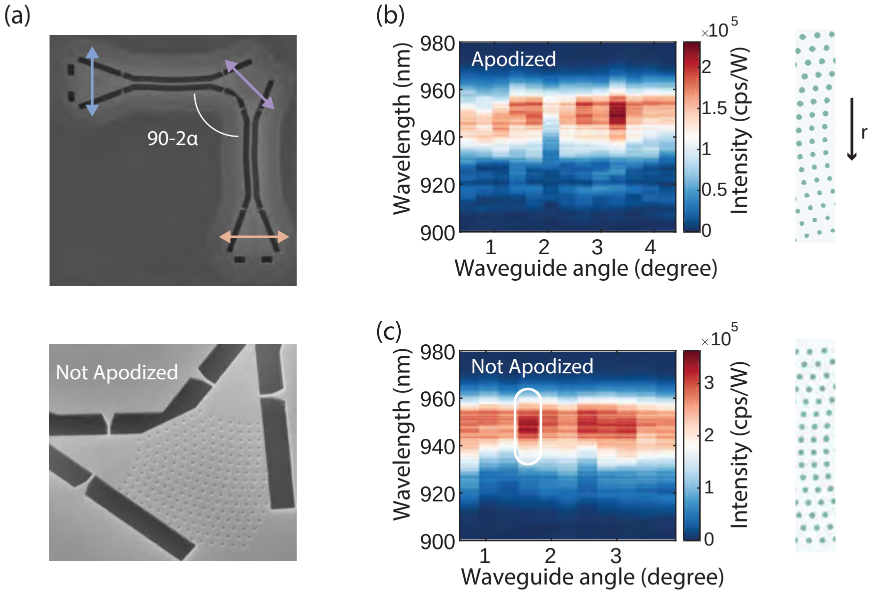

FIGURE 3.5: Design of polarization diversity gratings. (a) SEM image of the device to characterize the polarization diversity grating (PDG). The angle between the two nanobeams is varied. Bottom: zoom on the shallow-etched part of the PDG, not apodized. (b) Transmission measurement of a continuum laser source between an apodized PDG and the blue shallow-etched grating (SEG) port as a function of the waveguide angle. (c) A similar measurement is performed for the non-apodized PDG. The structure with the highest transmission is highlighted (white circle).

A supercontinuum laser light (SuperK, NKT Photonics, setup in Appendix A) is coupled to the PDG, with a polarization aligned as indicated by the purple arrow in Fig. 3.5(a,top). We optimized the alignment on a structure with an input SEG oriented along the same direction (45°). The intensity at the left SEG (blue arrow) is recorded on a spectrometer as a function of the input wavelength and the waveguide angle. We report the results for the apodized and non-apodized PDG in Figs. 3.5(b) and 3.5(c), respectively. As a general trend, the apodized PDGs are less efficient than the non-apodized PDGs, which is explained by the weaker diffraction efficiency of the non-apodized grating, as smaller features are etched shallower in the RIE process (RIE lag). From the transmission of the non-apodized grating, the waveguide angle presenting the highest transmission is marked (white area in Fig. 3.5(c)) and investigated further.

To characterize the extinction ratio between the two output ports of the structure (blue and red arrows in Fig. 3.5(a)), we record the transmission collected at each output as a function of the input polarization when the sample is cooled down to 10 K. The polarization is varied by rotating a half-wave plate (HWP) in the input path. The extinction ratio is defined as $\mathrm{ER} = 10\log_{10}(I_{\mathrm{red}}/I_{\mathrm{blue}})$. A clear broadband tuning of the coupling to each waveguide is seen in Fig. 3.6(a), with an extinction ratio larger than 20 dB in absolute value. This could be further improved by adding a quarter-wave plate before the HWP in the input port to linearize any residual polarization ellipticity.

Finally, we characterize the coupling efficiency to the PDG. In theory, the PDGs and the SEGs should have the same efficiency. We, therefore, compare the transmission through a horizontal nanobeam waveguide terminated with two SEGs (gray curve in Fig. 3.6(b)) to the transmission of the structure with a PDG. For this experiment, we optimized the input alignment for maximum coupling to the blue output port (purple curve in Fig. 3.6(b)). By comparing the transmission, we estimate the PDG coupling efficiency to reach maximally 25% of the SEG coupling efficiency at 950 nm. Recalling the value mentioned in section 3.2.2, this leads to a maximum PDG coupling efficiency of 20%, limited by mode overlap and etching depth of the shallow holes. Finally, we measured the crosstalk by recording the transmission from the blue port to the red port, shown by the yellow curve in Fig. 3.6(b). At a wavelength range close to the maximum transmission of the PDG, the crosstalk is suppressed by 3 orders of magnitude.

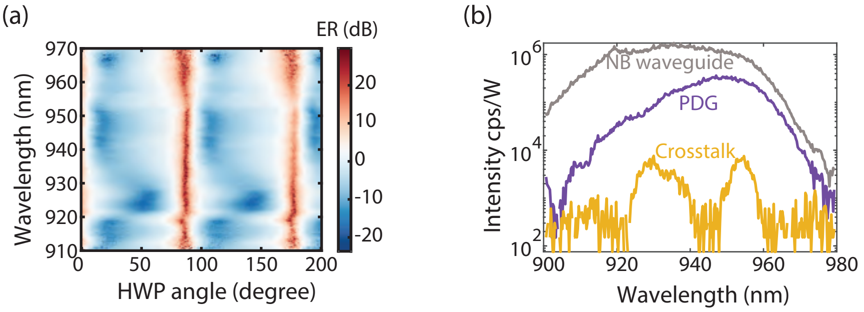

FIGURE 3.6: Performance of the polarization diversity grating. (a) Extinction ratio between the blue and red SEG ports (defined in Fig. 3.5(a)) as a function of the polarization of the input light, controlled by the half-wave plate (HWP) angle. (b) The transmission across a single nanobeam waveguide with two SEGs is shown as the gray curve to compare to the transmission across the structure with the most efficient PDG (purple curve). The crosstalk is measured by exciting at the red port and collecting at the blue port (yellow curve).

In conclusion, we have designed a compact device to control the distribution of optical power into two different waveguides by adjusting the polarization of the input light. This is a key functionality to operate two single-photon sources simultaneously in a controlled fashion.

3.3.2 Electrical isolation with trenches

A p-i-n junction embedded in the wafer membrane allows applying an electric field across the entire area of the sample after fabricating metal pads. However, it may be advantageous to restrict the electrically active areas, which can be done via lithographic methods and metalization. In general, the back n-layer is used as a plane for common ground, and individual p-areas are defined by shallow-etches trenches, etched approximately 50 nm to remove the p-layer.

Shallow-etched trenches were used in previous work to reduce the RC constant of local p-i-n diodes (Pedersen et al. 2020), a demonstration of good electrical isolation. A small electrically active area can be defined by patterning and depositing metals in the vicinity of a nanophotonic structure, as shown in Fig. 3.7(a), where the metal contacted to the p-layer is shadowed in yellow. The contact is then surrounded by a shallow-etched trench, highlighted in light blue. A tapered shallow-etched trench is fabricated on the nanobeam waveguide, as shown in the inset of Fig. 3.7(a), to restrict the active electrical to the central waveguide part. The trench width is adiabatically tapered to avoid scattering at the trench position and ensures a high simulated transmission of $\approx 99\%$ [2]. The trenches are etched together with shallow-etched gratings. We do not provide a measured transmission efficiency of the trenches, however, we observed the presence of scattering on the camera of our imaging system when light propagates through the nanobeam waveguide with trenches, indicating a lower efficiency than simulated.

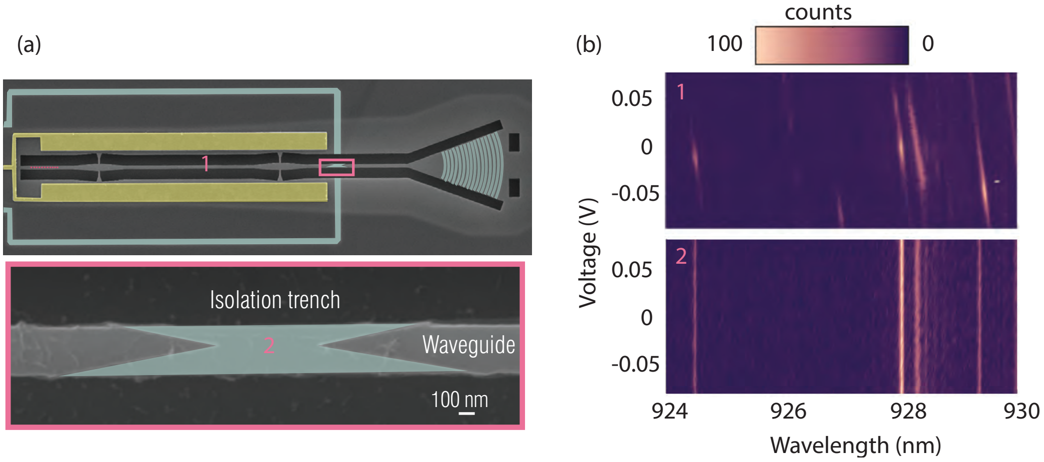

FIGURE 3.7: Electrical trenches for isolated DC-Stark tuning. (a) SEM of a single-sided nanobeam waveguide, where the p-electrode is highlighted in yellow. The shallow-etched trenches are located in the blue shadow. The inset shows a zoom of the tapered shallow-etched trench on the waveguide. (b) Above-band excitation as a function of applied voltage at two locations on the sample. In the electrically active part of the waveguide (1,top), the different excitonic lines tune as the voltage is swept. On the contrary, at the position of the trench (2, bottom), no DC-Stark tuning is observed.

A simple measurement to test the isolation provided by this shallow trench is to record the DC-Stark tuning effect, introduced in Chapter 1, on quantum dots located in the active optical area compared to quantum dots located in the electrically isolated part. We show the fluorescence from

---

[2] simulation courtesy of Assoc. Prof. Leonardo Midolo

quantum dots recorded on a spectrometer in Fig. 3.7(b,top), when a quasi-resonant laser is positioned in the nanobeam waveguide (position "1"). In this case, the emission frequency tunes clearly with the applied voltage bias. When the laser is moved to the trench, in Fig. 3.7(b,bottom), some excitonic transitions are shown, but the frequency tuning is absent: as the p-layer is removed, the quantum dots are not subjected to a large built-in field and the DC-Stark shift. With this result, we prove that shallow-etched trenches provide sufficient electrical isolation between different parts of the waveguides.

This small addition to nanophotonic devices enables the design of structures where two electrical and optical active regions can be biased independently by applying individual voltages to different p-electrodes.

3.3.3 Quantum dot density

To fabricate a successful single-photon source, we rely on the high fabrication yield and an adapted quantum dot density to overcome the random localization of self-assembled quantum dots.

If the density is too low, the probability of exciting a quantum dot at optimal position and wavelength for strong light-matter interaction will also be low. In this case, localization of quantum dots prior to fabrication is necessary (Chu et al. 2020). This pre-localization method can be circumvented with a higher quantum dot density, controlled by the growth condition (Bart et al. 2022). Too high quantum dot density will, on the other hand, ruin the single-photon source purity since the pure emission of a single quantum dot will be undermined by emission from neighboring quantum. With a moderate density of 10 QDs/μm^2, it is possible to measure several quantum dots coupled to the nanophotonic structures with high coupling efficiency (β-factor) (Pedersen et al. 2020).

We evaluate the success probability of finding a pair of quantum dots (QD) emitting at the same wavelength. To compensate the inhomogeneous broadening of self-assembled quantum dots, the DC-Stark tuning can be used, with a tuning range limited by the wafer heterostructure. Assuming two Gaussian distributions of wavelengths, centered at 930 nm and with a standard deviation of 15 nm, the probability of finding two quantum dots emitting at the same wavelength within a tuning range $\delta\lambda$ is expressed as

$$P(0 \leq \lambda \leq \delta\lambda) = \int_0^{\delta\lambda} \frac{1}{\sigma}\sqrt{\frac{2}{\pi}} e^{\frac{-\lambda^2}{2\sigma^2}} d\lambda. \tag{3.2}$$

The quantum dots described by the two Gaussian distributions are each embedded in a device of area A and are distributed according to a density ρ_{QD}. In this case, the total number of possible quantum dot pairs is $(A \cdot \rho_{\mathrm{QD}})^2$. Finally, the number of quantum dot pairs within $\delta\lambda$ is calculated as $P(0 \leq \lambda \leq \delta\lambda) \cdot (A \cdot \rho_{\mathrm{QD}})^2$. The result is given in Fig. 3.8, for different tuning range $\delta\lambda$ and QD density ρ_{QD}. We consider a waveguide with a width of 200 nm, which corresponds to the region where quantum dots can be excited within the waveguide-based single-photon source presented in Chapter 2, section

2.3. The length is chosen to be 40 μm, to increase the success probability. Moreover, we added a 50% penalty on the number of mutually resonant QD pairs to account for the cavity effect. This effect originates from reflections between the photonic crystal filter/mirror and the shallow-etched gratings, which presents a finite reflection (Zhou et al. 2018).

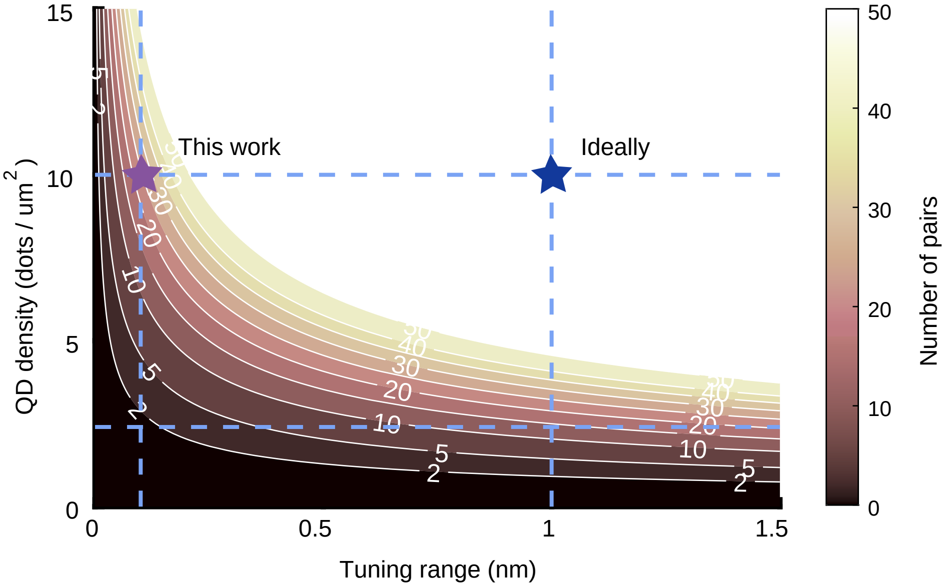

FIGURE 3.8: Calculation of the expected number of quantum dots pairs that can be tuned in mutual resonance as a function of the quantum dot density and the tuning range. We assume a waveguide with a width 200 nm and a length 40 μm. The quantum dots wavelength follow a normal distribution with a standard deviation of 15 nm.

In this work, with a tuning range of 0.1 nm and a QD density of 10 μm^{-2} (Uppu et al. 2020b), we expect to find approximately 25 pairs, given the length of the QD region of 40 μm. We deem this result encouraging and, therefore, design waveguide-based single-photon sources with a 40 μm-long emitter section. We note that ideally larger wavelength tuning range, up to 1 nm, would increase the number of resonant QD pairs considerably. This is achievable with modified wafer heterostructures (Kiršanskė et al. 2017).

* * *

In conclusion, we have introduced the main nanofabrication methods to fabricate high-quality nanophotonic structures with electrically active layers. Main attempts towards the efficiency optimization of the present quantum photonic platforms were explained. Although propagation loss remains a challenge, we introduced successful outcoupling optimization, which contributes to the higher efficiency of the platform. Moreover, we demonstrated tailored designs for the integration of two waveguide-based single-photon sources by developing polarization diversity grating and implementing shallow-etched trenches for isolated tuning. We also investigated the probability of resonantly exciting a pair of quantum dots, given the available quantum dot density and wavelength tuning.

We assemble the aforementioned building blocks in a circuit performing the simultaneous resonant excitation of quantum dots embedded in two waveguide-based single-photon sources, shown in Fig. 3.9.

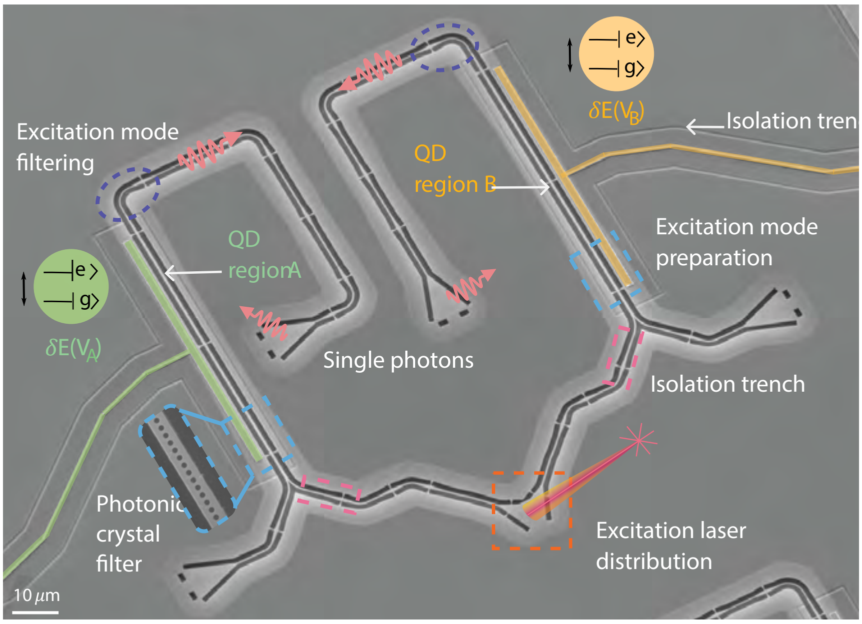

FIGURE 3.9: SEM of the fabricated device for circuit-based resonant excitation of multiple quantum dots. A PDG (orange dashed area) is connected to two waveguide-based single-photon sources, allowing the distribution of a pump laser. Two individual electrodes are fabricated close to each waveguide to independently tune quantum dots in region A (green shadow) and region B (orange shadow), ensured by isolation trenches on the waveguides (pink dashed area) and all around the electrodes. Single photons are collected through orthogonally-polarized SEGs after laser filtering by the waveguide taper and bending (purple dashed area). The photonic crystal filter is shown in the inset of the blue dashed area.

The polarization diversity grating distributes a pump laser to two quantum dot regions. Individual tuning of each region, denoted as A and B, is achieved by fabricating isolated local electrodes, highlighted in green and orange, respectively. Shallow-etched trenches are patterned around the electrodes and on top of the waveguide in the dashed pink region before the QD region. The emitter section is 40 μm-long, and a tether is added at the center to avoid the collapse of the structure after wet etching. The photonic crystal filter is located in the blue dashed regions before the emitter section of each waveguide. Shallow-etched gratings are added at the outputs to collect single photons off-chip after filtering through the taper and bent waveguide (purple dashed area). In the next chapter, we will investigate the performance of this small-scale multi-QD source.

4 Independent operation of two waveguide-integrated single-photon sources

This chapter is partly based on the following article (under peer-review)

C. Papon, Y. Wang, R. Uppu, S. Scholz, A. D. Wieck, A. Ludwig, P. Lodahl, & L. Midolo, **“Independent operation of two waveguide-integrated single-photon sources”** arXiv:2210.09826 (2022)

The quantum photonic toolbox presented in Chapters 2 and 3 opens a path towards addressing multiple single-photon sources via photonic circuits. In the present chapter, we will characterize the device performing the independent operation of two waveguide-integrated single-photon sources, presented in Fig. 3.9. To do so, we will perform resonance fluorescence experiments on a pair of resonant quantum dots, measure the second-order correlation functions and finally demonstrate two-photon quantum interference for the resonant quantum dot pair.

The goal is not only to achieve two-photon interference from remote emitters but also to demonstrate and operate a scalable multi-QD photonic circuit, which, to the best of our knowledge, has not been achieved so far. Our main focus is, therefore, to show that single-photon sources *and* the necessary control knobs to operate them are both scalable. We base, however, our understanding of two-photon quantum interference between remote emitters based on previous works. Such an experiment was performed on various platforms, notably quantum dots, molecules, and trapped ions, under quasi-resonant continuous wave-excitation (Patel et al. 2010; Lettow et al. 2010), resonant cw-excitation (Gerber et al. 2009), quasi-resonant pulsed excitation (Flagg et al. 2010; Reindl et al. 2017; Duquennoy et al. 2022) and resonant pulsed excitation (Weber et al. 2019; Zhai et al. 2022).

4.1 Optical setup for resonant excitation

To perform the experiment, the sample is inserted in a closed-cycle cryostat (attoDry2100) after wirebonding on a PCB and cooled down to 1.6 K, a temperature ensuring that decoherence from phonon dephasing is decreased (Tighineanu et al. 2018). Moreover, the low vibration of this system, equipped with a decoupled pulse tube, ensures the stability of the excitation and collection paths. In the following, we will describe the main characteristic of the efficient optical setup and introduce a dedicated HOM setup to interfere two different quantum dots.

4.1.1 Excitation and collection from a closed-cycle cryostat

The sample is fixed on top of a stack of three-axis nanopositioners (Attocube ANPx51), mounted at the bottom of a dipstick inserted in the cryostat, as described in Fig. 4.1. Helium buffer gas ensures a homogeneous thermal contact with the 1.6 K stage. Electrical feedthroughs connect the sample PCB to a multi-channel ultra low-noise voltage source (Basel Instrument, $1\ \mu$V root-mean-square (RMS) voltage noise). The nanopositioners are used to position the devices under a high-transmission cold objective (Numerical aperture 0.81, efficiency 82% (Pedersen 2020)), with a focal distance of $f = 2.39$ mm. Due to the length of the optical access, a $4f$-system is used as an optical relay to minimize diffraction losses. The optical excitation and collection paths are controlled via optical components mounted on a breadboard on top of the cryostat. The optical access to the dipstick is ensured by a thick top window, tilted to avoid direct reflections.

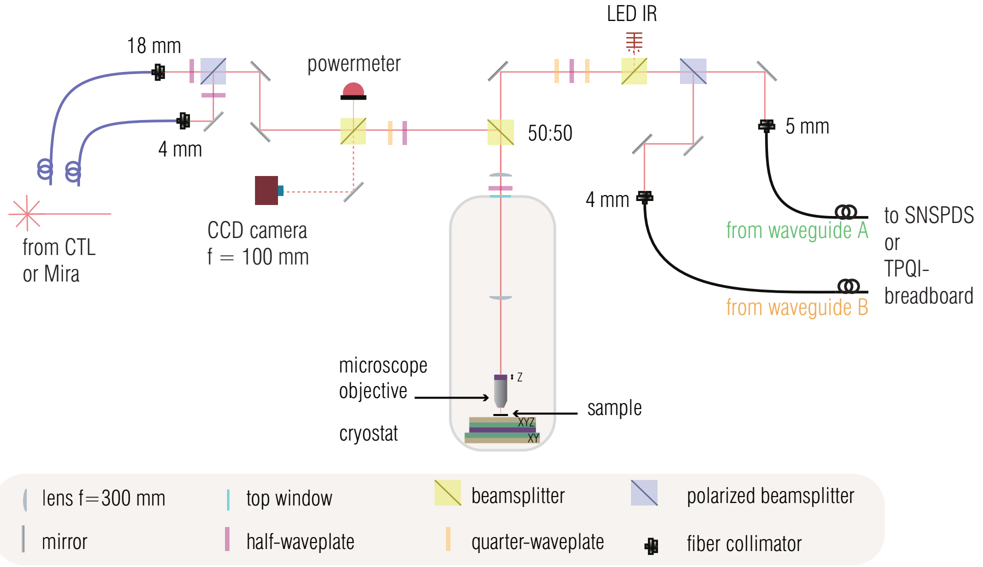

FIGURE 4.1: Optical setup for performing resonance fluorescence on a sample cooled down to 1.6 K in a closed-cycle cryostat. Laser light with stabilized optical power is sent to the sample via the reflection port of the $50:50$ beamsplitter and a microscope objective. The collected signal from the sample is then coupled to single-mode fibers after the transmission port of the $50:50$ beamsplitter. The current setup accommodates a single input path and two independent output paths.

The lasers used for excitation are transmitted to the breadboard via polarization-maintaining fibers. The lasers are then coupled to the setup via two fiber collimators, one with a lens of $f = 18$ mm, yielding diffraction limited beam spot size on the sample surface, which is used for top excitation. The other fiber collimator, with a lens of $f = 4$ mm, ensures a larger beam spot size, ideal for coupling into the shallow-etched gratings. This is the excitation port we will use for the experiment in the present chapter. The laser power in the breadboard setup is measured at the reflection output of a 50:50 beamsplitter (BS) to lock the power with a feedback loop. Afterward, polarization control is ensured with a pair of half- ($\lambda/2$) and quarter-waveplates ($\lambda/4$) mounted on motorized stages. The laser light is then sent to the sample via the reflective output of a 50:50 BS. Light is collected back from the sample through the transmission port of the same BS, followed by a dielectric mirror. We choose the 50:50 BS rather than a 10:90 BS to avoid strong birefringence during the alignment to the differently oriented grating couplers of the device.

The collected signal from the sample goes through a set of three waveplates ($\lambda/4$-$\lambda/2$-$\lambda/4$) to ensure full polarization control. The optical path is then split on a polarized beam splitter (PBS) and reaches two fiber collimators. The setup enables full position control for each output collimator, such that it is possible to couple signals from two different spots on the sample into two single-mode fibers. Two Schäfter & Kirchhoff assemblies are used for these outputs, one with $f = 4$ mm (60FC-4-A4-02) and one with $f = 5$ mm (60FC-SF-4-M5-10).

Throughout this experiment, we mainly used a continuously tunable laser (CTL, Toptica 950) for continuous-wave (cw) measurement with a narrow-bandwidth laser ($<$ 10 kHz from specs). Before sending it to the cryostat breadboard, a small fraction of CTL light is sent to a wavemeter (HighFinesse) to lock the frequency through a feedback loop. This allows scanning the frequency of the CTL down to 50 MHz incremental steps. For the pulsed experiment, a Coherent Mira laser is used, producing $3 - 5$ ps pulses of around 100 GHz bandwidth at a repetition rate of 72 MHz. The pulse bandwidth can be modified through a pulse stretcher, yielding pulses of 20-30 GHz bandwidth (Pedersen 2020).

The setup we refer to has been developed throughout the years to ensure efficient outcoupling of single photons with minimal equipment-induced noise (Uppu et al. 2020b; Uppu et al. 2020a; Pedersen 2020). Additionally, a setup for narrow filtering of the single-photon signal is necessary to reject the phonon sideband emission and to ensure high measured indistinguishability in pulsed excitation. To measure two-photon quantum interference, a setup for performing HOM experiment is needed. One was previously built to measure interference between two single photons emitted from the same quantum dot, necessitating a fiber delay. However, for performing the HOM experiment with two quantum dots, we need a setup to filter the signal from two quantum dots and a setup for performing two-photon interference.

4.1.2 Two-photon interference setup

We combine the two functionalities on the same breadboard, performing filtering and HOM experiment. To do so, the single photons emitted from two quantum dots, named QD$_A$ and QD$_B$, are coupled in two single-mode fibers at the output of the cryostat setup, which are then connected to the external setup shown in Fig. 4.2(a). With a set of $\lambda/2$-$\lambda/4$ waveplates on each path, we use a PBS to combine the signal from the two quantum dots in the same spatial mode but orthogonal polarization modes. The advantage is that the two modes can be filtered through a single etalon filter since this element is not birefringent. We show the transmission spectrum of the etalon in Fig. 4.2(b), which reveals a Lorentzian full-width half-maximum of $\Delta_{\text{FWHM}} = 3$ GHz and a free-spectral range of 98.6 GHz. The etalon is mounted on a Peltier element to control the central transmission frequency by warming or cooling the etalon, with a temperature tuning of 1.8 GHz/K. To avoid the parasitic temperature effect, we enclose the etalon in a plastic case with two anti-reflection coated windows. The etalon itself has a transmission efficiency of 95.6%.

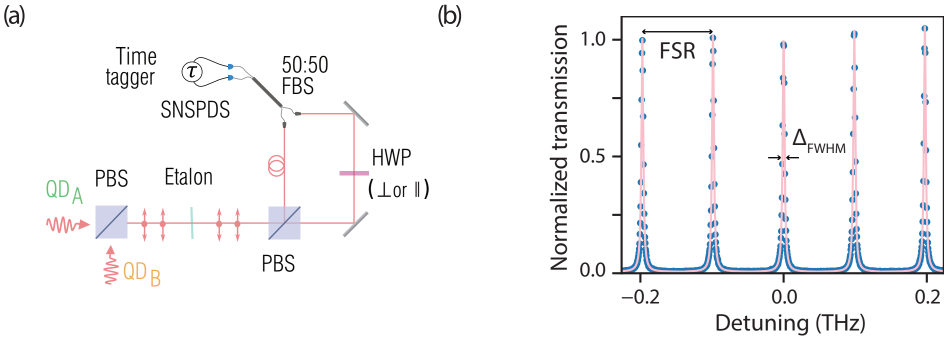

FIGURE 4.2: Setup for two-photon quantum interference between two quantum dots. (a) Schematic of the interferometer for two-photon quantum interference measurements. Single photons from QD$_A$ and QD$_B$ are filtered through an etalon and interfered on a 50:50 fiber beam-splitter (FBS). By rotating the half-wave plate (HWP), the coincidence counts are recorded with superconducting nanowire single-photon detectors (SNSPDs) for different polarization of the photons. (b) Transmission spectrum of the etalon filter, with a free spectral range (FSR) of 98.6 GHz and a full-width half-maximum (Δ_{FWHM}) of 3 GHz, extracted from a fit to Lorentzian functions. The transmission efficiency is 95.6%.

After the filtering part, the optical path is separated on a second PBS into the two arms of an unbalanced Mach-Zender interferometer (MZI). The delay in one of the arms is set such that the optical path length of the photons emitted from two quantum dots is the same. This is especially important in pulsed excitation, as the emission is triggered. The photons then recombine and interfere in the appropriate conditions on a $50:50$ fiber beam splitter (FBS) with measured transmission and reflection coefficients of 0.46 and 0.54, respectively. The outputs of the FBS are connected to superconducting nanowire single-photon detectors (SNSPDs, 96 ps time jitter, $\approx 70\%$ efficiency). A time-tagger (Swabian, 34 ps RMS jitter from specs) registers the time of each detection event. In one arm of the interferometer, a $\lambda/2$-waveplate is used to change the polarization between the two arms, either to a co-polarized or cross-polarized configuration. The latter configuration is used to normalize the two-photon quantum interference. We measure the cross-talk between the horizontally polarized optic path and the vertically polarized one is $< 1\%$. The total transmission efficiency from the input fiber of the breadboard to the detector fiber is $\approx 50\%$ when the polarization before entering the MZI is optimized. All fiber collimators are built with lenses with $f = 11$ mm to ensure a beam diameter of ≈ 2 mm throughout the setup. Coupling efficiency to the fiber collimators at the output is 75-85%. The polarization of the interferometer is aligned by scanning the CTL frequency (10 pm scan steps) and minimizing the classical interference fringes with a three-paddle polarization control at one input fiber of the FBS when the HWP is set to yield cross-polarized fields. The classical visibility of the MZI is then measured to $> 99\%$ when the HWP is set to yield co-polarized fields.

4.2 Initial characterization

In the following, we introduce the different characterization steps to isolate a working device on a nanophotonic chip. Indeed, the device shown in Fig. 3.9 is one of 25 fabricated devices, which contain copies of the photonic crystal filter with different hole radii, ranging from 70 to 74 nm. The radii are chosen from a parameter space encompassing the previously realized device (Uppu et al. 2020a). The devices are fabricated in series, meaning that a common p-electrode is distributed to the waveguides A of each structure, and a second p-electrode is connected to the waveguides B, as indicated in Fig. 4.3(a,top). Regarding the IV-curves, at 1.6 K, the current flowing across the p-i-n on sides A and B is 5 μA and $1 \times 10^{-4}\mu$A at 1.25 V, respectively. The resistance between the two p-electrodes is 55 MΩ, a result of the electrical isolation provided by the shallow-etched trenches.

Firstly, we want to find the device that leads to the best laser suppression. For this, we measure the transmission spectrum through the device by scanning the CTL wavelength with a step of 0.05 nm. The CTL is first coupled into the shallow-etched gratings (SEG) of waveguide A and then to the SEG of waveguide B, as depicted in Fig. 4.3(a,top). The device transmission, T_{dev}, is normalized by a reference transmission, T_{ref}, measured through a structure without a mode filter. We perform this measurement on all devices, and we show in Fig. 4.3(a,bottom) the result for the device with the best laser suppression. We identify a wavelength region, highlighted in gray, where both sides of the structure present laser suppression $< 10^{-2}$. This value, by recalling the device's working principle introduced in section 2.3, indicates the filtering of the TE0 mode by the photonic crystal filter. These measurements were performed with 0 V applied bias on each side. Beyond the overlapping part of the spectrum, the wavelength response is quite different on both sides. This is the effect of residual random fluctuations in the fabrication process.

Secondly, we move on to find potential quantum dot pairs on this device, excited on resonance. The CTL is coupled to the SEG, and the voltage across the diode is set to 1.25 V, as indicated in Fig. 4.3(b,top). This voltage corresponds to the bias at which neutral excitons can be excited. The emitted photons are detected at the output SEG while scanning the CTL

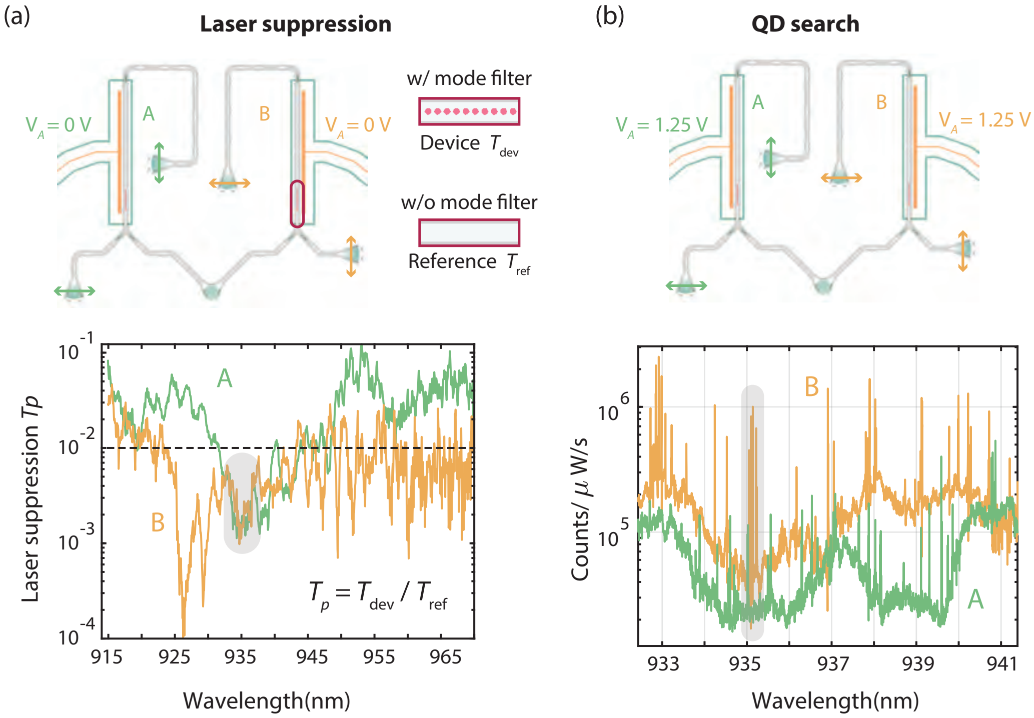

FIGURE 4.3: Laser suppression and quantum dot search. (a) The transmission through the device with a mode filter T_{dev} is normalized by the transmission through the device without a mode filter T_{ref}, for waveguide A (green curve) and waveguide B (orange curve). The gray area shows the wavelength region with overlapping laser suppression. (b) For the initial quantum dot search, we perform a finer wavelength scan with the voltage set at 1.25 V on each waveguide. We measure the resonance fluorescence from multiple QDs. The overlapping wavelength range showing low laser background and high counts from the QD emission is shown in gray.

wavelength with a fine step of 0.002 nm. The quantum dot search is first performed on waveguide A, then on waveguide B. We report the result in Fig. 4.3(b,bottom), which shows a large number of quantum dot lines. We highlight the wavelength region where the background is lowest for both sides A and B, and the quantum dot lines are the brightest. The power used for this measurement was 2.5 μW with neutral density filter (OD) 5.0.

For this characterization technique, the CTL wavelength scan is synchronized with the timetagger. Counts are detected continuously and binned to achieve the desired wavelength resolution. By doing so, wavelength scans can be acquired in a fast way; for example, the fine scan of Fig. 4.3(b) lasted for 20 min. Therefore, we can investigate all the devices and pick the best one. However, to perform more accurate quantum dot spectroscopy, we move on to locked frequency and voltage scans.

4.3 Resonant spectroscopy on multiple quantum dots

The introduction of the results of resonance fluorescence in Chapter 1 contains the necessary tools to investigate the properties of different quantum dots. We will utilize them to characterize the linewidth and saturation behavior of two quantum dots.

4.3.1 Charge Plateau

From the preliminary characterization, we isolate the resonant frequencies of potential quantum dot pairs. We then perform resonance fluorescence (RF) scans on each side of the structure by subsequently scanning the locked frequency in steps of 1 GHz. At each frequency, the voltage in waveguide A or B is scanned with incremental steps of 0.5 mV. The CTL power sent to each SEG is 1 μW with OD 5.0 to stay below saturation of the quantum dot transitions. The measurement performed on waveguide A (B) is shown in Fig. 4.4(a) (Fig. 4.4(b)). The frequency-voltage maps are corrected from background counts for clarity.

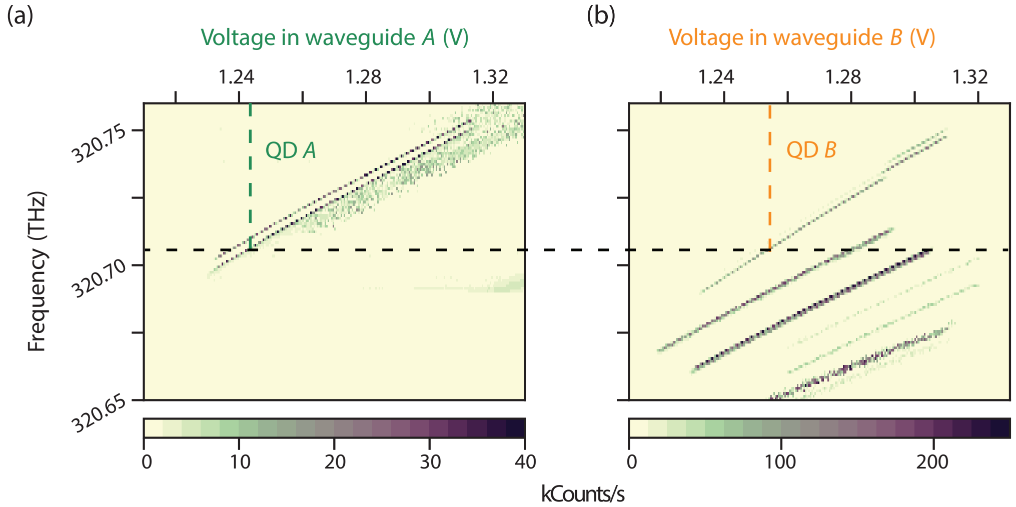

FIGURE 4.4: Resonance fluorescence collected from waveguide regions A (a) and B (b), as a function of the CTL frequency and bias voltage applied on each waveguide. If the laser frequency is locked to 320.705 THz (black dashed line), two quantum dots QD_A and QD_B located in each waveguide can be excited in resonance by setting each voltage to 1.243 V and 1.253 V, indicated respectively by the green and orange dashed curves.

We distinguish clear charge-tunable excitonic lines in the Coulomb blockade regime. We identify the charge states to be the neutral exciton, given the voltage range of these plateaus (Uppu et al. 2020b). Moreover, for the RF measurement in waveguide A, we notice two lines tuning parallelly and showing the same charge plateau length, which are assigned to the two dipoles of a single quantum dot. The 3.5 GHz frequency spacing fits with the fine structure splitting Δ_{FSS} that has been measured on this wafer previously (Uppu et al. 2020b). We identify the brightest of the two dipoles as QD_A in Fig. 4.4(a). A similar second dipole can be seen next to the line indicating QD_B in Fig. 4.4(b) but with a much weaker transition. The different relative intensities can be explained by the lateral position of each dot in the waveguide, leading to the different coupling to excitation and collection modes, as shown in Chapter 2.

From the charge plateau, a lever arm effect is extracted for each quantum dot and is used to relate resonant transition frequency to the voltage at resonance. From a linear fit, we extract the tuning slope of 0.67 GHz/mV for QD_A and 0.76 GHz/mV for QD_B. From this point on, we perform RF scans by sweeping the voltage applied for a fixed laser frequency, which makes the measurement faster. By locking the laser frequency to 320.705 THz, marked by the black dashed line in Fig. 4.4, two quantum dots are brought in resonance by setting V_A and V_B, the voltages across waveguide A and B, independently. Here we chose the upper excitonic line of waveguide B, but two other quantum dots can also be brought in mutual resonance with QD_A.

4.3.2 Simultaneous resonant excitation

All we are left to do is to excite the quantum dot pair simultaneously with the CTL coupled to the polarization diversity grating (PDG), as shown in Fig. 4.5(a). We align the input laser by using a reference structure (without a mode filter) and ensure equal coupling to the waveguides by adjusting the positions and polarization. This will be further adjusted to provide similar optical power at each quantum dot.

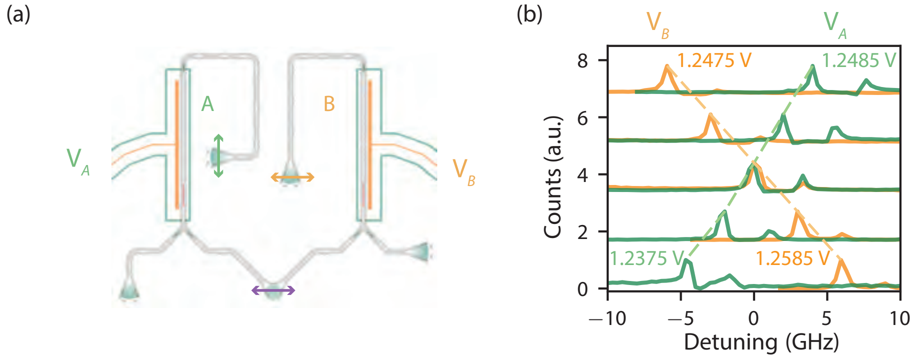

FIGURE 4.5: Simultaneous resonant excitation of a quantum dot pair. (a) Sketch of the experiment. The CTL is coupled to the PDG (purple arrow), and single photons are collected from the two output ports (green and orange arrows). (b) The laser frequency is fixed to 320.705 THz, and the two quantum dots are brought into resonance by sweeping independently V_A and V_B.

The frequency of the CTL is locked at 320.705 THz, and the voltage across each waveguide is changed independently to tune each quantum dot, as shown in Fig. 4.5(b). By fixing the voltage across the diode of the waveguides A and B to $V_A = 1.243$ V and $V_B = 1.253$ V, respectively, the mutual resonance between the two quantum dots is ensured. For clarity, each data set in Fig. 4.5(b) is normalized to its peak value.

We note that in between the initial characterization of the device and the final demonstration of simultaneous resonant excitation of a quantum dot pair, the cryostat underwent a couple of cycles of warm up and cool down. This resulted in a global shift of resonance frequency by approximately 10 GHz, but the quantum dots' linewidth was unchanged.

4.3.3 Saturation of the resonance fluorescence

As introduced in section 1.3, a two-level system reaches saturation as the Rabi frequency Ω is increased. This is controlled by increasing the power of the driving field since $\Omega^2 \propto P$. The saturation of the two quantum dot transitions is shown in Fig. 4.6(a). It is measured by recording the peak intensity as a function of the power sent to the sample, corrected for the OD filter transmission. We fit the saturation curve for QD$_A$ (green stars) and QD$_B$ (orange stars) with

$$I(P) = I_\infty \frac{1}{1 + P_{\text{sat}}/P}, \tag{4.1}$$

where I_∞ is the maximal intensity of the transmission and P_{sat} the saturation power at which the $I(P_{sat}) = I_\infty/2$. The fit yields a saturation power of $P_{sat} = 4.5 \pm 0.2\ \mu$W for QD$_A$ (green dashed curve) and $P_{sat} = 8.7 \pm 0.3\ \mu$W for QD$_B$ (orange dashed curve). Although the saturation powers are not fully equalized, the PDG ensures that the power coupled to each waveguide is of the same order. More importantly, the Rabi frequency of each QD transition should be similar to guarantee comparable dynamics.

By comparing Eq. 4.1 to the saturation of a two-level system derived in Eq. 1.5, the Rabi frequency, in the absence of dephasing, is defined as

$$\Omega(P) = \frac{\gamma}{\sqrt{2}} \sqrt{\frac{P}{P_{\text{sat}}}}, \tag{4.2}$$

with γ being the radiative decay. Knowing the latter for each QD, a measurement shown in the next section, we use this simple relation to translate the bottom axis in Fig. 4.6(b), which shows the full-width half-maximum Δ_{FWHM} of the excitation spectra of each QD as a function of the increasing Rabi frequency. Both the Rabi frequency and Δ_{FWHM} are shown in unit of $\Gamma = \frac{\gamma}{2\pi}$, for each QD. In the low-power regime, the linewidths are broadened by $1.2\Gamma_A$ ($2.6\Gamma_B$) for QD$_A$ (QD$_B$), showing narrow-linewidth operation. Recalling the derivation from 1, we fit the data for each QD with

$$\Delta_{\text{FWHM}} = \sqrt{\Gamma^2 + 2\Omega^2} + b, \tag{4.3}$$

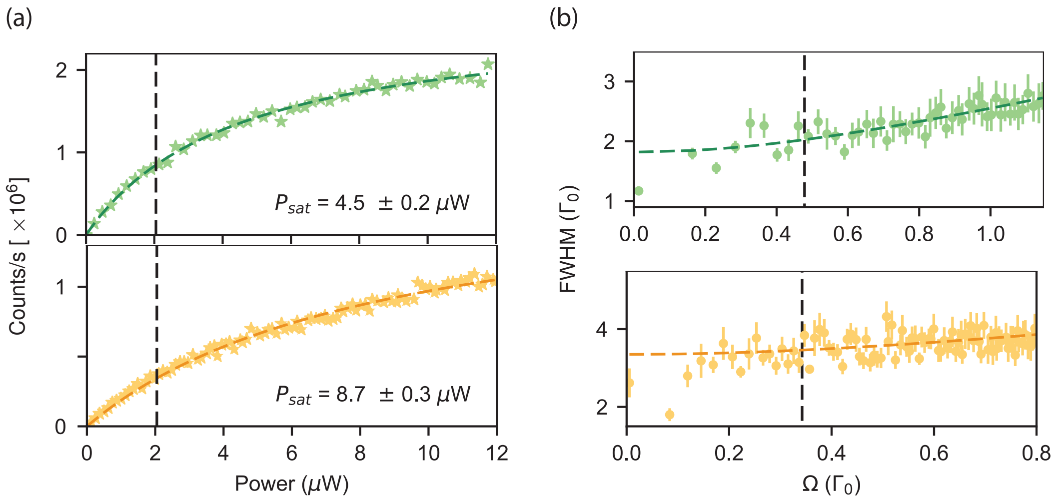

FIGURE 4.6: Saturation and power broadening of two excitonic transitions. (a) The peak intensity is measured as a function of excitation power for QD_A (green stars) and QD_B (orange stars). The curves are fit to the data with Eq. 4.1. (b) The excitonic transitions' linewidth is measured at each excitation power for QD_A (green circles) and QD_B (orange circles). The bottom axis is converted to Rabi frequency with Eq. 4.2. The power broadening is fitted with Eq. 4.3 (dashed curves).

which holds in the absence of dephasing, where b accounts phenomenologically for broadening mechanism such as spectral diffusion (Arcari 2015). The latter can be better characterized by fitting the low-power spectra to a Voigt function (not shown), as introduced in section 1.5.2, from which we extract $\sigma_A = 68 \pm 4$ MHz and $\sigma_B = 163 \pm 25$ MHz for QD_A and QD_B respectively, after fixing the Lorentzian contribution to the lifetime-limited value.

We then fix the power at which the following measurements are performed at 2 μW, as indicated in Fig. 4.6(a), and the corresponding Rabi frequencies are shown in Fig. 4.6(b), which ensures to be in the middle power regime (Michler 2017).

4.4 Second-order correlation of individual quantum dots

After finding the parameters for which two quantum dots are in mutual resonance and understanding the effect of power on the saturation, we go on with measuring the second-order correlation of each quantum dot. To do so, we send the signal from QD_A and QD_B to the TPQI-breadboard, and by subsequently blocking one arm of the MZI, we measure the filtered excitation spectrum of each quantum dot followed by the coincidence counts on the detectors after the FBS. The first measurement is shown in Fig. 4.7(a), from which we read similar maximum detected intensity. The value differs from the one in Fig. 4.6(a) since the efficiency of the TPQI-breadboard must be taken into account.

In these experimental conditions, the second-order correlation functions are measured for each quantum dot when corresponding voltages are set to address them on resonance with the laser. The coincidence counts normalized by the value at long time delay are shown in Fig. 4.7(b) as a function of the time delay τ between detection events. The errorbar on each data point is extracted from Poissonian statistics. Both quantum dots reveal a strong antibunching for $\tau = 0$, characterized by $g_A^{(2)}(0) = 0.13 \pm 0.02$ (top) and $g_B^{(2)}(0) = 0.04 \pm 0.015$ (bottom). The deviation from $g^{(2)}(0) = 0$ is partly explained by the SNR due to imperfect laser suppression, since $g^{(2)}(0) = 2\xi - \xi^2$, where the impurity $\xi = 1/\text{SNR}$ (Kako et al. 2006). In this experiment, the SNR can be extracted by recording the intensity at a voltage $V = 1$ V for which no charge state is excited and is measured after performing the RF scan in Fig. 4.7(a). The SNR is 30 for QD$_A$ and 58 for QD$_B$, which would result in lower $g^{(2)}(0)$ than measured. We attribute the discrepancy to the different timescales of the measurements since the laser background is measured over 40 s and the second-order correlation function over 10 min. The second-order correlation functions at $\tau = 0$ clearly show that single emitters are addressed and demonstrate a decent laser suppression from the dual-mode waveguides.

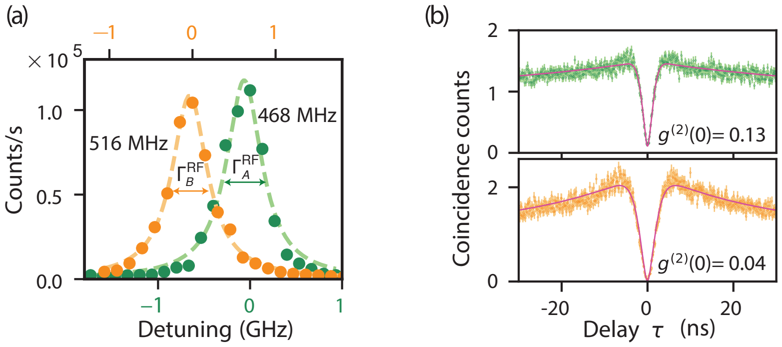

FIGURE 4.7: Second-order correlation measurement for two quantum dots excited simultaneously. (a) Resonance fluorescence is recorded for each quantum dot as a function of the detuning to the cw-laser. The fluorescence is filtered through the TPQI-breadboard and is subsequently detected for QD$_A$ (green curve) and QD$_B$ (orange curve). (b) The second-order correlation function was measured for each quantum dot after blocking subsequently one arm of the TPQI-interferometer. The pink curves are a fit to Eq. 4.4.

The second-order correlation functions are fitted with the derived $g_{\text{RF}}^{(2)}(\tau, \gamma, \Omega)$ from Eq. 1.15 to which we add an additional exponential term to model the blinking seen at short time delay (Schwartz et al. 2018), such that the full model is

$$g^{(2)}(\tau, \gamma, \Omega) = g_{\text{RF}}^{(2)}(\tau, \gamma, \Omega)(1 + C_{\text{b}} e^{-\gamma_{\text{b}}\tau}), \tag{4.4}$$

where C_b and γ_b are the amplitude and decay rate of the bunching, respectively. Moreover, we convolute the signal with the response function of the detector given by the 96 ps time jitter. To fit the second-order correlation functions, we fix the Rabi frequency to $\Omega_A = 0.48\gamma_A$ and $\Omega_B = 0.34\gamma_B$ for QD$_A$ and QD$_B$ respectively. The radiative decay rate from are fitted to be

$\gamma_A = (1.46 \pm 0.03)$ ns^{-1} and $\gamma_B = (1.05 \pm 0.01)$ ns^{-1}. The bunching accounts to the signal with amplitude $C_\text{b} = 0.48$ ($C_\text{b} = 1.13$) and decay rate $\gamma_\text{b} = (0.0218 \pm 0.0005)$ ns^{-1} ($\gamma_\text{b} = (0.0356 \pm 0.0004)$ ns^{-1}) for QD$_A$ (QD$_B$). We attribute the blinking experienced by both QDs to the interaction with phenomenological dark states (Davanço et al. 2014), which originates from the fluctuating charge environment around the QDs. The long tail of this noise is measured to be independent of the power applied, while the area close to $\tau = 0$ becomes narrower in time with increasing power due to the onset of Rabi oscillations (Flagg et al. 2009).

We finally want to compare the extracted decay rate for each quantum dot to a time-resolved fluorescence measurement. To do so, we swap the CTL with the MIRA pulsed laser centered at a frequency that can excite the quantum dots through their individual p-shell resonances. We found resonances at 919.88 nm for QD$_A$ and 922.60 nm for QD$_B$. The signal is then filtered through a grating filter (22 GHz bandwidth) before the etalon. The result is shown in Fig. 4.8 for QD$_A$ (top) and QD$_B$ (bottom). The gray dashed curve shows the instrument response function.

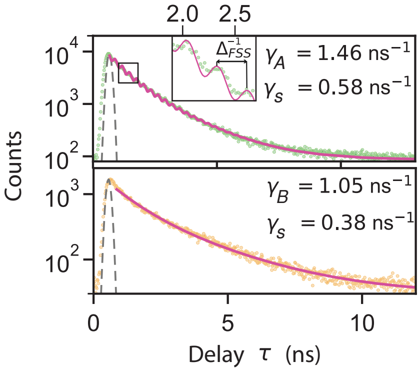

FIGURE 4.8: Lifetime of two quantum dots with p-shell excitation through the waveguide. The fit to a double exponential is shown for QD$_A$ (top) and QD$_B$ (bottom) as the pink curves. The fit to QD$_A$ includes an oscillating term (inset) from the pronounced second dipole, with a frequency $\Delta_{FSS}/2\pi = 3.453 \pm 0.006$ GHz.

Both decay curves are fitted with a double-exponential, where the fast decay rate is fixed to the one extracted from the fit of the second-order correlation function. For QD$_A$, the fact that the second dipole is excited by the pulsed laser is expressed as the beating in the decay curve (Flissikowski et al. 2001), shown in the inset. We fit the decay curve by including a rotating term in the exponential decay as

$$I(\tau) = |\sqrt{A_f}e^{-\frac{\gamma_A}{2}(t-t_0)} + \sqrt{A_s}e^{i(\Delta_\text{FSS}(t-t_0)+\phi)}e^{-\frac{\gamma_s}{2}(t-t_0)}|^2, \tag{4.5}$$

where t_0, A_f, Δ_FSS, ϕ, and A_s are the starting time of the decay, the amplitude of the fast decay rate γ_A, the fine structure splitting, the constant phase and the amplitude of the slow decay rate γ_s, respectively. With a constant phase of $\phi = 3.24 \pm 0.02$, the fine structure splitting is fitted to $\Delta_{FSS}/2\pi = 3.453 \pm 0.006$ GHz, which is in accordance with the spectrum of

Fig. 4.5(b). Therefore, we assume that the slow decay rate is the contribution from the second dipole and extract the slow decay rate of $\gamma_s = 0.578 \pm 0.006$ ns^{-1}. This assumption is corroborated by the ratio of the fitted amplitude $A_f/A_s = 1.9$, which matches the relative intensity shown in Fig. 4.5(b). The decay curve of QD$_B$ follows a simple double-exponential, which matches with the absence of a pronounced second dipole. The slow decay rate is fitted with $\gamma_s = 0.384 \pm 0.005$ ns^{-1}, and we attribute it to the interaction with non-radiative states (Johansen et al. 2010). The fit, in this case, started a couple of nanoseconds after the start of the decay to mitigate the fast component from the laser leakage, which was not fully suppressed in this experiment.

In conclusion, from the agreement between the measured decay curves and the bi-exponential model, we extract the lifetime-limited contribution to the linewidth of $\Gamma_A = \gamma_A/2\pi = 233$ MHz and $\Gamma_B = \gamma_B/2\pi = 167$ MHz for QD$_A$ and QD$_B$ respectively. These are the values used in section 4.3.3 for extracting the Rabi frequency.

In this section, we demonstrated that the dual-mode waveguides, in combination with individual Stark tuning, allow exciting simultaneously two quantum dots. The measured second-order correlation functions for both QDs show strong antibunching behavior limited by the laser leakage. We also acquired a better understanding of the dynamics of each QD. We assume the contribution from the pure dephasing γ_d to be negligible. From the pulsed HOM experiment on the same platform, it was extracted to be $\gamma_d = 0.2$ ns^{-1} (Uppu et al. 2020a), so it contributes moderately to the loss of coherence and linewidth broadening. Moreover, since the dephasing rate is not measured directly in the present experiment, we chose to neglect it and focus on the effect of spectral diffusion. In the next section, we use the TPQI-breadboard and probe the non-classical effect between two photons emitted by two quantum dots tuned in resonance.

4.5 Two-photon quantum interference from two quantum dots

The low-noise characteristic of the two resonant QDs demonstrated earlier enables performing two-photon quantum interference measurement. We realize a Hong-Ou-Mandel experiment with the balanced Mach-Zender-Intererometer (MZI) under cw-excitation, presented in Fig. 4.2(a), using the same excitation power condition as for the measurement of the second-order coherence function. The $\lambda/2$-waveplate in one of the paths sets the relative polarization of the two arms of the MZI. When the photons are orthogonally-polarized, i.e. fully distinguishable, the probability $g^{(2)}_{\perp}(\tau)$ of detecting photons on both detectors as a function of the time delay τ between the two events is (Lettow et al. 2010; Patel et al. 2010)

$$g^{(2)}_{\perp}(\tau) = c_A^2 g^{(2)}_A(\tau) + c_B^2 g^{(2)}_B(\tau) + 2c_A c_B, \tag{4.6}$$

where $c_n = I_n/(I_A + I_B)$ and I_n is the intensity recorded for QD$_n$ (for $n \in \{A, B\}$) before the HOM measurement. The cross-polarized measurement is shown in Fig. 4.9(a) (pink dots, top) together with the prediction from Eq. (4.6) (gray curve), which is calculated with the fitted $g_n^{(2)}(\tau)$ from Fig. 4.7(b).

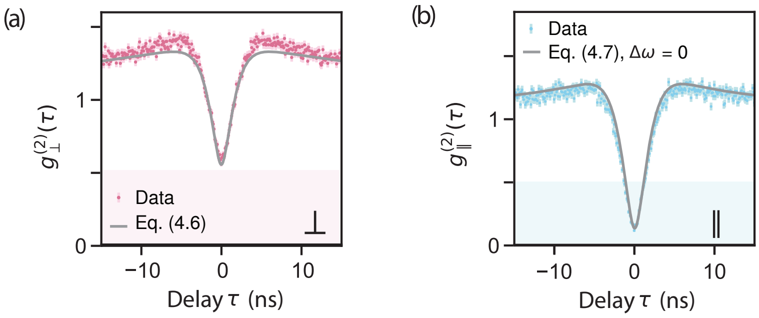

FIGURE 4.9: Two-photon quantum interference between two quantum dots excited simultaneously. (a) Coincidence counts between two detectors at the output of the TPQI-breadboard, measured for cross-polarized photons. The gray curve shows the prediction of Eq. (4.6) given the fitted $g^{(2)}(\tau)$ from Fig. 4.7(b). (b) Two-photon interference occurs for co-polarized photons (bottom). The plain gray curve is the result of Eq. (4.7) for $\Delta\omega = 0$. The shaded regions indicate the threshold below which non-classical effects occur.

TPQI is observed when rotating the HWP in the MZI such that both arms have the same polarization, which results in a vanishing coincidence function at short time delays τ. Such a measurement is shown in Fig. 4.9(b) (blue dots, bottom) with an observed TPQI dip reduced much below the classical threshold of 0.5. The TPQI can be modelled with (Lettow et al. 2010; Patel et al. 2010)

$$g_{\parallel}^{(2)}(\tau) = c_A^2 g_A^{(2)}(\tau) + c_B^2 g_B^{(2)}(\tau) + 2Rc_Ac_B \times \\ \left[1 - \zeta_A\zeta_B |g_A^{(1)}(\tau)||g_B^{(1)}(\tau)| \cos(\Delta\omega\tau)\right], \quad (4.7)$$

where R is a constant to ensure that $\lim_{|\tau|\to\infty} g_{\parallel}^{(2)}(\tau) = 1$ (Woolley et al. 2013), due to the excitation scheme (resonant excitation with medium Rabi frequency) we have that $\lim_{|\tau|\to\infty} g^{(1)}(\tau) \neq 0$, in opposition to previous works, where non-resonant excitation (Lettow et al. 2010) or high Rabi frequencies in RF (Gerber et al. 2009) are used. The residual laser photons account for imperfect interference through $\zeta_n = \sqrt{1 - g_n^{(2)}(0)}$, which ensures that the SNR impact on both the photon statistic and interference is taken into account. The first-order coherence function $g_n^{(1)}(\tau)$ of QD$_n$ is a function of the lifetime of the emitters, Rabi frequency and dephasing (Scully et al. 1997) and is calculated with the measured parameter γ_A, γ_B, Ω_A, and Ω_B, while here again the dephasing rate is neglected since it is not measured directly. For QDs fully resonant during the experiment, we have $\cos(\Delta\omega\tau) = 1$, where $\Delta\omega$ is the frequency detuning between the two emitters. The plain gray curve in Fig. 4.9(a)(bottom) is the expected $g_{\parallel}^{(2)}(\tau)$ for $\Delta\omega = 0$, where only the normalization constant R is left as a free parameter, which is fitted to $R = 1.800 \pm 0.005$. The measured TPQI is well described by the model; we, however, note that the time response of the measured TPQI is slower than from calculation, which indicates a slight overestimation of the decay rate and/or Rabi frequency. This can be corrected in the future by directly measuring the first-order coherence. The cross- and co-polarized correlation functions were integrated for 6 min, with a bin size of 100 ps and correlation range of 100 μs. The error bars on the data points follow Poissonian statistics.

The visibility of the HOM measurement, defined as $V(\tau) = 1 - \frac{g^{(2)}_{\parallel}(\tau)}{g^{(2)}_{\perp}(\tau)}$, is displayed in Fig. 4.10 and reveals a peak of $(79 \pm 2)\%$. The plain gray curve, which is the visibility calculated with $\Delta\omega = 0$, shows a significant overlap with the measured data, both in width, governed by the dynamics of the QDs, and in peak value, limited here by the laser leakage measured in Fig. 4.7(b). From this overlap, we conclude that the main limitation to the visibility of $V = (79 \pm 2)\%$ is the finite $g^{(2)}(0)$ and, therefore, the laser suppression through the structure. Surprisingly, although low-power RF scans indicate the presence of slow spectral diffusion for both QDs, the TPQI dip and hence the visibility peak can be fairly well explained without taking this effect into account.

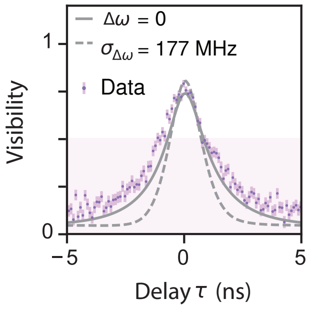

FIGURE 4.10: Visibility of the two-photon quantum interference from two quantum dots, with peak visibility $V = (79 \pm 2)\%$. The plain gray curve is the calculated visibility with $\Delta\omega = 0$, while the dashed curve is the predicted visibility averaging over a random width distribution $\sigma_{\Delta\omega} = 177$ MHz. The shaded region indicates the threshold above which non-classical effects occur.

To interpret this result, we also calculate the visibility curve when assuming that the spectral diffusion experienced by the two QDs is fully uncorrelated, meaning that, although the two QDs are tuned into resonance, their frequency detuning $\Delta\omega$ varies stochastically. In this case, the mutual detuning, on average $\overline{\Delta\omega} = 0$, would follow a normal distribution with $\sigma_{\Delta\omega} = 177$ MHz, given by $\sqrt{\sigma_A^2 + \sigma_B^2}$ from section 4.3.3, which are the standard deviation of the Gaussian distribution convolving the low-power spectra of the individual dots. We then calculate the expected visibility from an ensemble average of Eq. 4.7, with a fitted constant $R = 0.875 \pm 0.004$. We observe an apparent deviation from this model in terms of the peak width, as shown in Fig. 4.10 (dashed gray curve), which indicates that, although slow noise processes are present in individual QDs, the dominant noise sources are not entirely uncorrelated. This points towards the lines for distributing the electrical signal as the origin of this noise, potentially correlated. We note that the calculated peak value of the visibility curves differs, which is due to the uncertainty added by the ensemble average and the normalization of the TPQI expression. Finally, we acknowledge that spectral diffusion of the individual QD also influences their respective correlation functions and the exact Rabi frequency at which they are driven. However, even when striving to take these uncertainties into account (not shown here), the HOM visibility cannot be modeled with an ensemble of mutual detunings with distribution $\sigma_{\Delta\omega} = 177$ MHz. This is a strong sign that the detrimental effect of spectral diffusion on the TPQI is not as severe as anticipated.

4.6 Two-photon quantum interference from individual quantum dots

This experiment aimed to demonstrate the simultaneous resonant excitation of two quantum dots, which can then be used to demonstrate two-photon quantum interference between two resonant emitters. Our setup can, however, also be used to measure TPQI from individual quantum dots. To do so, we add a 15 m fiber in one arm of the MZI of the TPQI-breadboard, which yields a 75 ns delay between the two arms Proux et al. 2015 and a rotating half-wave plate after the etalon filter, which ensures that the photons from each QD are equally distributed in the two arms of the MZI. This allows probing of the interference between photons emitted from the same QD. The result is shown in Fig. 4.11(a) for QD$_A$ and Fig. 4.11(b) for QD$_B$. The excitation power is the same as in the previous experiment. For both QDs, we see a strong sign of two-photon interference. However, both the cross-polarized and co-polarized measurements are greatly spoiled at $\tau = 0$ due to the large laser leakage in this experiment, which is also measured in the second-order correlation (not shown).

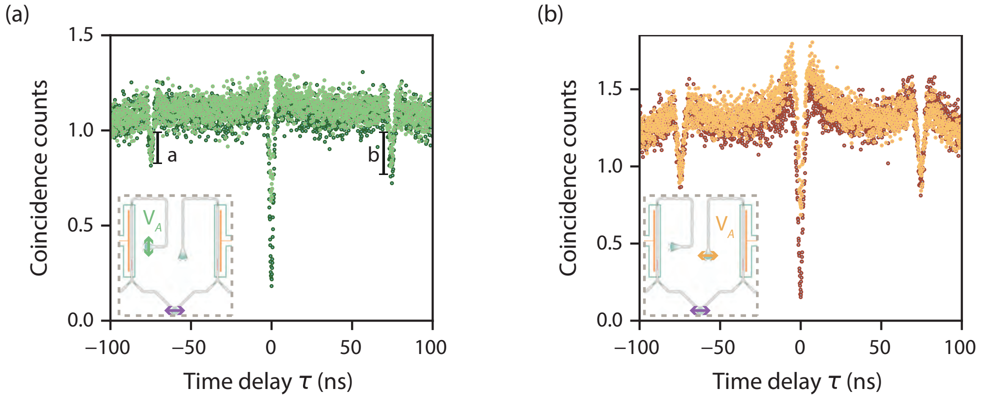

FIGURE 4.11: Two-photon quantum interference for QD$_A$ (a) and QD$_B$ (b) measured individually, as shown in the figure insets. For this measurement, a delay fiber of 15 m was introduced in one arm of the MZI, leading to the side dips, shifted by $\pm\Delta\tau = 75$ ns. Both $g^{(2)}_{\parallel}(\tau)$ and $g^{(2)}_{\perp}(\tau)$ deviate from the ideal value, mainly due to the low SNR in this experiment.

The side dips are given by the delay of the MZI and correspond to a situation where coincidence detection can happen with 25% probability. Quantum interference does not occur at the side dip (Proux et al. 2015), but the asymmetry can be linked to the ratio between the transmission and reflection of the FBS. The slight asymmetry between the side peaks reveals that the rotating half-wave plate after the etalon could compensate for the imperfect splitting ratio of the FBS.

4.7 Pulsed excitation

The measurements presented earlier were all performed under cw-excitation. In this case, determining the indistinguishability of the photon wave packets from the two-photon quantum interference is not straightforward since the visibility at $\tau = 0$ is ultimately limited by the time resolution of the detection rather than the quantum dot properties. Indeed, independently of the dephasing or spectral diffusion, if the visibility is post-selected at $\tau = 0$, the interference is expected to be preserved, meaning $g_{\parallel}^{(2)}(0) = 0$ (Flagg et al. 2010). The effect will be seen as a narrowing of the visibility curve, which in practice can lead to lower visibility due to the finite time resolution of the detection. Alternative methods exist to extract indistinguishability from incoherent cw-excitation (Schofield et al. 2022) or to give another metric, like the coalescence time window (Proux et al. 2015).

To extract this number accurately, the two-photon interference must be performed under pulsed resonant excitation, where the emission of single photons is triggered. We, therefore, go on with exciting the two quantum dots with a pulsed resonant laser. For this, we use a stretched Mira pulse centered at the frequency of the two quantum dots, with a Gaussian FWHM of 24 GHz, as shown in Fig. 4.12(a). We perform a π-pulse on each quantum on their separate input in the first place, as shown in Fig. 4.12(b) and 4.12(c) for QD$_A$ and QD$_B$ respectively.

The SNR on both measurements drops dramatically in the pulsed excitation compared to the cw-excitation, due to the larger bandwidth of this excitation method (Schwartz et al. 2016). At any power, the SNR does not exceed 5, which is too low to perform a two-photon experiment. This is explained by the limited performance of the two nanophotonic devices for pulsed excitation, already highlighted in the cw-experiments, since the peak power is increased in the pulsed excitation. We attribute this limitation to the performance of the photonic crystal filter, which is diminished due to fabrication imperfections of the photonic crystal holes combined with the y-splitter spectral response (Uğurlu 2021).

In this chapter, we operated the photonic device specially designed to perform the resonant excitation of quantum dots embedded in dual-mode waveguide single-photon sources. By distributing a single laser, it is possible to excite resonantly two quantum dots, which are brought in mutual resonance by individual DC-Stark tuning. We demonstrated that the device provides good laser suppression by measuring the second-order correlation function, enough to measure a convincing two-photon quantum

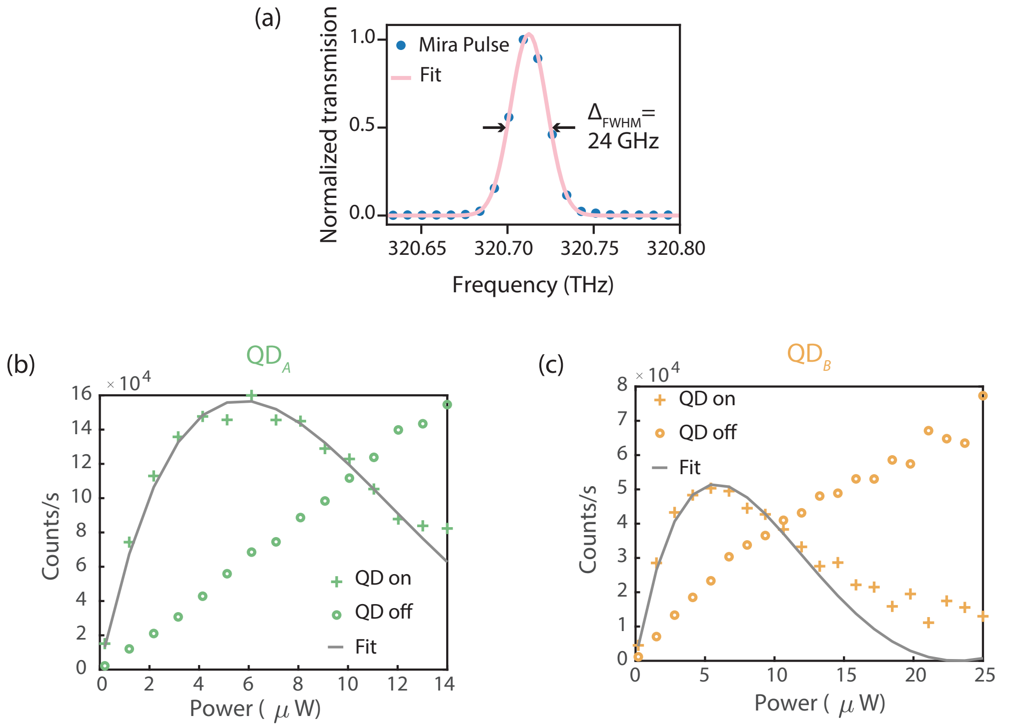

FIGURE 4.12: Pulsed excitation of two waveguide-based single-photon sources. (a) The spectrum of the stretched Mira pulses, fitted to a Gaussian of FWHM 24 GHz. The power saturation in pulsed excitation of QD_A (b) and QD_B (c) shows a π-pulse, however, the SNR is low due to higher peak power.

interference between two different resonant quantum dots. The device performance was, however, not good enough in terms of laser suppression to repeat the experiment with pulsed excitation. This is needed to measure indistinguishability and operate the quantum dots as deterministic single-photon sources. The promising prospect of scaling single-photon sources on a chip necessitates a strategy more robust to fabrication imperfections, which we address in the next chapter.

5 Towards on-chip multi-photon experiment

In the previous chapter, we strove to demonstrate the potential to assemble different elements of the planar quantum photonic platform to achieve a scalable architecture of single-photon sources. This strategy allowed us to demonstrate the simultaneous operation of two mutually resonant quantum dots integrated into dual-mode waveguides. However, the moderate laser suppression prevented us from realizing resonant pulsed excitation with a good signal-to-noise ratio. The first limitation arises from the narrow bandwidth of the device presented in (Uppu et al. 2020a), which is a characteristic of photonic crystal filters. This implies that not only the quantum dots must be in resonance with each other, but their resonant frequency should also overlap with the spectral window of high laser suppression offered by the device. Moreover, the radius of the photonic filter holes is subjected to enlargement after fabrication (Pregnolato 2019), which impairs the maximal laser suppression extracted from the simulation detailed in Ref. (Uğurlu 2021). Disorder in the hole size induced by fabrication can also break the perfect periodicity of the photonic crystal filter and modify its transmission spectrum.

These are the facts that motivated the development of another strategy to perform resonant excitation in the dual-mode waveguide without resorting to a photonic crystal filter. In Ref. (Uğurlu 2021), it was found that this can be achieved through an asymmetric directional coupler (ADC), which relies on bringing a single-mode and a dual-mode waveguide close to each other to induce power transfer in the TE1 mode without exciting the TE0 mode of the dual-mode waveguide. This technique does not rely on a photonic filter, so we anticipate it will be more robust to fabrication disorder. Moreover, the fabricated width of the nanobeam waveguide can be accurately controlled by applying a correction factor (Pregnolato 2019).

In this chapter, we will introduce the design of the device to be tested against fabrication variations. We will then demonstrate resonance fluorescence using the novel device for circuit-based resonance fluorescence with asymmetric directional couplers. Since the emission of single photons is bidirectional in waveguides, this device can be considered an integrated source of dual-rail encoded photons. Finally, we will present a few-photons application for this integrated source, where upscaling to $N = 4$ sources on the same chip combined with linear operations and interference can lead to the generation of a two-photon heralded entangled state.

5.1 Asymmetric directional couplers for resonant excitation of quantum dots

Evanescently coupled waveguides enable important on-chip functionalities to control and manipulate light propagation. For example, two coupled single-mode waveguides enable the transfer of optical power from one waveguide to the other, with a ratio that can be controlled by modifying the gap distance between the waveguides. Combined with a quantum dot, such a device demonstrated on-chip single-photon routing (Papon et al. 2019). There are numerous examples in classical photonics on the use of asymmetric and tapered directional couplers, which have been used to perform mode multiplexing in multi-mode waveguides (Ding et al. 2013; Wang et al. 2015). These devices rely on the perfect index matching between the TE0 of a single-mode waveguide and the TE1 of a multi-mode waveguide for efficient power transfer. In our case, we can use this technique to transfer a fraction of the optical power to the TE1 mode of the dual-mode waveguide while ensuring negligible power coupled to the well-confined TE0 mode of the dual-mode waveguide. This is ultimately the condition to ensure the absence of laser photons in the TE0 mode. Once the TE1 mode is pumped in the dual-mode waveguide, the condition on the excitation of off-centered quantum dots is the same as introduced in Chapters 2 and 4.

5.1.1 Design

The working principle is shown in Fig. 5.1(a), where a single-mode waveguide of width w_{SM} is brought in the vicinity of a dual-mode waveguide of width w_{DM}, at a gap distance g. By coupling a laser for excitation in the $\mathrm{TE0}_{\mathrm{SM}}$ of the single-mode waveguide, optical power is exchanged between the $\mathrm{TE0}_{\mathrm{SM}}$ mode and the $\mathrm{TE1}_{\mathrm{DM}}$ mode of the dual-mode waveguide over an interaction length L. By carefully choosing the length and the widths of the two waveguides, the $\mathrm{TE1}_{\mathrm{DM}}$ mode can be excited in the dual-mode waveguide with an insignificant transfer of optical power the $\mathrm{TE0}_{\mathrm{DM}}$ mode of the dual-mode waveguide. To gain intuition into this effect, we show in Fig. 5.1(b) the effective refractive index of the TE0 and TE1 modes as a function of waveguide width, simulated with a two-dimensional finite-element method (FEM). The maximum power transfer between the $\mathrm{TE0}_{\mathrm{SM}}$ mode of the single-mode waveguide and the $\mathrm{TE1}_{\mathrm{DM}}$ of the dual-mode waveguide occurs when the two modes are phase-matched, $\Delta n_{\mathrm{eff}} = 0$. On the contrary, the $\mathrm{TE0}_{\mathrm{DM}}$ mode is very well confined within the core of the dual-mode waveguide and therefore exhibits a large index mismatch with the $\mathrm{TE0}_{\mathrm{SM}}$ mode of the single-mode waveguide. This can be further highlighted by calculating the transmission through the ADC with three-dimensional FEM as a function of the coupling length L, shown in Fig. 5.1(c) for waveguide widths optimized to minimize laser transmission through the ADC (Uğurlu 2021) (indicated by the black vertical lines in Fig. 5.1(b)). The transmission between the two TE0 modes is strongly suppressed, while the transmission to the $\mathrm{TE1}_{\mathrm{DM}}$ mode is high over the whole range. The optimal extinction ratio between the TE1 and TE0 modes in the dual-mode waveguide is achieved for a coupling length of $3~\mu$m. The effect of the gap variation is also investigated by reproducing the FEM simulations with different gap distances, showing that increasing the gap distance slightly increases the overall optical power transferred to the dual-waveguide modes but does not severely impact the laser extinction between $\mathrm{TE1}_{\mathrm{DM}}$ and $\mathrm{TE0}_{\mathrm{SM}}$.

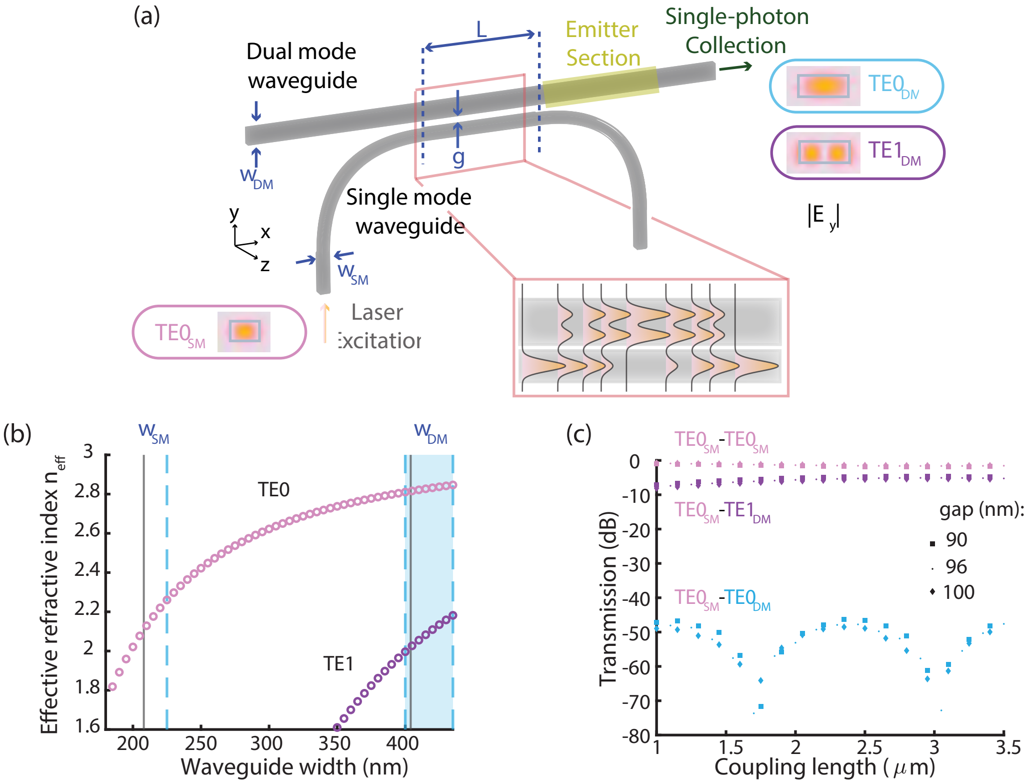

FIGURE 5.1: (a) Schematic of the working principle of the asymmetric directional coupler for resonant excitation of quantum dots in dual-mode waveguides. Adapted from (Uğurlu 2021). (b) Effective refractive index of the TE0 and TE1 mode as a function of waveguide width. The solid gray line indicates the optimal widths from the three-dimensional (3D) FEM simulation, while the dashed blue lines delimit the parameter space for fabrication. (c) Transmission between different modes (from 3D FEM calculation) for different gap distances as a function of the coupling length.

With these parameters at hand, we design ADC structures sweeping the coupling length from 3.2 to $5~\mu$m, fix the width of the single-mode waveguide to 225 nm, and sweep the width of the dual-mode waveguide from 400 to 445 nm. We chose enlarged width values, indicated by blue lines in Fig. 5.1(b), compared to the optimized values from simulation to accommodate the 20 nm shrink in waveguide width after fabrication. Finally, the gap is fixed to 100 nm and will also widen after fabrication. We do not correct this enlargement since its effect is negligible on the performance of the laser suppression.

5.1.2 Initial characterization

One of the fabricated structures is shown in Fig. 5.2(a), where shallow-etched gratings terminate each port of the ADC. The yellow shadow indicates the presence of a large p-electrode close to the structures, to apply a bias voltage across all of them simultaneously. The sample is cooled down to 1.6 K with the same setup presented in section 4.1.

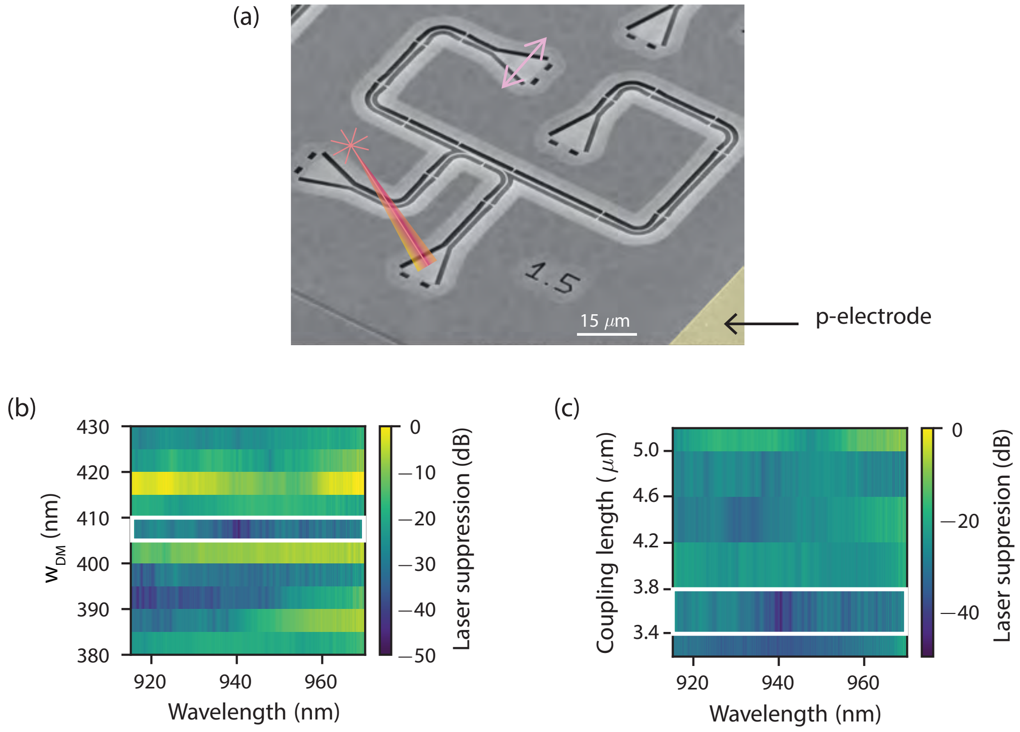

FIGURE 5.2: (a) SEM of the fabricated structure for testing circuit-based RF with asymmetric directional coupler. For initial characterization, a cw-laser is coupled through the SEG, and transmission is collected at the port shown by the pink arrow. (b) Measured transmission through the structure normalized to the transmission through a single-mode nanobeam waveguide of the same length. The measurement is taken for structures with a coupling length of 3.4 μm and increasing dual-mode waveguide widths (measured after fabrication). (c) For a given width of 405 nm, the extinction is measured for increasing coupling length.

To characterize the transmission through the ADC, we couple a CTL laser in one of the inputs of the single-mode waveguide and collect the transmitted signal at the output port indicated by the pink arrow. The transmission is normalized by the reference transmission through a single-mode nanobeam waveguide connecting two SEGs with the same orientation and distance as the one presented in the device picture. For a fixed coupling length of 3.4 μm, we show in Fig. 5.2(b) the laser suppression as a function of the CTL wavelength and the width of the dual-mode waveguide w_{DM} after fabrication, which is extracted from the SEM pictures. We identify a pronounced laser suppression on the structure indicated by the white rectangle at the wavelength around the central emission of the quantum dots.

We claimed earlier that the advantage of the ADC compared to the photonic crystal mode filter would be better robustness to fabrication imperfection. However, we do not see this trend as the waveguide width varies by ± 5 nm. This issue can arise from the presence of a tether at the center of the single-mode waveguide, which was added for more structural stability of the device. This can be removed in the future by modifying the geometry of the directional coupler region.

Similarly, for a dual-mode waveguide of the same nominal width, we probe the effect of the coupling length, as shown in Fig. 5.2(c), but no clear trend arises. However, we can confirm that the best device presents a large laser suppression < -40 dB over 2 nm. Although the tether brings disorder in the spectral response, we found a device within the expected parameter space showing a decent laser suppression. The ultimate test is naturally the measurement of resonance fluorescence from quantum dots, with hopefully an enhanced laser suppression compared to the one that was demonstrated in Chapter 4.

5.2 An integrated source of dual-rail encoded photons

In Fig. 5.3, we present in the middle panel a schematic of the experiment performed. A laser used for excitation is coupled into one of the SEG of the single-mode waveguide, and the mode for excitation is prepared by the ADC. A quantum dot in the dual-mode waveguide, located after the coupling region, is excited and emits single photons in both directions, with $50/50$ probability since the dipoles of the neutral excitons are linearly polarized in the absence of a magnetic field (Coles et al. 2016). The emission is then collected from ports 0 and 1. Considering the direction of the waveguide as a basis for dual-rail encoded qubits, $|0\rangle$ and $|1\rangle$ for the backward and forward direction, respectively, the presented device already provides a qubit described by a coherent superposition $|\psi\rangle = \frac{1}{\sqrt{2}}(|0\rangle + |1\rangle)$. Several of these devices operated in parallel may represent the necessary hardware for on-chip quantum information protocols, as will be introduced later in this chapter.

Meanwhile, we ought to demonstrate the increased device performance by realizing the resonant excitation of quantum dots. The quantum dot search is performed in the same way as in section 4.2. We find a quantum dot resonant at 318.177 THz, and we show on the left and right panels of Fig. 5.3 the resonance fluorescence of this quantum dot as a function of the voltage applied. The first striking feature is the presence of two closely spaced emission lines due to the two bright dipoles of a neutral exciton. This is confirmed by the charge plateau maps shown in section 1.6 of Chapter 1, which indicates that these two excitonic lines tune with the same Stark-shift and are spaced by ≈ 4.5 GHz.

The resonance fluorescence scan is shown from both output ports and indicates a high SNR of 50 at port 0 and 250 at port 1 for the brightest dipole,

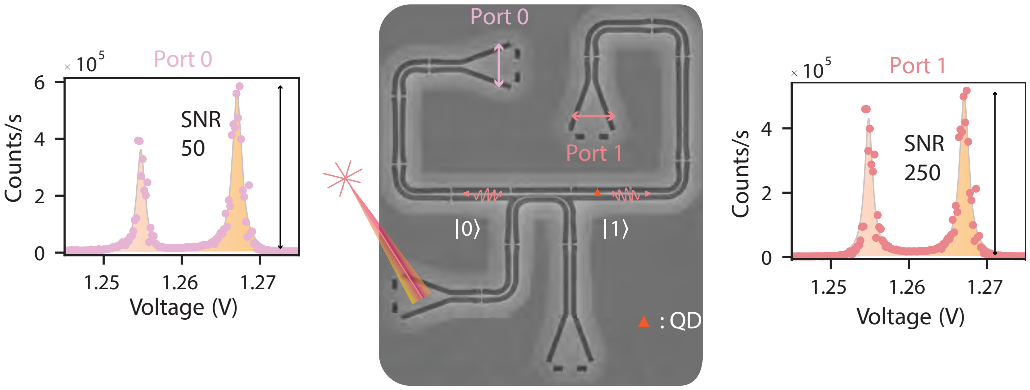

FIGURE 5.3: Asymmetric directional coupler as a source of dual-rail encoded photons. Once a quantum dot is excited, it emits single photons with 50% probability towards port 0 and 50% probability towards port 1. Photons are collected from both outputs, and we show the resonance fluorescence of one quantum dot with two dipoles. The signal-to-noise ratio is indicated for the brightest dipole.

an encouraging sign of improved device performance. We notice that the SNR at port 0 is lower than at port 1, although the laser propagates in the counter direction than the collected signal at port 0. This indicates the occurrence of reflection and scattering into the TE0 mode of the dual-mode waveguide, traveling towards port 0. Removing sources of scattering in future experiments will improve the SNR at port 0 since the direction of the single photons collected there is opposite to the propagation of the laser. Moreover, the SEG at port 0 is co-polarized with the SEG used for excitation so that some residual laser photons might come from specular reflections. Nonetheless, the SNR is low enough at both collection ports that pulsed excitation can be executed.

5.2.1 Pulsed resonant excitation

To perform the resonant excitation of the quantum dot in a pulsed fashion, several elements can be used again from Chapter 4. Firstly, the same stretched pulse from the Mira is used, with a central frequency of 318.177 THz and 24 GHz bandwidth. Secondly, we can use the TPQI-breadboard, introduced in section 4.1.2, to filter single photons collected from the two output ports simultaneously and detect with two individual SNSPDs, after removing the FBS.

We go on by measuring the effect of the average power of the excitation pulse of the RF signal, shown for both dipoles in Fig. 5.4(a). The data presented here for output port 1 are not background corrected, and the strong contrast between the values at off-resonant voltages and the one at resonance showcases the high laser suppression and good coupling of the quantum dot to the waveguide mode. For both dipoles, the RF signal reaches a maximum at a given power, corresponding to full population inversion, called a π-pulse. For increasing power, the RF signal diminishes due to Rabi oscillation, which demonstrates coherent control of the excited state population.

This effect is highlighted by tracking the maximum fluorescence as a function of power for both dipoles, as shown by the white circles and crosses in Fig. 5.4(a). The results are shown in Fig. 5.4(b) and (c), for port 0 and 1 respectively. The RF signal is fitted with $I(P) = I_\infty \sin^2(\sqrt{2P/P_\pi})$, which gives the power corresponding to a π-pulse, and the latter is indicated by vertical lines in Fig. 5.4(b) and (c) for each dipole. Rabi oscillations are seen as the power is increased, being proportional to the square of the Rabi frequency, however, phonon dephasing (Ramsay et al. 2010) and spectral diffusion damp the oscillation.

In the same figures, we also display the impurity for each transition and each port, which is defined as $\xi = I_{\text{off}}/(I_{\text{on}} - I_{\text{off}})$, where I_{on} and I_{off} are the detected intensities when the quantum dot is tuned on-resonance and off-resonance, respectively, with the applied bias. Only considering the right dipole, indicated by the crosses, we extract an impurity of $\xi_0 = 0.045$ and $\xi_1 = 0.03$ for port 0 and 1, respectively. With this measured impurities, we would expect $g_0^{(2)}(0) = 0.088$ and $g_1^{(2)}(0) = 0.049$ if the second-order correlation was measured at each port individually (Kako et al. 2006).

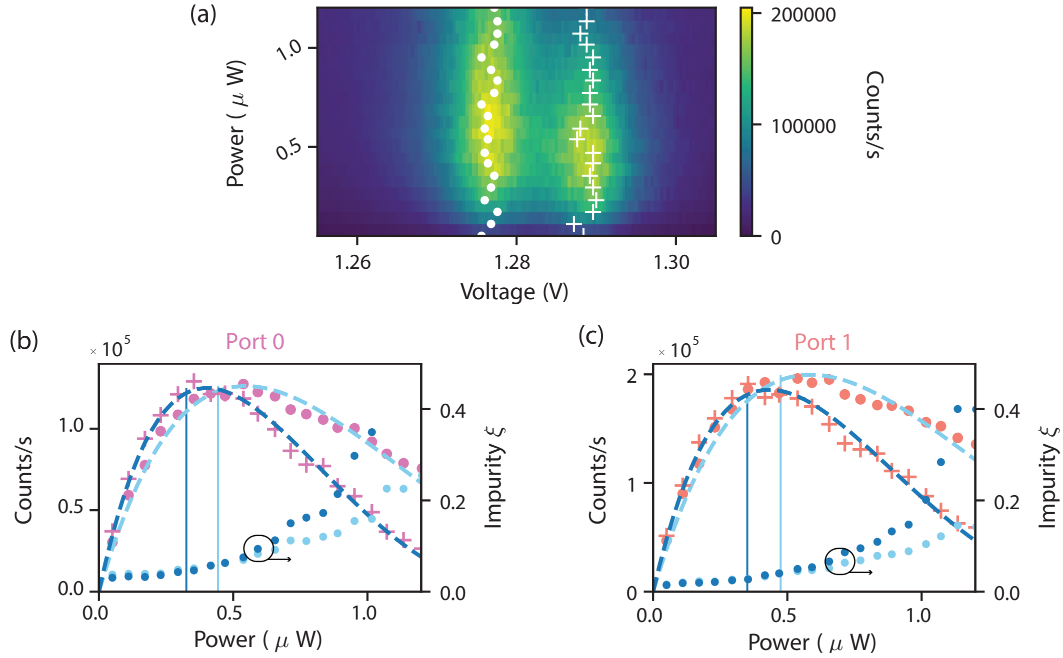

FIGURE 5.4: Rabi oscillation of a quantum dot excited resonantly with the ADC-based pumping scheme. (a) The RF signal is collected at port 1 as a function of the input average power and the voltage across the waveguide. No background correction. The RF peaks are extracted for signal collected at port 0 (b) and port 1 (c) and fitted to a square sine for both dipoles (pink circles and crosses). A vertical line indicates the power at which π-pulse is achieved. The impurity is also displayed for each dipole (circles).

Since the quantum dot emits in both directions and we collect the signal from the two output ports, we can measure the second-order correlation by simply registering the coincidence counts as a function of the time delay between detection events at port 0 and 1. The single photons emitted by the dipole centered at 1.289 V are filtered through the etalon beforehand. We show the second-order correlation function measured in this way, at the power corresponding to the π-pulse, in Fig. 5.5(a). Contrarily to the cw-excitation case, the emission from the quantum dot is triggered at discrete time intervals, and therefore, the coincidence counts are distributed in peaks, whose spacing is given by the repetition rate of the pulsed laser of 13.8 ns. We denominate the time interval over which each peak is defined as $[\tau]$. If the quantum dot emits one photon at most per excitation pulse, the central peak, which gives the probability of detecting more than one photon at the same time, should vanish. We measure residual coincidence counts at $[\tau = 0]$, which are linked to the average impurity in the RF signal.

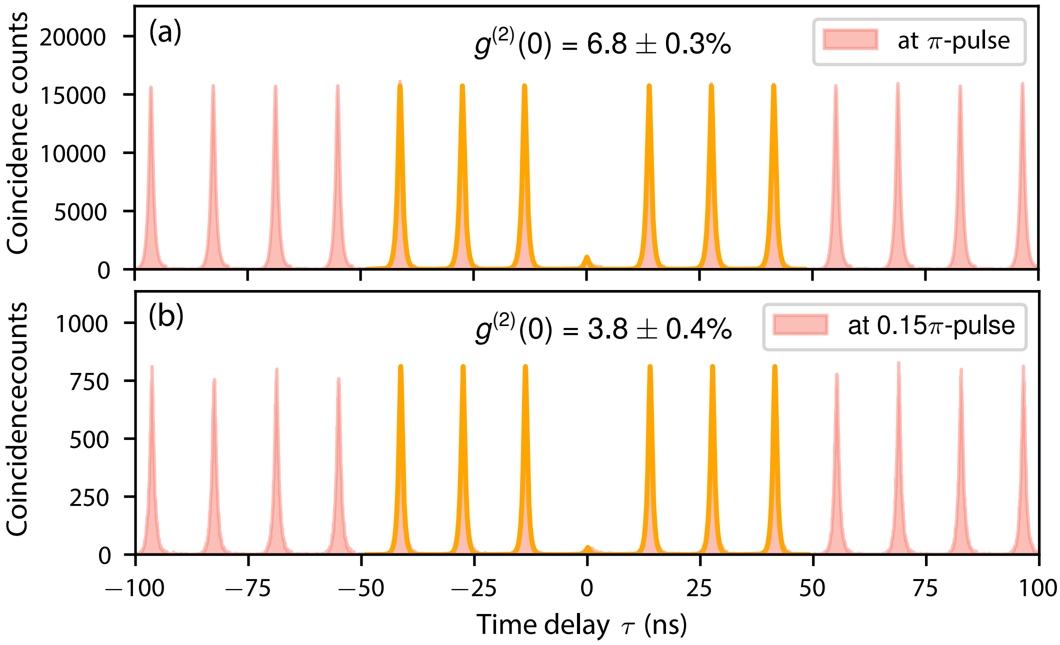

FIGURE 5.5: Second-order correlation function between the two output ports of the ADC-based single-photon source, for a power corresponding to (a) a π-pulse and to (b) a 0.15π-pulse. The orange lines correspond to the fit to an exponential decay, allowing to integrate the area under the peak at $[\tau = 0]$. The latter is then normalized to the area of a peak at $[\tau = 50\ \mu\text{s}]$ to calculate $g^{(2)}(0)$.

The second-order correlation function is fitted by two-sided exponential functions, with a time constant given by the radiative lifetime of the transition, in this case, fitted to $\tau = 468 \pm 3$ ps. To estimate the area under the fitted peak at $[\tau = 0]$, the contribution for the 3 closest peaks on each side is taken into account. The area $A[\tau]$ under the peak at $[\tau = 0]$ is then normalized by the area under a peak at delay $[\tau = 50\ \mu\text{s}]$ to alleviate the effect of potential blinking on a short time scale, such that

$$g^{(2)}(0) = \frac{A[\tau = 0]}{A[\tau = 50\ \mu\text{s}]}. \tag{5.1}$$

This yields the value $g^{(2)}(0) = (6.8 \pm 0.3)\%$, with the error extracted from the fit. By normalizing $A[\tau = 0]$ to a peak closest in time, such as $A[\tau = 500\text{ ns}]$, we get $g^{(2)}(0) = (6.7 \pm 0.3)\%$, which indicates that blinking to dark states is low for this quantum dot. We estimate that the deviation from $g^{(2)}(0) = 0$ is indeed due to the imperfect laser suppression and not multiphoton emission from the quantum dot, since the average impurity measured on each port, displayed in Fig. 5.4(b) and (c), is $\bar{\xi}(P \sim P_\pi) = 0.0375$, yielding $g^{(2)}(0) = 7.4\%$.

We perform a similar experiment at lower power, corresponding to 15% of a π-pulse, shown in Fig. 5.5(b). In this case we extract $g^{(2)}(0) = (3.9 \pm 0.4)\%$. The intensity fluctuation from peak to peak originates from the higher Poissonian error due to lower counts, which also reflects on the slightly higher error on $g^{(2)}(0)$. Detailed fitting routine is described in (Pedersen 2020), to whom we are obliged for the fitting scripts. Both second-order correlation measurements were acquired over 15 min, with timebins of 10 ps each integrated over 2 s. With the accurate characterization of the purity of the single-photon source based on ADC, we can carry on to the next measurement, namely two-photon quantum interference in the pulsed regime.

5.2.2 Two-photon quantum interference

To finalize the characterization of the ADC-based single-photon source, we measure the spectral mode overlap between two consecutively emitted single photons with a HOM measurement, from which we can extract the indistinguishability of the single photons. To do so, we excite the quantum dot with a π-pulse and send the single photons collected from port 1, showing the lowest impurity at π-pulse, to an unbalanced Mach-Zender interferometer after filtering through an etalon accommodating a single optical mode (3 GHz FWHM). The delay in one of the arms corresponds to the repetition rate of the laser, such that consecutively emitted photons interfere at the last beamsplitter of the unbalanced MZI. Similarly to the setup presented in section 4.1.2, a HWP in one arm of the interferometer allows us to record the coincidence counts at the output of the MZI for photons with parallel and orthogonal polarization. Such a measurement is shown in Fig. 5.6(a), where coincidence counts are gathered in peaks due to the pulsed excitation scheme. For visualization purposes, we normalize the coincidence counts by the maximal value of a peak centered at $\tau = 500$ ns. When the photons impinging the last beamsplitter of the MZI are cross-polarized, the probability of simultaneously detecting two photons in the time bin $[\tau = 0]$ is 50% (pink area). When the photons are made co-polarized by rotating the HWP, the single photons are indistinguishable in all their degrees of freedom, such that the probability of simultaneous detection events should vanish at $[\tau = 0]$ due to two-photon quantum interference.

In Fig. 5.6(b), we zoom on the central peaks, which we normalized by the maximal value of the cross-polarized coincidence peak. The presence of residual coincidences in the co-polarized case reveals imperfect two-photon quantum interference due to several factors, which we will enumerate later.

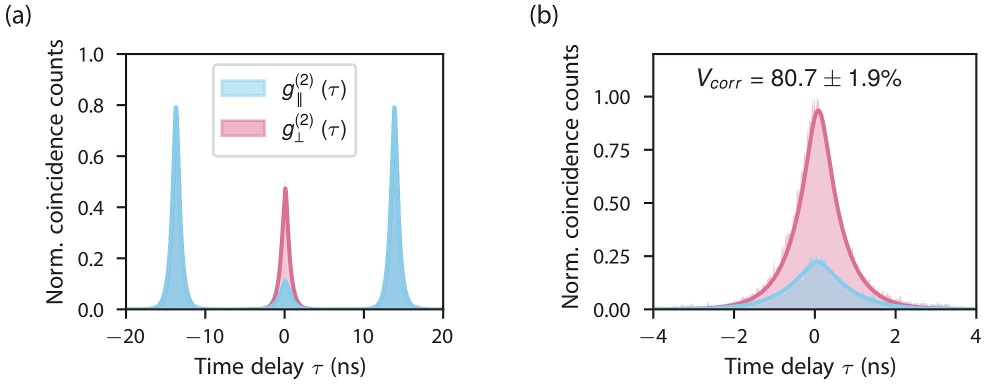

FIGURE 5.6: Hong-Ou-Mandel measurement of the single-photon source based on ADC. (a) Coincidence counts at the output of the MZI for the photons made cross-polarized (blue area) and co-polarized (pink area). Both sets of data are normalized to a peak value at a long time delay. (b) Closeup look on the middle peaks, re-normalized by the peak value of the distinguishable case. The peaks are fitted as double-sided exponential decay convolved with a Gaussian for the instrument time response. The visibility is extracted from Eq. 5.2, and the corrected value is indicated.

To quantify the visibility of the interference, each peak is fitted by a two-sided-exponential decay convolved with a Gaussian function to account for the time jitter of the detectors. The area under each curve is then integrated and normalized by the area of a peak at a long time delay, to account for coincidence counts fluctuations between the measurements with the two polarization configurations. In this way, the visibility of the quantum interference is defined as

$$V_{\text{raw}} = 1 - \frac{A_{\parallel}[\tau = 0]}{A_{\perp}[\tau = 0]}, \tag{5.2}$$

where $A_{\parallel}[\tau = 0]$ and $A_{\perp}[\tau = 0]$ are the normalized areas for the co- and cross-polarized configuration, respectively. From this measurement, a raw visibility of $V_{\text{raw}} = (68 \pm 1)\%$ is extracted. One limitation to the visibility of the HOM measurement arises from a multi-photon component in the signal, characterized by a value of $g^{(2)}(0) = (5.9 \pm 0.5)\%$. The imperfect FBS in the MZI and imperfect polarization control also diminish the visibility. We extract the intrinsic visibility V_{HOM} by correcting the measured visibility according to (Santori et al. 2002)

$$V_{\text{HOM}} = \frac{(R^2 + T^2)[1 + 2g^{(2)}(0)]}{2RT(1-\epsilon)^2} V_{\text{raw}}, \tag{5.3}$$

where $R = 0.476$ and $T = 0.524$ are the FBS reflection and transmission coefficients, respectively, and $(1 - \epsilon) = 0.975$ is the classical visibility of the MZI, measured with the CTL while scanning its frequency. We obtain a value of $V_{\text{HOM}} = (80 \pm 2)\%$, with the error calculated from error propagation. We note that the factor of 2 for the correction due to imperfect suppression of multi-photon events is valid as long as the extra photons are distinguishable from the single photons (Ollivier et al. 2021), which we assume is true since we concluded earlier that the main limitation to $g^{(2)}(0)$ is the SNR.

Decoherence processes such as pure phonon dephasing, a fast process occurring within the lifetime of the quantum dot, can limit the spectral overlap and, thus, the intrinsic visibility of the HOM measurement. The indistinguishability is the measure of spectral overlap between the two interfered single photons, which can be expressed as $V = \gamma/(\gamma + 2\gamma_d)$ (González-Ruiz et al. 2022). Given the decay rate of the considered dipole, measured in an independent measurement to be $\gamma = (305 \pm 3)$ MHz, the pure dephasing rate corresponding to the intrinsic visibility is $\gamma_d \approx 40$ MHz. We obtain $\gamma_d \approx 0.13\gamma$, which is in good agreement with the value extracted in Ref. (Thyrrestrup et al. 2018) for a QD embedded in a multi-mode waveguide. The experiment conducted in a dual-mode waveguide in Ref. (Uppu et al. 2020a) shows a significantly lower pure dephasing rate, which can be attributed to the more centered QD position across the waveguide compared to the present experiment, also highlighted by the better suppression of the second dipole in the cited work.

5.2.3 Resonant transmission measurement

In the previous sections, the measurements of resonance fluorescence as a function of power have highlighted that the two dipoles of the QD can be excited both to π-pulse with similar power. Moreover, the maximum RF intensity is of the same order of magnitude. We would like to understand how well each dipole couples to the TE0 mode of the dual-mode waveguide since from Chapter 2 we know that both dipoles have very different β-factors to the TE0 mode. To do so, we make use of the fact that we can couple the CTL laser to one of the SEG of the dual-mode waveguide and collect in transmission from the opposite SEG of the dual-mode waveguide. In this way, we can measure the resonance transmission as a function of power, from which we can extract the β-factor to the TE0 mode from both dipoles (Thyrrestrup et al. 2018).

When a two-level system is excited with an attenuated cw-laser, the emitted single photons will interfere destructively with the coherent laser in transmission, which results in the transmission dips seen in Fig. 5.7(a) for power at the QD of $P = 0.8$ nW. To perform this measurement, we initially fixed the CTL frequency at 318.77 THz and scanned the voltage applied on the QD for each excitation power. We then converted the x-axis back to frequency by applying the Stark shift of 0.34 THz/V, and the result is shown in Fig. 5.7(b). Note that the order of appearance of the dipoles is then swapped compared to Fig. 5.3 due to the positive Stark shift. We see that the FWHM of the left dipole is larger than the right dipole, which can be explained at first by the radiative decay of 305 MHz and 280 MHz, respectively, calculated from independent lifetime measurement performed under resonant excitation (not shown).

The transmission T as a function of power and detuning Δ to the laser frequency is fitted according to the model presented in Ref. (Türschmann

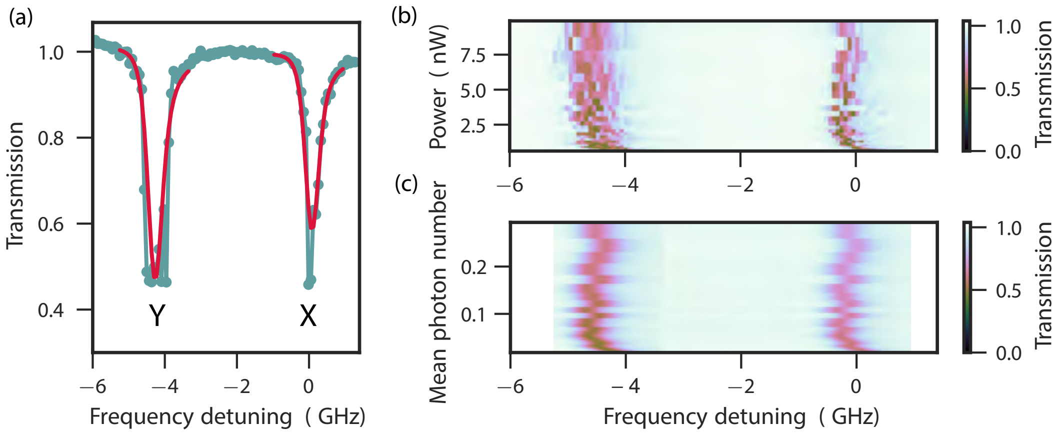

FIGURE 5.7: Resonant transmission of the QD in the dual-mode waveguide. (a) Resonant transmission of the two dipoles at a power $P = 0.8$ nW. The red curves are fit from Eq. 5.4 with the radiative decay fixed to $\gamma = 305$ MHz and $\gamma = 280$ MHz for the first and second dipole, respectively. (b) Resonant transmission as a function of frequency detuning and power at the QD. (c) Fit to the data from the model presented in Eq. 5.4, from which we extract $\beta_{\text{left}} = (65 \pm 3)\%$ and $\beta_{\text{right}} = (43 \pm 2)\%$.

et al. 2019), reading

$$T = 1 + \text{Re}\{\frac{R\gamma(\gamma_2 + i\Delta)}{2\gamma_2^2 + 2\Delta^2 + 8\gamma_2\gamma^{-1}\Omega^2}\}, \tag{5.4}$$

with $R = \beta(\beta - 2z)/|z|^2$ and $z = (1 + i\xi)^{-1}$ accounts for the presence of Fano resonance due to internal reflections in the waveguide (Le Jeannic et al. 2021). We fixed the radiative decay to $\gamma = 305$ MHz and $\gamma = 280$ MHz for the left and right dipole, respectively, and we fixed the dephasing to $\gamma_d = 40$ MHz, which enters in the model as $\gamma_2 = \gamma/2 + \gamma_d$. Finally, the power is converted to the Rabi frequency as $\Omega = \sqrt{\eta P_{\text{in}}}$, where η accounts for the setup efficiency and allows to indicate the power at the QD. The fit to the data is shown in Fig. 5.7(c), and the y-axis is converted to the mean photon number per lifetime, defined as $n = 2\Omega^2/\gamma^2$, γ being fixed to the radiative decay of the right dipole. Moreover, the effect of spectral diffusion is included by performing an ensemble average of a normal distribution of detuning Δ, with average 0 and standard deviation fitted to $\sigma_{\text{sd}} = 76$ MHz. Finally, the β-factor for each dipole is extracted, yielding

$$\begin{aligned} \beta_{\text{Y}} &= (65 \pm 3)\% \\ \beta_{\text{X}} &= (43 \pm 2)\%. \end{aligned} \tag{5.5}$$

According to the β-factor calculation presented in Chapter 2, we would then attribute the largest β-factor to the y-dipole, which translates into a position 80 nm away from the center. For such a location, the x-dipole coupling to the TE0 is much lower than 40%, and from simulation, there are no positions across the waveguide where the x-dipole can exhibit such a high β-factor to the TE0 mode.

We bring up two hypotheses to explain this discrepancy. We assume that only the TE0 mode is excited in the dual-mode waveguide when coupling the laser through one of its attached SEG. However, if the taper is not adiabatic enough, scattering into higher order modes is possible, and the measured β is an average of the β-factor to each mode with appropriate weights. Another possibility is a misalignment between the crystallographic axis and the patterned waveguide. In this case, the projection of the electric field on the different x and y crystallographic axis will also lead to an average effect, with weights controlled by the rotation of the device with respect to the edges of the chip aligned to the crystallographic axis. This hypothesis holds, assuming that the strain is aligned along this axis too. In future fabrication runs, we will keep track of the rotation, probably small, of the pattern and also the direction of the axis on the chip.

5.2.4 Limitations of the current device

The fabricated device has a different geometry than the simulated one shown in Fig. 5.1(a) since we needed to include supporting tethers to avoid structure collapse after fabrication, as shown in Fig. 5.8(a). We are interested in understanding the effect of the presence of tethers for the transmission of optical power into the different modes of the dual-mode waveguide. To do so, we perform a three-dimensional simulation FDTD calculation of the transmission through a structure with parameters as close to the fabricated ones. An input Gaussian pulse, centered at 930 nm and with a bandwidth of ≈ 100 nm, is launched at the bottom left input port of the single-mode waveguide, with power P_{in}. We then look for the transmission coefficients of the eigenmodes at the right and left output ports of the dual-mode waveguide. By taking the absolute value squared of these coefficients, the optical power coupled to each mode is calculated, which we then normalized by the input power P_{in}. In this way, we define the following coupling efficiencies η_{TE0}, η_{TE1} and $\eta_{\text{TE0,r}}$ which are the coupling efficiency to the TE0 and TE1 modes of the dual-mode and the TE0 mode of the dual-mode waveguide in the counter-propagating direction, respectively. Ideally, if there are no reflections in the structure, this efficiency should be negligible. Finally, we define the ratio $\xi = \eta_{\text{TE0}}/\eta_{\text{TE1}}$ as the laser extinction. As can be seen in Fig. 5.8(a), the laser extinction expected for such a structure is modest, and $\eta_{\text{TE0,r}}$ is far from being negligible, which highlights sources of reflections in the structure.

To compare, we reproduce the same simulation but with a structure with no tether, neither on the dual-mode waveguide nor on the single-mode. The result of this simulation is shown in Fig. 5.8(b). Here we clearly see an inhibited η_{TE0} and hence low ξ. Moreover, as expected in the absence of reflective and scattering elements, $\eta_{\text{TE0,r}}$ is strongly suppressed. To understand the most detrimental type of tether to the performance of the device, we perform two additional simulations, one including the tethers on the dual-mode waveguide (Fig. 5.8(b)) and one solely including the middle tether on the single-mode waveguide (Fig. 5.8(d)). The comparison between the two measurements demonstrates that the most detrimental effect of the laser extinction in the TE0 mode arises from the presence of the tether on the dual-mode waveguide. We suspect that the asymmetry of the tethers, meaning that they are only located on one side of the waveguide, introduces the possible scattering from the TE1 to TE0 mode in the dual-mode waveguide. If implemented in a controlled way, asymmetries can be used to convert the TE1 mode to TE0 mode (Chen et al. 2015), but here it is, of course, not a desirable effect. The main effect of the middle tether is then to introduce reflection/scattering back to the left port of the dual-mode waveguide. Again, converting back to a geometry presented in (Papon et al. 2019) can alleviate this effect. Moreover, the development of suspension tethers made of polymer can reduce scattering losses (Uğurlu 2021).

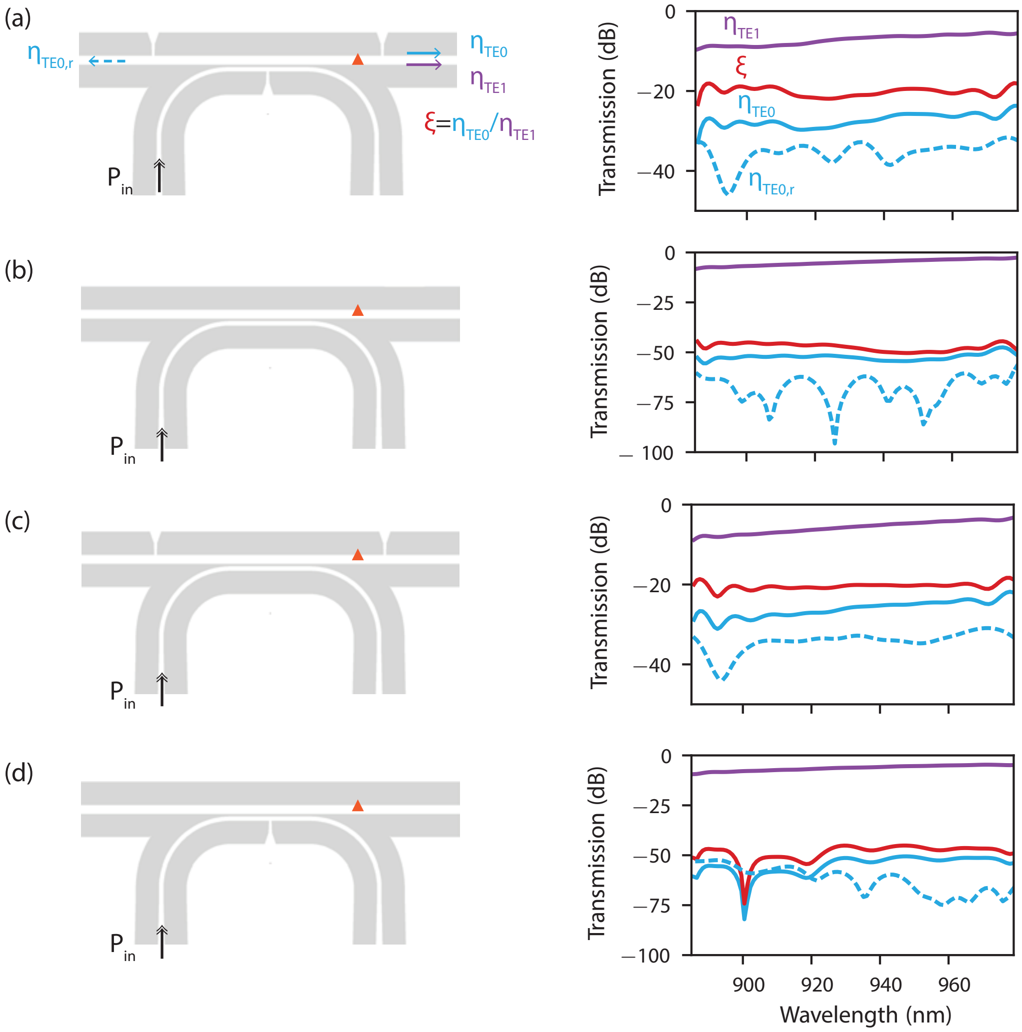

FIGURE 5.8: Three-dimensional FDTD simulations for different configurations of the ADC. For each configuration, as fabricated (a), without any tether (b), with tethers on the dual-mode waveguide (c), and with the middle tether on the single-mode waveguide (d), the indicated transmission efficiencies are calculated.

Throughout this chapter, we introduced a novel device based on ADC for performing in-plane resonant excitation of QDs embedded in a dual-mode waveguide. We demonstrated large laser suppression that enabled to perform pulsed resonant excitation with a large SNR. This led to the measurement of $g^{(2)}(0) < 7\%$, which could be further reduced by improving the fabrication and design of the structure. We gave an explanation for the limited visibility of the HOM interference and also strived to explain how the current design limits the laser suppression. We can, however, confidently confirm that such a device represents a source of dual-rail encoded photons. Usually, uni-directionality of the emission is preferred for boosting the source efficiency, which could be implemented by adding a mirror similar to the photonic crystal filter shown in Chapter. 4. We can, however, instead think of integrating several ADC-based sources on the same chip and connecting both outputs of the dual-mode waveguides to a circuit of linear optics elements performing an operation on the input dual-rail encoded quantum states. In the last section, we will give an example of such an application.

5.3 Applications: towards on-chip heralded two-photon entanglement

As introduced in the introduction of this thesis, single photons are favorable for carrying quantum information and can be used as logical qubits to perform quantum information operations. The computational basis is defined by two logical qubits

$$\begin{aligned} |0\rangle_L &= \hat{a}_1^\dagger |0,0\rangle_{1,2} = |1,0\rangle_{1,2} \\ |1\rangle_L &= \hat{a}_2^\dagger |0,0\rangle_{1,2} = |0,1\rangle_{1,2} \,, \end{aligned} \tag{5.6}$$

where $\hat{a}_j$ is the creation operator applied to mode $j = 1, 2$, corresponding to the degree of freedom of the single photons chosen for encoding the quantum information. When the creation operator is applied to the vacuum state of the Fock state basis, the system is changed according to $\hat{a}^\dagger |n\rangle = \sqrt{n+1}\,|n+1\rangle$ (Knight et al. 2005).

A physical qubit can then be described by the logical qubits as the general state

$$|\psi\rangle = \cos(\theta/2)\,|0\rangle_L + e^{i\phi}\sin(\theta/2)\,|1\rangle_L \,. \tag{5.7}$$

In geometrical representation, the qubit is described by a position on the surface of a sphere of radius 1, called the Bloch sphere. Qubit rotation is performed by changing the polar and azimuthal angles θ and ϕ. A largely exploited degree of freedom has been the polarization basis, where logical qubits can be encoded in the horizontal and vertical polarization of the photons. Rotation of the qubit can then be performed with a half-wave plate.

To make use of the maturity of the photonic integrated circuitry, it is in the best interest to transfer qubits operation directly on-chip. Polarization control in a photonic waveguide is possible (Crespi et al. 2011) but challenging. Instead, path-encoding, or dual-rail encoding, is more favorable since waveguide modes are easily defined by fabrication. On this basis, the logical qubits are defined as the presence of the photon in one waveguide or the other (Bergamasco et al. 2017), as shown in Fig. 5.9. The rotation of the qubit is done with $50:50$ directional couplers (DC), the transfer matrix relating the input mode operators $\hat{a}_0^\dagger$, $\hat{a}_1^\dagger$ to the output modes $\hat{a'}_0^\dagger$, $\hat{a'}_1^\dagger$ is shown, where $\hat{a}_j^\dagger$ denotes the creation operator acting on the mode $j=0$ for the top waveguide (dashed line) and $j=1$ for the bottom waveguide (solid line). We observe a different transformation matrix than for the polarization-encoded case, which can be accounted for by performing a $\pi/2$-phase shift on the a_1 and a_1' waveguide modes. This difference is due to the working principle of the directional coupler, which results in the two output waveguide modes being $\pi/2$ out-of-phase (Chrostowski et al. 2015).

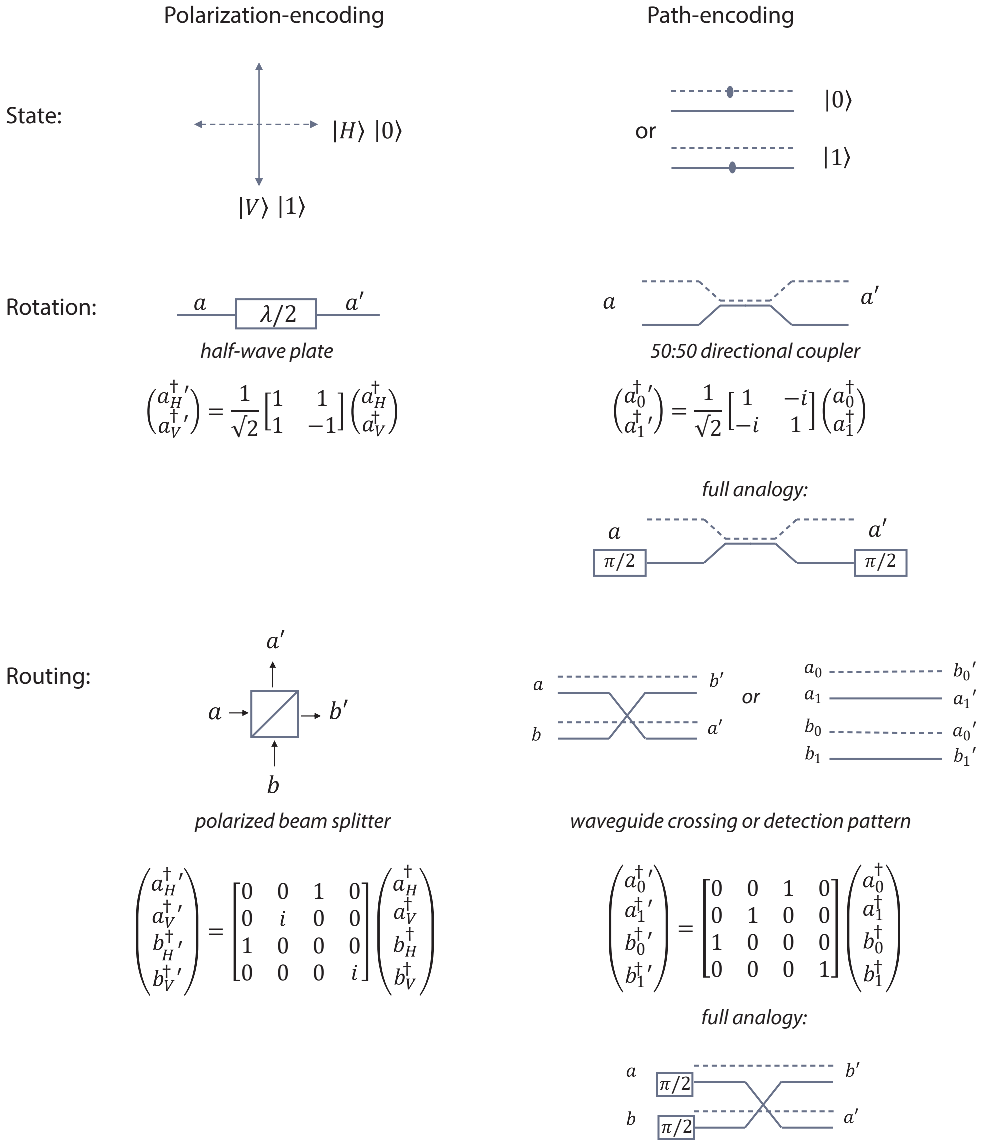

FIGURE 5.9: Equivalence between the polarization-endoded basis and the path-encoded basis. The state description in these two bases is shown together with common single-qubit operations.

Finally, the equivalent to routing conditioned on the polarization of the photons is executed in path-encoding with re-routing of the waveguides. However, this implies that waveguide-crossing may occur, which is not desirable for on-chip operation since this may add crosstalk between the modes. Instead, re-arranging the ordering of waveguide mode and changing the detection pattern accordingly leads to the same effect.

With this overview of the path-encoded basis, we can now convert any circuit designed in the polarization-encoded basis to an equivalent integrated circuit. An interesting case is the two-photon heralded entanglement gate (Zhang et al. 2008), shown in Fig. 5.10(a), realized in the polarization basis with free-space optics. This gate relies on $N = 4$ polarization-encoded single photons sent to a network of $22.5°$ half-wave plate and polarized beamsplitter at ports A, B, C, and D. At the end of the gate, 4-fold coincidence at each output (A', B'', C'' and D') only occurs due to the contribution of the state $|\psi_{A'B''C''D'}\rangle = \frac{1}{4}(\Phi^+_{A'D'}\Psi^+_{B''C''} - \Psi^+_{A'D'}\Phi^+_{B''C''})$, where $\Psi^{\pm}_{AD} = \frac{1}{\sqrt{2}}(|H\rangle_A |V\rangle_D \pm |V\rangle_A |H\rangle_D)$ and $\Phi^{\pm}_{AD} = \frac{1}{\sqrt{2}}(|H\rangle_A |H\rangle_D \pm |V\rangle_A |V\rangle_D)$ are the maximally entangled Bell States. By measuring the right states in modes B'' and C'', it is then possible to herald an entangled state in modes A' and D'. This experiment has been realized by outcoupling the single photons emitted from a single quantum dot and demultiplexing the photon stream to generate $N = 4$ temporally-matched photons (Hummel 2019; Mikkelsen 2021). Generating two-photon entangled states with high heralding efficiency can be used in device-independent quantum key distribution protocols.

The equivalent path-encoded circuit is shown in Fig. 5.10(b), where corresponding parts are shadowed in yellow and green. Single photons are coupled to 4 waveguides, assigned to mode $\hat{a_0}^\dagger$, $\hat{b_0}^\dagger$, $\hat{c_0}^\dagger$ and $\hat{d_0}^\dagger$. A $50:50$ directional coupler transforms the mode $\hat{j_0}^\dagger$ intro a superposition of $\hat{j_0}^\dagger$ and $\hat{j_1}^\dagger$, where j stands for a, b, c, d. The modes are then re-assigned to perform the waveguide crossing. The set of modes a'_0, a'_1 and d'_0, d'_1 represents two qubits Q1 and Q2 onto which an entangled state is heralded. The central part of the circuit performed a nested interferometer, and coincidence counts between detectors $D1$ and $D2$ herald an entangled state. Phase shifters are added for real-life applications. The presence of this interferometer for the path-encoded basis shows that integrated circuits are more suited for dual-rail encoding since the phase relation is more stable on-chip than off-chip. The unitary operations transforming the mode operators are indicated as inset. Given the input mode operators, the output

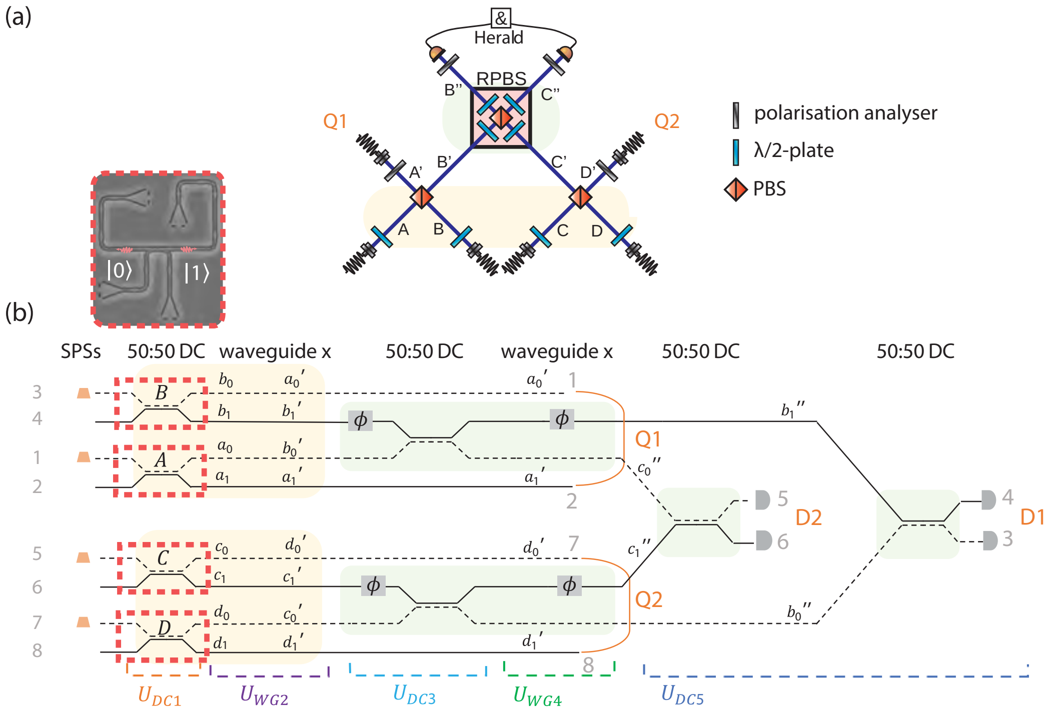

FIGURE 5.10: Heralded-entanglement gate in (a) the polarization-encoded basis and (b) the path-encoded basis. The first unitary U_{DC1} can be replaced in future experiments by $N = 4$ integrated sources of dual-rail encoded qubits. The schematic in (a) is adapted from (Hummel 2019). RPBS: rotated polarized beamsplitter, $\lambda/2$: half-wave plate, DC: directional coupler.

operators can be obtained as

$$\begin{pmatrix} \hat{a}_0^{\prime\dagger} \\ \hat{a}_1^{\prime\dagger} \\ \hat{b}_0^{\prime\dagger} \\ \hat{b}_1^{\prime\dagger} \\ \hat{c}_0^{\prime\dagger} \\ \hat{c}_1^{\prime\dagger} \\ \hat{d}_0^{\prime\dagger} \\ \hat{d}_1^{\prime\dagger} \end{pmatrix} = \underbrace{\frac{1}{2\sqrt{2}} \begin{bmatrix} 0 & 0 & 2 & -2i & 0 & 0 & 0 & 0 \\ -2i & 2 & 0 & 0 & 0 & 0 & 0 & 0 \\ -1 & i & -1 & -i & -1 & -i & 1 & -i \\ -i & -1 & -i & 1 & i & -1 & -i & -1 \\ 1 & -i & -1 & -i & -1 & -i & -1 & i \\ -i & -1 & i & -1 & -i & 1 & -i & -1 \\ 0 & 0 & 0 & 0 & 2 & -2i & 0 & 0 \\ 0 & 0 & 0 & 0 & 0 & 0 & -2i & 2 \end{bmatrix}}_{U_{\mathrm{total}}} \begin{pmatrix} \hat{a}_0^{\dagger} \\ \hat{a}_1^{\dagger} \\ \hat{b}_0^{\dagger} \\ \hat{b}_1^{\dagger} \\ \hat{c}_0^{\dagger} \\ \hat{c}_1^{\dagger} \\ \hat{d}_0^{\dagger} \\ \hat{d}_1^{\dagger} \end{pmatrix}, \tag{5.8}$$

where

$$U_{\mathrm{total}} = U_{\mathrm{DC5}}\, U_{\mathrm{WG4}}\, U_{\mathrm{DC3}}\, U_{\mathrm{WG2}}\, U_{\mathrm{DC1}}. \tag{5.9}$$

The full description of the individual matrices is shown in Appendix B. This unitary does not contain the individual phase shifters, but they can be easily included by an identity matrix including $e^{i\phi}$-terms in the diagonal. In Fig. 5.10(b), we marked each input and output mode by its order of appearance in the input and output vectors in Eq. 5.8. The four initials $50:50$ DC operations can be replaced by $N = 4$ ADC-based sources, introduced in the previous section, thereby decreasing the number of components of such a circuit in future experiments.

The distribution of indistinguishable single photons through a circuit described by the unitary U_{total} is calculated from all the possible photon distribution at the output modes given input of mode occupation, which is described in Ref. (Tichy 2014) as

$$P(\vec{r}, \vec{s}; U) = \frac{\prod_j s_j!}{\prod_j r_j!} \left| \sum_{\sigma \in S_{\vec{d}(\vec{s})}} \prod_{j=1}^{N} U_{d_j(\vec{r}),\sigma(j)} \right|^2 , \tag{5.10}$$

which gives the transition probability between an input state $\vec{r}$ and an output state $\vec{s}$. Here $\vec{r}$ ($\vec{s}$) stands for the mode occupation list, for example $[10101010]$, which means 1 photon in mode 1, 0 in mode 2, etc. The equivalent mode assignment $d(\vec{r})$ is then $[1\ 3\ 5\ 7]$, showing to which modes the 4 photons are assigned to. The sampling to the different output combinations is done by summing over $\sigma \in S_{\vec{d}(\vec{s})}$ which runs over all the output mode assignment $\vec{d}(\vec{s})$ given a $N \times N$ unitary matrix. For four photons, the probability distribution can still be calculated numerically.

With the goal of fabricating such a chip, we investigate the effect of imperfect $50 : 50$ DC on the 4-fold coincidences probability since this detection event ensures the generation of an entangled state. To do so, we recall the general transformation matrix of a DC, reading

$$U_{\text{DC}} = \begin{bmatrix} t & -ir \\ -ir & t \end{bmatrix} , \tag{5.11}$$

where $t = \cos\left(\frac{k\pi}{2}\right)$ and $t = \sin\left(\frac{k\pi}{2}\right)$, with $k = x/L_t$, x the length of the DC and L_t the length for which all the power is transferred to the other arm. Naturally, for $k = 0.5$ we have a perfect $50 : 50$ DC. In Fig.5.11(a) and (b), we show the 4-fold coincidences for particular detection pattern, $[3\ 6]$ and $[4\ 5]$ respectively, after the evolution through matrix U_{total} for an input mode assignment $[1\ 3\ 5\ 7]$, calculated from Eq. 5.10.

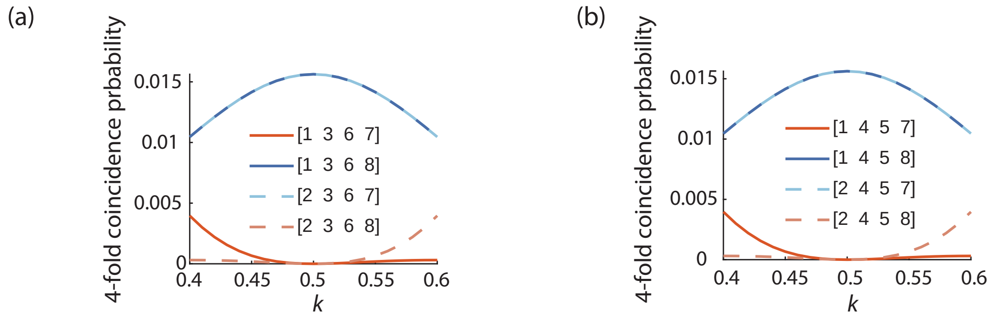

FIGURE 5.11: Four-fold coincidences after the evolution through U_{total} for an input mode assignment $[1\ 3\ 5\ 7]$, with herald on output (a) $[3\ 6]$ and (b) $[4\ 5]$, as a function of the directional coupler splitting ratio.

Given the assigned parity of each port (0 or 1), it seems that detection on output ports $[3\ 6]$ heralds the state Ψ^{+}. From these calculations, we extract $\rho^{[b\ c]}_{\Psi^{+}_{Q1,Q2}}$, the probability of detecting $\Psi^{+}_{Q1,Q2}$ combined with herald (b, c), which is highest for perfect DCs. We get $\rho^{[3\ 6]}_{\Psi^+_{Q1,Q2}} = 1/32$, $\rho^{[4\ 5]}_{\Psi^+_{Q1,Q2}} = 1/32$ and $\rho^{[3\ 6,4\ 5]}_{\Psi^+_{Q1,Q2}} = 1/16$.

We are now interested in quantifying the heralding probability, meaning the probability of heralding Ψ^+ between $Q1$ and $Q2$ given that we detect coincidences on $[3\ 6]$ or $[4\ 5]$. For this calculation, we assume that we have number-resolving detectors, meaning that we can discard detection events with more than 1 photon at each heralding detector and that we have enough detectors to measure on all output ports. The first assumption is very strong since it can only be realized with our detectors by performing a HBT measurement before the herald, adding two extra detectors requirement per heralding mode, or employing transition-edge sensors. We, however, go on with it since we want to see the impact of imperfect DC in the best-case scenario. The heralding probability is defined here as

$$P_s = \frac{\rho^{[b\ c]}_{\Psi^+_{Q1,Q2}}}{\rho^{[b\ c]}_{\Psi^+_{Q1,Q2}} + \rho^{[b\ c]}_{\epsilon}}, \tag{5.12}$$

where (b, c) stands for the heralding patterns considered, either $[3\ 6]$, $[4\ 5]$ or $[3\ 6]$ and $[4\ 5]$. All detection events at the herald that do not contribute to the generation of $\Psi^+_{Q1,Q2}$ are contained in $\rho^{[b\ c]}_{\epsilon}$. In Fig. 5.12, we show the calculated heralding probability for the different heralding schemes. As anticipated, having the possibility of detecting at the 4 output modes of the heralding station ensures a high heralding probability. We show as the vertical dashed lines the expected fabrication error, and if all DC undergo the same systematic error, the effect on the heralding probability is low. Here we neglect random variations, which are expected to be more detrimental.

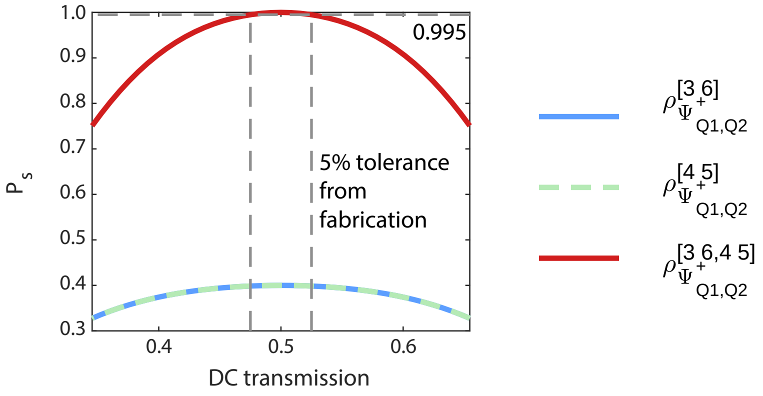

FIGURE 5.12: Probability of successfully heralding Ψ^+ on $Q1$ and $Q2$ as a function of the transmission of the directional couplers. Different heralding patterns are shown depending on the number of detectors available.

Finally, we would like to calculate the projective measurements on one output of $Q1$, one output of $Q2$, and the outputs $[3\ 6]$ at the heralding station to record the correlation between the coincidences in a Bell test fashion (Bell 1964). To do so, we add two tunable directional couplers before detection

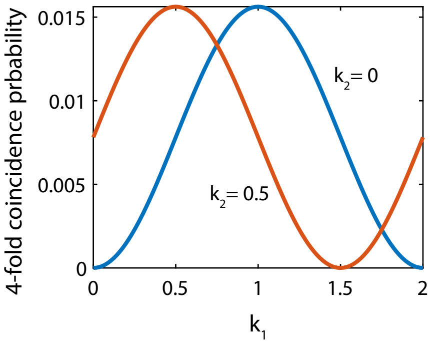

FIGURE 5.13: Four-fold coincidence probability on outputs $[1\ 7\ 3\ 6]$, calculated from projective measurements on the qubit outputs performed by varying the splitting ratio of tunable directional couplers.

at $Q1$ and $Q2$, defined by arbitrary transmission and reflection coefficients t_1, r_1 and t_2, r_2, respectively. In practice, $t = \cos(k\pi/2)$ and $r = \sin(k\pi/2)$ can be controlled by changing the waveguide gap distance (Papon et al. 2019) or with two DCs and a phase shifter forming a MZI interferometer (Wang et al. 2014). The proposed layout to accommodate the additional tunable directional couplers is shown in Appendix B. In Fig. 5.13, we show the probability of coincidence counts in $[1\ 7]$ conditioned on the detection at $[3\ 6]$, for $k_2 = 0$ (blue curve) and $k_2 = 0.5$ (red curve) as k_1 is swept from $0 \to 2$. We clearly observe a joint sine distribution, which is characteristic of the correlations of a Bell state (Fox 2006).

This section focused on proposing a design of an on-chip circuit generating two-photon heralded entangled states. This work was done in collaboration with Dr. Fabian Ruf at Aarhus University, who prepared the actual design compatible with the SiN chips from the foundry Lionix. The experimental characterization will be shown in a follow-up work.

◆

Throughout this chapter, we demonstrated a novel nanophotonic structure based on asymmetric directional couplers for resonantly exciting quantum dots embedded in a dual-mode waveguide. We demonstrated the asset of the bi-directionality of single-photon emission for defining on-chip dual-rail encoded qubits. This was proven by measuring the second-order correlation function between the two output modes of the source with $g^{(2)}(0) < 7\%$ at π-pulse excitation. We touched upon the design limitations of the current device and suggested a direct way to improve it. This naturally led us to present an application for multiple dual-rail encoded sources, which can be used for generating two-photon heralded entanglement with $N = 4$ sources. After characterizing the effect of systematic DC errors, the chip was fabricated and will be used with a demultiplexed source in the first place. Future experiments will focus on harvesting the scalability offered by integrated multi-QD sources.

6 Conclusions and Outlook

6.1 In summary

Throughout this thesis, we ought to experimentally demonstrate the strategy to control multiple quantum dots in photonic integrated circuits, a requirement for the scalable operation of N deterministic single-photon sources. To do so, we first introduced the nanofabrication methods of quantum photonic circuits and covered one of the main challenges for designing a scalable photonic platform, which is efficiency. Many aspects of the quantum photonic circuit contribute to efficiency, one of which is the propagation loss in the nanobeam waveguides. The lowest propagation loss we measured for the GaAs platform was 5.6 ± 0.4 dB/mm, and we report the typical value of 7 dB/mm. We investigated different methods to diminish the losses, such as multi-pass exposure and surface treatments with atomic layer deposition. Still, none of them led to a decrease in propagation loss, originating from the waveguide sidewall roughness. Although we did not improve the transmission efficiency through the nanobeam waveguides, we provided a benchmark to compare the propagation loss through doped waveguides (Wang et al. 2021) and integrated waveguides on silicon substrate (Shadmani et al. 2022).

Another aspect of the photonic integrated circuit we addressed is the outcoupling efficiency from the waveguide to an optical fiber. Shallow-etched gratings are commonly used in the planar quantum photonic platform to scatter light off-chip, and coupling efficiency $> 60\%$ was previously reported (Zhou et al. 2018). During our studies, the outcoupling efficiency was further boosted by implementing distributed Bragg reflectors below the sacrificial layer, such that efficiency up to 80% was measured. This enhanced outcoupling performance contributed to the forecast of a fiber-coupled single-photon source with 78% efficiency (Uppu et al. 2020b).

Efficiency is a generic consideration for the development of scalable quantum photonic circuits. On top of it, to address multiple quantum dots, we needed to enrich the nanophotonic toolbox by designing and implementing novel elements. Therefore, we implemented polarization diversity gratings to the GaAs platform to distribute an excitation laser to two waveguides. We demonstrated an extinction ratio between the transmission through two waveguides coupled to the polarization grating of $|ER| > 20$ dB. We used this two-dimensional coupler to address two waveguide-integrated single-photon sources simultaneously. Moreover, individual shallow-etched trenches implemented on each source allowed us to apply a bias voltage through the diode of each waveguide individually.

After designing such a nanophotonic device, we demonstrated, for the first time, the simultaneous resonant excitation of two quantum dots embedded in two independent waveguide-based sources (Papon et al. 2022). We brought two quantum dots into mutual resonance using individual Stark tuning and verified the single-photon character of their emission by measuring the second-order correlation function in continuous-wave excitation. We extract values of $g^{(2)}(0) = 0.13 \pm 0.02$ and $g^{(2)}(0) = 0.04 \pm 0.015$ for two quantum dots, limited by the laser suppression provided by the nanophotonic structure. We measured two-photon quantum interference between two quantum dots by bringing them in resonance, with a peak visibility of $V = (79 \pm 2)\%$, limited by the imperfect residual laser photon extinction. From the temporal width of the visibility curve, we find indications that the effect of spectral diffusion experienced by each quantum dot is not as detrimental as anticipated. It is likely due to the correlation in the electrical noise reaching each quantum dot. Improvements in the setup of transmission lines will potentially remove the source of electrical noise altogether.

The fabrication disorder was limiting the performance of the developed $N = 2$ single-photon source by the laser suppression through the photonic crystal filter. This prohibited performing the pulsed resonant excitation of two quantum dots with a sufficient signal-to-noise ratio. In turn, this drawback was a strong push towards developing waveguide sources based on asymmetric directional coupler (ADC) (Uğurlu 2021). We characterized this new nanophotonic device and measured a laser suppression $T_p < -40$ dB over a wavelength window of 2 nm. Moreover, we performed resonant pulsed excitation of a quantum dot in the dual-mode waveguide with a signal-to-noise ratio of 33 at π-pulse, a significant improvement compared to the previous attempt. The bi-directionality of the quantum dot emission can be seen as a built-in $50 : 50$ beamsplitter, which we use by collecting from the two output ports of the dual-mode waveguide. By recording coincidence counts as a function of time delay between the two output ports of the nanophotonic structure, we observed a second-order correlation function of $g^{(2)}(0) = (6.8 \pm 0.3)\%$ under pulsed excitation. This directly demonstrated the potential of the ADC for in-plane quantum photonic circuits with a dual-rail encoding of photonic qubits. In future experiments, four fabricated sources of dual-rail encoded photons can be used as the input of a circuit generating two-photon heralded entangled state through quantum interference.

6.2 Outlook

The central result of this thesis is the reported simultaneous resonant excitation and interference of two mutually resonant quantum dots employing a fully waveguide-based circuit. This represents a step towards operating multiple single-photon sources on the same chip. We highlighted the limitations of the current system and contributed to developing the next generation of quantum photonic circuits based on ADC for resonant excitation. Besides the suggestions for optimization that we already touched upon in Chapter 5, we would like to draft some salient features of this device.

First, most of the optical power used for excitation can be recycled for exciting following ADC-based waveguide sources. Indeed, as the simulation of Chapter 5 shows, the coupling efficiency between the TE0 mode of the single-mode waveguide and the TE1 mode of the dual-mode waveguide is approximately 30%, enough to apply a π-pulse to the quantum dot, where $> 70\%$ of the optical power remains in the single-mode waveguide. In the current device layout, the other end of the single-mode waveguide is connected to a shallow-etched grating, so the laser light is scattered out of the structure. This optical power can be instead recycled by appending a second ADC-based single-photon source and exciting another quantum dot within the same excitation pulse. This way, $N = 4$ single-photon sources could be operated simultaneously with a single laser "bus", as depicted in Fig. 6.1.

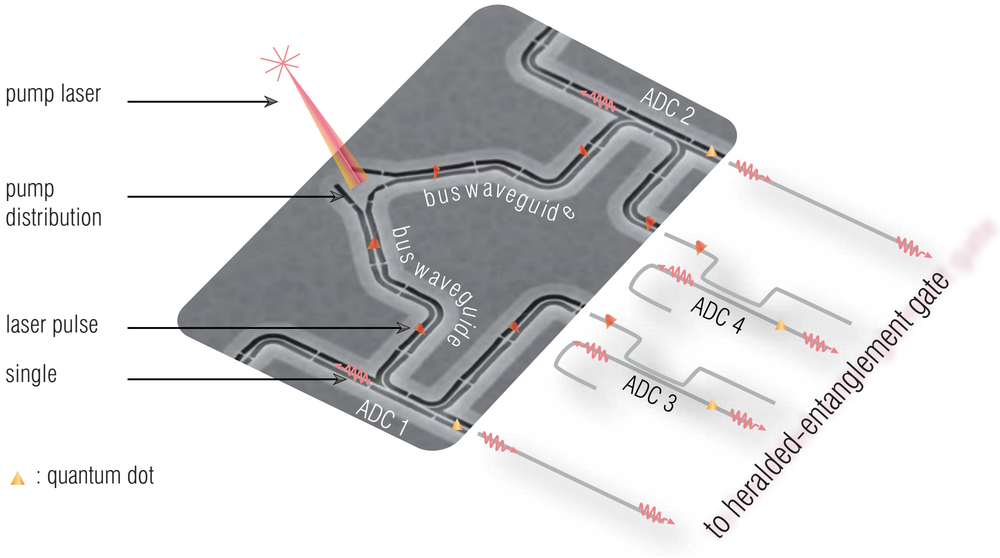

FIGURE 6.1: Illustration of the pump recycling concept for exciting $N = 4$ single-photon sources based on asymmetric directional couplers (ADC). After exciting two quantum dots through two ADCs, the remaining pump laser is guided toward two additional ADC-bases single-photon sources. A scanning electron microscope of a fabricated device for $N = 2$ is adapted for illustration purposes.

After interaction with the quantum dot, a similar power recycling argument holds for the optical power coupled to the TE1 mode of the dual-mode waveguide. In this case, a single-mode waveguide with a refractive index matched with the TE1 mode of the dual-mode waveguide could be used to couple laser photons out of the single-photon source area and take the role of filtering instead of the tapered waveguide. This could then either be connected yet to another ADC-based source (Chang et al. 2017) or dumped somewhere else on the chip, avoiding random scattering close to the quantum dot. In this way, the tapered waveguide region after the quantum dot area will only perform adiabatic transfer between a dual and single-mode waveguide but not take alone the role of filtering the laser power.

Tuning the gap distance between the waveguides of the asymmetric directional couplers allows one to modify the power transferred for exciting quantum dots. This control ensures that each cascaded ADC-based single-photon source can be operated at π-pulse. One can realize this by adding pairs of electrodes to the coupled waveguides and using electro-mechanical tuning to change the gap distance (Papon et al. 2019; Zhou et al. 2020). We expect that changing the gap distance would not deteriorate the laser suppression, as shown in the simulations of Chapter 5.

To alleviate the effect of pure dephasing through Purcell enhancement and to ensure a high single-photon generation rate, a higher $beta$ factor than the one provided by the dual-mode waveguide is desired. One can achieve this by appending a dual-mode photonic-crystal waveguide after the nanobeam waveguide (Zhou et al. 2022). This way, the ADC would prepare the TE1 mode to excite quantum dots in the photonic crystal waveguide with $\beta > 95\%$. For best source efficiency, unidirectionality of the single-photon emission is favored, which can be realized with the photonic crystal filter.

Given the current propagation loss of the GaAs quantum photonic platform, after scaling up the single-photon sources, it will still be favorable to couple the single photons out of the chip and perform quantum information processing on a low-loss programmable circuit (Sund et al. 2022). The increased number of single-photon sources will challenge the outcoupling method: in this case, coupling from the shallow-etched gratings to different free-space to fiber-coupler paths becomes cumbersome. A way to alleviate this issue is to perform chip-to-fiber array direct coupling with equally-spaced shallow-etched gratings or multi-core fiber coupling (Pita Ruiz et al. 2022). We also hope fiber coupling will diminish the specular reflection and scattering, contributing to photon impurity. Another way to explore is the hybrid integration of a quantum emitter platform to a low-loss processing chip through adiabatic tapering (Wan et al. 2020). The promising result of hybrid photonic circuits is the successful fabrication of the introduced GaAs waveguides on a silicon substrate (Shadmani et al. 2022).

In this thesis, we demonstrated that the operation of two deterministic single-photon sources is within reach, which could provide streams of indistinguishable photons at a high rate. Such a quantum device will find direct application within quantum communication, notably for loophole-free violation of Bell's inequality (González-Ruiz et al. 2022) and device-independent quantum key distribution, where local efficiency of the multi-photon source is critical (González-Ruiz et al. 2022). Indistinguishability is, of course, a fundamental property of the multi-photon source for quantum information protocols, which we could not measure in our multi-QD experiment. However, the indication that the linewidth broadening beyond the transform-limited value is not linked to fully uncorrelated noise gives a hopeful prospect of large mutual indistinguishability (Kambs et al. 2018). Moreover, the recent demonstration of coherent coupling between two InAs quantum dots emitted in the same waveguide mode (Tiranov et al. 2022), an effect also impacted by the indistinguishability of emitters, indicates that mutually indistinguishable multi-QD sources are realistic. Finally, the demonstration of $N = 2$ mutually resonant quantum dots from two different waveguides is the seed requirement for performing on-chip Bell state analyzer (Mahmoodian et al. 2016), a crucial element for building a quantum network.

According to the same method as presented in Fig. 3.8, we estimate that an optimized photonic circuit having large bandwidth of laser suppression would provide a likelihood of finding ≈ 15 quadruplets of quantum dots in different waveguides and ≈ 10 sextuplets. We assumed here similar quantum dot density and wavelength tuning range as presented in Chapter 4. However, increasing the latter would undoubtedly result in a higher probability of achieving fully-resonant multi single-photon sources. The prospect of scaling up to $N = 6$ waveguide-integrated single-photon sources is significant since such a scaled-up source represents the necessary hardware for generating heralded GHZ state. This way, the generation rate of such a small-scale entangled state can be boosted without using a $N = 6$-mode lossy demultiplexer. The latter is known to suffer transmission losses with the detection probability scaling as ρ^N, where ρ is the transmission efficiency per photon. Since GHZ states are useful for generating higher-dimensional cluster states through linear optics fusion gates (Gimeno-Segovia et al. 2015; Bombin et al. 2021), this has direct applications for measurement-based quantum computing. This percolated approach requires many ancillary photons, so a high-efficiency multi-photon source is needed for concrete quantum photonic simulators.

Finally, all the considerations above could be implemented for various solid-state quantum emitters. Among them are the GaAs quantum dots, which demonstrated high visibility between two remote GaAs QDs (Zhai et al. 2022). Or 'G-centers' in Silicon (Prabhu et al. 2022) providing optical transitions closer to the telecommunication band. These two quantum emitters present narrower inhomogeneous broadening than InAS quantum dots. This characteristic would play advantageously in developing a large number of mutually resonant single-photon sources. The present contribution advancing photonic circuits with multiple quantum emitters will resonate beyond the InAs quantum dot platform and will lead to further developments toward practical quantum information applications.

A Flow cryostat setup

The optical setup used for characterization in Chapter 3 is shown in A.1. We also provide a description of another method to measure the coupling to shallow-etched gratings (SEG). For other measurements presented in Chapter 3, supercontinuum laser source is used instead of the CTL. A continuous tunable laser (CTL) is coupled into the first shallow-etched grating through a microscope objective and the input power is controlled and monitored with a powermeter at the reflection port of beam splitter 1 (BS1). The diameter of the input beam is controlled with a beam expander in the excitation path so that it matches the optimal beam size for coupling into SEG. After propagation through the short nanobeam waveguide, light is scattered upwards by the second SEG, collected by the objective and transmitted to the collection path. The collected light is coupled into a zoom-fiber collimator (ZFC) whose focal length has been optimized as well to match the SEG beam size. The alignment to this structure is optimized by maximizing the power collected at the output fiber while changing the angle and position of the excitation and collection paths.

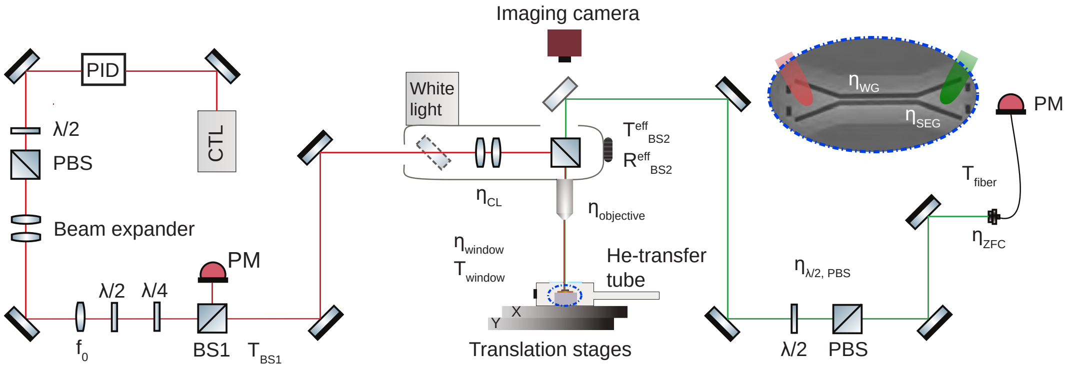

FIGURE A.1: Flow cryostat setup for measurement of the transmission of a CTL through two SEGs.

Assuming that the the SEGs are identical and neglecting the waveguide loss ($\eta_{\mathrm{wg}} \approx 1$), the transmission efficiency of a single grating is calculated as

$$\eta_{\mathrm{SEG}} = \sqrt{\frac{P_{\mathrm{SEG}}}{P_{\mathrm{R,BS1}} \cdot \frac{T_{\mathrm{BS1}}}{R_{\mathrm{BS1}}} \cdot \eta_{\mathrm{CL}} \cdot R^{\mathrm{eff}}_{\mathrm{BS2}} \cdot \eta^2_{\mathrm{objective}} \cdot \eta^2_{\mathrm{window}} \cdot T^4_{\mathrm{window}} \cdot T^{\mathrm{eff}}_{\mathrm{BS2}} \cdot \eta_{\lambda/2,\mathrm{PBS}} \cdot \eta_{\mathrm{ZFC}} \cdot T^2_{\mathrm{fiber}}}}, \tag{A.1}$$

where the different efficiencies are listed in Table 1.

Description	Efficiency	Comment
Transmission of BS1 T_{BS1}	$51.6\,\%$	Measured
Condenser lenses efficiency η_{CL}	$56.4\,\%$	Measured
Effective reflection of BS2 $R_{\text{BS2}}^{\text{eff}}$	$34.4\,\%$	Measured
Objective efficiency $\eta_{\text{objective}}$	$69.6\,\%$	Measured
Window efficiency η_{window}	$95\,\%$	From specs
Transmission at the window T_{window}	$96\,\%$	From Fresnel's eq.
Effective transmission of BS2 $T_{\text{BS2}}^{\text{eff}}$	$65.6\,\%$	$1 - R_{\text{BS2}}^{\text{eff}}$
Half-wave plate and PBS efficiency $\eta_{\lambda/2,\text{PBS}}$	$80.7\,\%$	Measured
Zoom fiber collimator efficiency η_{ZFC}	$88\,\%$	From specs
Transmission at the fiber T_{fiber}	$96\,\%$	From Fresnel's eq.

TABLE A.1: Setup efficiency of the flow cryostat. Note: this is not actual anymore since the optical setup has been rebuild.

B Heralded entanglement in path-encoded basis

In this Appendix, we show the proposed design for the two-photon heralded entanglement circuit with the tunable directional couplers added before detection on Qubit 1 and Qubit 2. In this way, we can perform joint projective measurement with all control on-chip, in the dual-rail encoded basis, without converting back to the polarization basis. We also show all the matrices needed to calculate the full transformation matrix U_{total}.

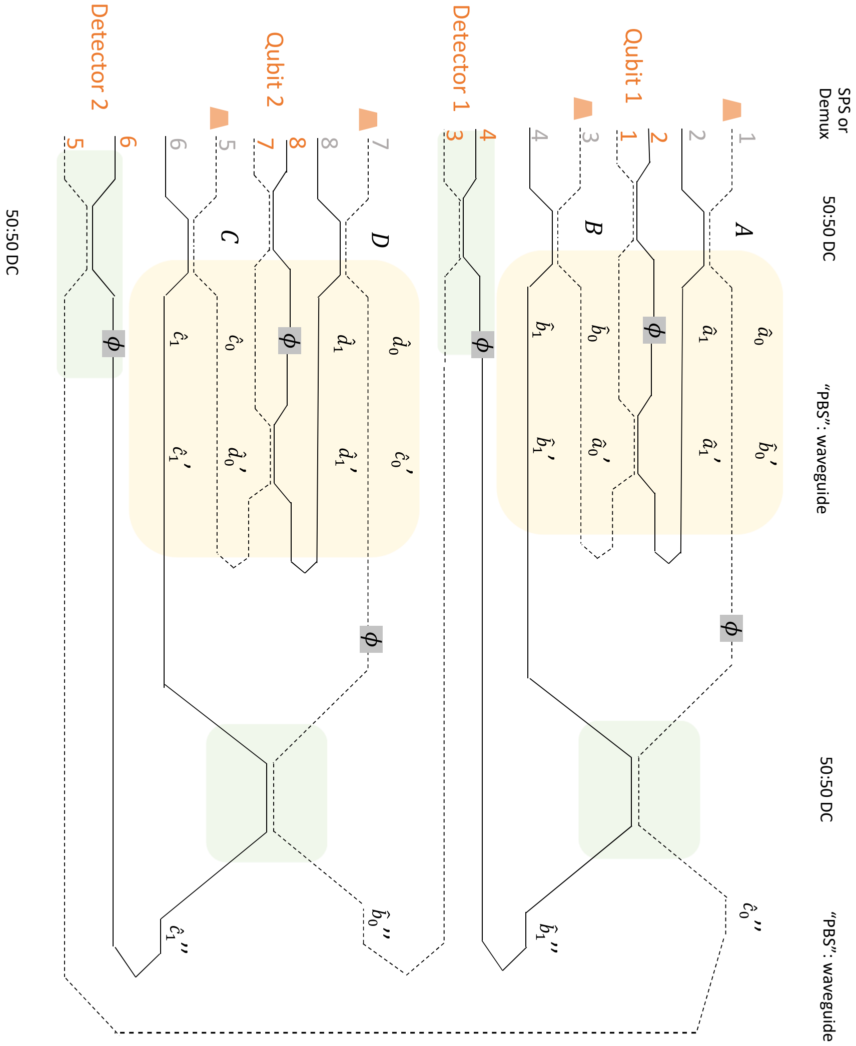

FIGURE B.1: Two-photon heralded entanglement gate with tunable directoinal couplers added before detection on $Q1$ and $Q2$ for joint projective measurements.

$$
\begin{gathered}
U_{DC1} = \frac{1}{\sqrt{2}} \begin{bmatrix} 1 & -i & 0 & 0 & 0 & 0 & 0 & 0 \\ -i & 1 & 0 & 0 & 0 & 0 & 0 & 0 \\ 0 & 0 & 1 & -i & 0 & 0 & 0 & 0 \\ 0 & 0 & -i & 1 & 0 & 0 & 0 & 0 \\ 0 & 0 & 0 & 0 & 1 & -i & 0 & 0 \\ 0 & 0 & 0 & 0 & -i & 1 & 0 & 0 \\ 0 & 0 & 0 & 0 & 0 & 0 & 1 & -i \\ 0 & 0 & 0 & 0 & 0 & 0 & -i & 1 \end{bmatrix} \\
U_{WG2} = \begin{bmatrix} 0 & 0 & 1 & 0 & 0 & 0 & 0 & 0 \\ 0 & 1 & 0 & 0 & 0 & 0 & 0 & 0 \\ 1 & 0 & 0 & 0 & 0 & 0 & 0 & 0 \\ 0 & 0 & 0 & 1 & 0 & 0 & 0 & 0 \\ 0 & 0 & 0 & 0 & 0 & 0 & 1 & 0 \\ 0 & 0 & 0 & 0 & 0 & 1 & 0 & 0 \\ 0 & 0 & 0 & 0 & 1 & 0 & 0 & 0 \\ 0 & 0 & 0 & 0 & 0 & 0 & 0 & 1 \end{bmatrix} \\
U_{DC3} = \frac{1}{\sqrt{2}} \begin{bmatrix} \sqrt{2} & 0 & 0 & 0 & 0 & 0 & 0 & 0 \\ 0 & \sqrt{2} & 0 & 0 & 0 & 0 & 0 & 0 \\ 0 & 0 & 1 & -i & 0 & 0 & 0 & 0 \\ 0 & 0 & -i & 1 & 0 & 0 & 0 & 0 \\ 0 & 0 & 0 & 0 & 1 & -i & 0 & 0 \\ 0 & 0 & 0 & 0 & -i & 1 & 0 & 0 \\ 0 & 0 & 0 & 0 & 0 & 0 & \sqrt{2} & 0 \\ 0 & 0 & 0 & 0 & 0 & 0 & 0 & \sqrt{2} \end{bmatrix} \\
U_{WG4} = \begin{bmatrix} 1 & 0 & 0 & 0 & 0 & 0 & 0 & 0 \\ 0 & 1 & 0 & 0 & 0 & 0 & 0 & 0 \\ 0 & 0 & 0 & 0 & 1 & 0 & 0 & 0 \\ 0 & 0 & 0 & 1 & 0 & 0 & 0 & 0 \\ 0 & 0 & 1 & 0 & 0 & 0 & 0 & 0 \\ 0 & 0 & 0 & 0 & 0 & 1 & 0 & 0 \\ 0 & 0 & 0 & 0 & 0 & 0 & 1 & 0 \\ 0 & 0 & 0 & 0 & 0 & 0 & 0 & 1 \end{bmatrix} \\
U_{DC5} = \frac{1}{\sqrt{2}2} \begin{bmatrix} \sqrt{2} & 0 & 0 & 0 & 0 & 0 & 0 & 0 \\ 0 & \sqrt{2} & 0 & 0 & 0 & 0 & 0 & 0 \\ 0 & 0 & 1 & -i & 0 & 0 & 0 & 0 \\ 0 & 0 & -i & 1 & 0 & 0 & 0 & 0 \\ 0 & 0 & 0 & 0 & 1 & -i & 0 & 0 \\ 0 & 0 & 0 & 0 & -i & 1 & 0 & 0 \\ 0 & 0 & 0 & 0 & 0 & 0 & \sqrt{2} & 0 \\ 0 & 0 & 0 & 0 & 0 & 0 & 0 & \sqrt{2} \end{bmatrix}
\end{gathered}
\tag{B.1}
$$

Bibliography

ACÍN, A., N. Brunner, N. Gisin, S. Massar, S. Pironio, and V. Scarani (2007). “Device-Independent Security of Quantum Cryptography against Collective Attacks”. *Phys. Rev. Lett.* **98** (23), 230501. DOI: `10.1103/PhysRevLett.98.230501` (cited on p. 2).

ACÍN, A. et al. (2018). “The quantum technologies roadmap: a European community view”. *New Journal of Physics* **20**.8, 080201. DOI: `10.1088/1367-2630/aad1ea` (cited on p. 1).

AHARONOVICH, I., D. Englund, and M. Toth (2016). “Solid-state single-photon emitters”. *Nature Photonics* **10**.10, 631–641. DOI: `10.1038/nphoton.2016.186` (cited on p. 2).

APPEL, M. H., A. Tiranov, S. Pabst, M. L. Chan, C. Starup, Y. Wang, L. Midolo, K. Tiurev, S. Scholz, A. D. Wieck, A. Ludwig, A. S. Sørensen, and P. Lodahl (2022). “Entangling a Hole Spin with a Time-Bin Photon: A Waveguide Approach for Quantum Dot Sources of Multiphoton Entanglement”. *Phys. Rev. Lett.* **128** (23), 233602. DOI: `10.1103/PhysRevLett.128.233602` (cited on p. 10).

ARAKAWA, Y. and M. J. Holmes (2020). “Progress in quantum-dot single photon sources for quantum information technologies: A broad spectrum overview”. *Applied Physics Reviews* 7.2, 021309. DOI: `10.1063/5.0010193` (cited on p. 5).

ARCARI, M., I. Söllner, A. Javadi, S. L. Hansen, S. Mahmoodian, J. Liu, H. Thyrrestrup, E. H. Lee, J. D. Song, S. Stobbe, and P. Lodahl (2014). “Near-unity coupling efficiency of a quantum emitter to a photonic crystal waveguide”. *Physical Review Letters* **113**, 093603 (cited on pp. 25, 27).

ARCARI, M. (2015). *Efficiency and coherence of quantum-dot single-photon sources: towards the ideal photon-emitter interface for photonic quantum networks*. PhD thesis, University of Copenhagen (cited on p. 66).

ASPECT, A., J. Dalibard, and G. Roger (1982). “Experimental Test of Bell’s Inequalities Using Time-Varying Analyzers”. *Phys. Rev. Lett.* **49** (25), 1804–1807. DOI: `10.1103/PhysRevLett.49.1804` (cited on p. 5).

BACA, A. G. and C. I. H. Ashby (2005). *Fabrication of GaAs devices*. The Institution of Electrical Engineers (cited on p. 41).

BART, N. et al. (2022). "Wafer-scale epitaxial modulation of quantum dot density". *Nature Communications* **13**.1, 1633. DOI: `10.1038/s41467-022-29116-8` (cited on pp. 7, 53).

BARTOLUCCI, S., P. Birchall, H. Bombin, H. Cable, C. Dawson, M. Gimeno-Segovia, E. Johnston, K. Kieling, N. Nickerson, M. Pant, F. Pastawski, T. Rudolph, and C. Sparrow (2021). *Fusion-based quantum computation*. DOI: `10.48550/ARXIV.2101.09310` (cited on p. 42).

BELL, J. S. (1964). "On the Einstein Podolsky Rosen paradox". *Physics Physique Fizika* **1** (3), 195–200. DOI: `10.1103/PhysicsPhysiqueFizika.1.195` (cited on p. 94).

BENEVIDES, R., M. Ménard, G. S. Wiederhecker, and T. P. M. Alegre (2020). "Ar/Cl2 etching of GaAs optomechanical microdisks fabricated with positive electroresist". *Opt. Mater. Express* **10**.1, 57–67. DOI: `10.1364/OME.10.000057` (cited on p. 44).

BENNETT, C. H. (1984). "Quantum cryptography: Public key distribution and coin tossing". *IEEE Int. Conf. on Computers, Systems and Signal Processing* (cited on p. 2).

BERA, A., Y. Marin, M. Harjanne, M. Cherchi, and T. Aalto (2022). "Ultra-low loss waveguide platform in silicon photonics". *Silicon Photonics XVII*. Ed. by G. T. **REED** and A. P. Knights. Vol. 12006. International Society for Optics and Photonics. SPIE, 1200603. DOI: `10.1117/12.2610022` (cited on p. 42).

BERGAMASCO, N., M. Menotti, J. E. Sipe, and M. Liscidini (2017). "Generation of Path-Encoded Greenberger-Horne-Zeilinger States". *Phys. Rev. Applied* **8** (5), 054014. DOI: `10.1103/PhysRevApplied.8.054014` (cited on p. 90).

BOMBIN, H., I. H. Kim, D. Litinski, N. Nickerson, M. Pant, F. Pastawski, S. Roberts, and T. Rudolph (2021). *Interleaving: Modular architectures for fault-tolerant photonic quantum computing*. DOI: `10.48550/ARXIV.2103.08612` (cited on p. 101).

BORREGAARD, J., H. Pichler, T. Schröder, M. D. Lukin, P. Lodahl, and A. S. Sørensen (2020). "One-Way Quantum Repeater Based on Near-Deterministic Photon-Emitter Interfaces". *Phys. Rev. X* **10** (2), 021071. DOI: `10.1103/PhysRevX.10.021071` (cited on p. 2).

BRIEGEL, H.-J., W. Dür, J. I. Cirac, and P. Zoller (1998). "Quantum Repeaters: The Role of Imperfect Local Operations in Quantum Communication". *Phys. Rev. Lett.* **81** (26), 5932–5935. DOI: `10.1103/PhysRevLett.81.5932` (cited on p. 2).

BROWN, R. H. and R. Q. Twiss (1956). "Correlation between Photons in two Coherent Beams of Light". *Nature* **177**.4497, 27–29. DOI: `10.1038/177027a0` (cited on p. 16).

BUTERAKOS, D., E. Barnes, and S. E. Economou (2017). "Deterministic Generation of All-Photonic Quantum Repeaters from Solid-State Emitters". *Phys. Rev. X* **7** (4), 041023. DOI: `10.1103/PhysRevX.7.041023` (cited on p. 2).

CAROLAN, J. et al. (2015). "Universal linear optics". *Science* **349**.6249, 711–716 (cited on p. 2).

CHANG, Y.-C., S. P. Roberts, B. Stern, and M. Lipson (2017). *Resonance-Free Light Recycling*. DOI: `10.48550/ARXIV.1710.02891` (cited on p. 99).

CHEN, D., X. Xiao, L. Wang, Y. Yu, W. Liu, and Q. Yang (2015). "Low-loss and fabrication tolerant silicon mode-order converters based on novel compact tapers". *Opt. Express* **23**.9, 11152–11159. DOI: `10.1364/OE.23.011152` (cited on p. 88).

CHOW, J., E. Greplová, F. Heijman, C. Kuchkovsky, D. O'Halloran, J. Pointing, G. Shutko, and C. J. Williams (2022). *State of quantum computing: builiding a quantum economy*. World Economic Forum, insight report (cited on p. 1).

CHROSTOWSKI, L. and M. Hochberg (2015). *Silicon photonics design: from devices to systems*. Cambridge University Press (cited on p. 90).

CHU, X.-L., T. Pregnolato, R. Schott, A. D. Wieck, A. Ludwig, N. Rotenberg, and P. Lodahl (2020). "Lifetimes and Quantum Efficiencies of Quantum Dots Deterministically Positioned in Photonic-Crystal Waveguides". *Advanced Quantum Technologies* **3**.11, 2000026. DOI: `https://doi.org/10.1002/qute.202000026` (cited on p. 53).

COLES, R. J., D. M. Price, J. E. Dixon, B. Royall, E. Clarke, P. Kok, M. S. Skolnick, A. M. Fox, and M. N. Makhonin (2016). "Chirality of nanophotonic waveguide with embedded quantum emitter for unidirectional spin transfer". *Nature Communications* **7**.1, 11183. DOI: `10.1038/ncomms11183` (cited on p. 79).

CRESPI, A., R. Ramponi, R. Osellame, L. Sansoni, I. Bongioanni, F. Sciarrino, G. Vallone, and P. Mataloni (2011). "Integrated photonic quantum gates for polarization qubits". *Nature Communications* **2**.1, 566. DOI: `10.1038/ncomms1570` (cited on p. 89).

DAVANÇO, M., C. S. Hellberg, S. Ates, A. Badolato, and K. Srinivasan (2014). "Multiple time scale blinking in InAs quantum dot single-photon sources". *Phys. Rev. B* **89** (16), 161303. DOI: `10.1103/PhysRevB.89.161303` (cited on p. 68).

DAVEAU, R. S. (2016). *Efficient fiber-coupled single-photon sources based on quantum dots*. PhD thesis, University of Copenhagen (cited on p. 28).

DAVEAU, R. S., K. C. Balram, T. Pregnolato, J. Liu, E. H. Lee, J. D. Song, V. Verma, R. Mirin, S. W. Nam, L. Midolo, S. Stobbe, K. Srinivasan, and P. Lodahl (2017). "Efficient fiber-coupled single-photon source based on quantum dots in a photonic-crystal waveguide". *Optica* **4**.2, 178–184. DOI: `10.1364/OPTICA.4.000178` (cited on p. 45).

DING, Y., J. Xu, F. D. Ros, B. Huang, H. Ou, and C. Peucheret (2013). "On-chip two-mode division multiplexing using tapered directional coupler-based mode multiplexer and demultiplexer". *Opt. Express* **21**.8, 10376–10382. DOI: `10.1364/OE.21.010376` (cited on p. 76).

DIVINCENZO, D. P. (2000). "The physical implementation of quantum computation". *Fortschritte der Physik* **48**.9-11, 771–783 (cited on p. 1).

DONG, P., W. Qian, S. Liao, H. Liang, C.-C. Kung, N.-N. Feng, R. Shafiiha, J. Fong, D. Feng, A. V. Krishnamoorthy, and M. Asghari (2010). "Low loss shallow-ridge silicon waveguides". *Opt. Express* **18**.14, 14474–14479. DOI: `10.1364/OE.18.014474` (cited on p. 42).

DREESSEN, C. L., C Ouellet-Plamondon, P Tighineanu, X Zhou, L Midolo, A. S. Sørensen, and P Lodahl (2018). "Suppressing phonon decoherence of high performance single-photon sources in nanophotonic waveguides". *Quantum Science and Technology* **4**.1, 015003. DOI: `10.1088/2058-9565/aadbb8` (cited on p. 21).

DUQUENNOY, R., M. Colautti, R. Emadi, P. Majumder, P. Lombardi, and C. Toninelli (2022). "Real-time two-photon interference from distinct molecules on the same chip". *Optica* **9**.7, 731–737. DOI: `10.1364/OPTICA.452317` (cited on p. 57).

ELLIS, D. J. P., A. J. Bennett, C. Dangel, J. P. Lee, J. P. Griffiths, T. A. Mitchell, T.-K. Paraiso, P. Spencer, D. A. Ritchie, and A. J. Shields (2018). "Independent indistinguishable quantum light sources on a reconfigurable photonic integrated circuit". *Applied Physics Letters* **112**.21, 211104. DOI: `10.1063/1.5028339` (cited on p. 34).

ELSHAARI, A. W., I. E. Zadeh, A. Fognini, M. E. Reimer, D. Dalacu, P. J. Poole, V. Zwiller, and K. D. Jöns (2017). "On-chip single photon filtering and multiplexing in hybrid quantum photonic circuits". *Nature Communications* **8**.1, 379. DOI: `10.1038/s41467-017-00486-8` (cited on p. 33).

FEYNMAN, R. P. (1982). "Simulating physics with computers". *International Journal of Theoretical Physics* **21**.6, 467 (cited on p. 1).

FISCHER, K. A., L. Hanschke, M. Kremser, J. J. Finley, K. Müller, and J. Vučković (2017). "Pulsed Rabi oscillations in quantum two-level systems: beyond the area theorem". *Quantum Science and Technology* **3**.1, 014006. DOI: `10.1088/2058-9565/aa9269` (cited on p. 31).

FLAGG, E. B., A. Muller, J. W. Robertson, S. Founta, D. G. Deppe, M. Xiao, W. Ma, G. J. Salamo, and C. K. Shih (2009). "Resonantly driven coherent oscillations in a solid-state quantum emitter". *Nature Physics* **5**.3, 203–207. DOI: `10.1038/nphys1184` (cited on p. 68).

FLAGG, E. B., A. Muller, S. V. Polyakov, A. Ling, A. Migdall, and G. S. Solomon (2010). “Interference of Single Photons from Two Separate Semiconductor Quantum Dots”. *Phys. Rev. Lett.* **104** (13), 137401. DOI: `10.1103/PhysRevLett.104.137401` (cited on pp. 57, 73).

FLAMINI, F., N. Spagnolo, and F. Sciarrino (2018). “Photonic quantum information processing: a review”. *Reports on Progress in Physics* **82**.1, 016001. DOI: `10.1088/1361-6633/aad5b2` (cited on p. 5).

FLISSIKOWSKI, T., A. Hundt, M. Lowisch, M. Rabe, and F. Henneberger (2001). “Photon Beats from a Single Semiconductor Quantum Dot”. *Phys. Rev. Lett.* **86** (14), 3172–3175. DOI: `10.1103/PhysRevLett.86.3172` (cited on p. 68).

FOX, M. (2006). *Quantum optics: an introduction*. Oxford University Press (cited on p. 95).

GERBER, S, D Rotter, M Hennrich, R Blatt, F Rohde, C Schuck, M Almendros, R Gehr, F Dubin, and J Eschner (2009). “Quantum interference from remotely trapped ions”. *New Journal of Physics* **11**.1, 013032. DOI: `10.1088/1367-2630/11/1/013032` (cited on pp. 57, 70).

GIMENO-SEGOVIA, M., P. Shadbolt, D. E. Browne, and T. Rudolph (2015). “From Three-Photon Greenberger-Horne-Zeilinger States to Ballistic Universal Quantum Computation”. *Phys. Rev. Lett.* **115** (2), 020502. DOI: `10.1103/PhysRevLett.115.020502` (cited on p. 101).

GONZÁLEZ-RUIZ, E. M., S. K. Das, P. Lodahl, and A. S. Sørensen (2022). “Violation of Bell’s inequality with quantum-dot single-photon sources”. *Phys. Rev. A* **106** (1), 012222. DOI: `10.1103/PhysRevA.106.012222` (cited on pp. 21, 85, 100).

GONZÁLEZ-RUIZ, E. M., J. Rivera-Dean, M. F. B. Cenni, A. S. Sørensen, A. Acín, and E. Oudot (2022). *Device Independent Quantum Key Distribution with realistic single-photon source implementations*. DOI: `10.48550/ARXIV.2211.16472` (cited on p. 100).

GRIM, J. Q., A. S. Bracker, M. Zalalutdinov, S. G. Carter, A. C. Kozen, M. Kim, C. S. Kim, J. T. Mlack, M. Yakes, B. Lee, and D. Gammon (2019). “Scalable in operando strain tuning in nanophotonic waveguides enabling three-quantum-dot superradiance”. *Nature Materials* **18**.9, 963–969. DOI: `10.1038/s41563-019-0418-0` (cited on p. 34).

GROVER, L. K. (2001). “From Schrödinger’s equation to the quantum search algorithm”. *Pramana* **56**.2, 333 (cited on p. 1).

GUHA, B., F. Marsault, F. Cadiz, L. Morgenroth, V. Ulin, V. Berkovitz, A. Lemaître, C. Gomez, A. Amo, S. Combrié, B. Gérard, G. Leo, and I. Favero (2017). “Surface-enhanced gallium arsenide photonic resonator with quality factor of 6×10^6”. *Optica* **4**.2, 218–221. DOI: `10.1364/OPTICA.4.000218` (cited on p. 44).

HANSCHKE, L. et al. (2020). "Origin of Antibunching in Resonance Fluorescence". *Phys. Rev. Lett.* **125** (17), 170402. DOI: `10.1103/PhysRevLett.125.170402` (cited on p. 16).

HANSOM, J., C. H. H. Schulte, C. Matthiesen, M. J. Stanley, and M. Atatüre (2014). "Frequency stabilization of the zero-phonon line of a quantum dot via phonon-assisted active feedback". *Applied Physics Letters* **105**.17, 172107. DOI: `10.1063/1.4901045` (cited on p. 34).

HARRIS, N. C., G. R. Steinbrecher, M. Prabhu, Y. Lahini, J. Mower, D. Bunandar, C. Chen, F. N. C. Wong, T. Baehr-Jones, M. Hochberg, S. Lloyd, and D. Englund (2017). "Quantum transport simulations in a programmable nanophotonic processor". *Nature Photonics* **11**.7, 447–452. DOI: `10.1038/nphoton.2017.95` (cited on p. 2).

HÖGELE, A., S. Seidl, M. Kroner, K. Karrai, R. J. Warburton, B. D. Gerardot, and P. M. Petroff (2004). "Voltage-Controlled Optics of a Quantum Dot". *Phys. Rev. Lett.* **93** (21), 217401. DOI: `10.1103/PhysRevLett.93.217401` (cited on p. 24).

HONG, C. K., Z. Y. Ou, and L. Mandel (1987). "Measurement of subpicosecond time intervals between two photons by interference". *Phys. Rev. Lett.* **59** (18), 2044–2046. DOI: `10.1103/PhysRevLett.59.2044` (cited on p. 17).

HUH, J., G. G. Guerreschi, B. Peropadre, J. R. McClean, and A. Aspuru-Guzik (2015). "Boson sampling for molecular vibronic spectra". *Nature Photonics* **9**.9, 615–620. DOI: `10.1038/nphoton.2015.153` (cited on p. 2).

HUMMEL, T. (2019). *Multiphoton generation from a single quantum dot in a photonic nanostructure*. PhD thesis, University of Copenhagen (cited on pp. 91, 92).

HUMMEL, T., C. Ouellet-Plamondon, E. Ugur, I. Kulkova, T. Lund-Hansen, M. A. Broome, R. Uppu, and P. Lodahl (2019). "Efficient demultiplexed single-photon source with a quantum dot coupled to a nanophotonic waveguide". *Applied Physics Letters* **115**.2, 021102. DOI: `10.1063/1.5096979` (cited on p. 33).

JAVADI, A. (2015). *Quantum electrodynamics with 1D artificial atoms*. PhD thesis, University of Copenhagen (cited on p. 27).

JOANNOPOULOS, J. D., S. G. Johnson, J. N. Winn, and R. D. Meade (2008). *Photonic Crystals: Molding the Flow of Light - Second Edition*. REV - Revised, 2. Princeton University Press (cited on p. 26).

JOHANSEN, J., B. Julsgaard, S. Stobbe, J. M. Hvam, and P. Lodahl (2010). "Probing long-lived dark excitons in self-assembled quantum dots". *Phys. Rev. B* **81** (8), 081304. DOI: `10.1103/PhysRevB.81.081304` (cited on pp. 10, 69).

JOHANSSON, J., P. Nation, and F. Nori (2012). "QuTiP: An open-source Python framework for the dynamics of open quantum systems". *Computer Physics Communications* **183**.8, 1760–1772. DOI: `https://doi.org/10.1016/j.cpc.2012.02.021` (cited on p. 22).

JULSGAARD, B., J. Johansen, S. Stobbe, T. Stolberg-Rohr, T. Sünner, M. Kamp, A. Forchel, and P. Lodahl (2008). "Decay dynamics of quantum dots influenced by the local density of optical states of two-dimensional photonic crystal membranes". *Applied Physics Letters* **93**.9, 094102. DOI: `10.1063/1.2977605` (cited on p. 26).

KAKO, S., C. Santori, K. Hoshino, S. Götzinger, Y. Yamamoto, and Y. Arakawa (2006). "A gallium nitride single-photon source operating at 200K". *Nature Materials* **5**.11, 887–892. DOI: `10.1038/nmat1763` (cited on pp. 67, 81).

KAMBS, B. and C. Becher (2018). "Limitations on the indistinguishability of photons from remote solid state sources". *New Journal of Physics* **20**.11, 115003. DOI: `10.1088/1367-2630/aaea99` (cited on p. 101).

KIMBLE, H. J. (2008). "The quantum internet". *Nature* **453**.7198, 1023–1030. DOI: `10.1038/nature07127` (cited on p. 2).

KIRŠANSKĖ, G. et al. (2017). "Indistinguishable and efficient single photons from a quantum dot in a planar nanobeam waveguide". *Phys. Rev. B* **96** (16), 165306. DOI: `10.1103/PhysRevB.96.165306` (cited on pp. 24, 28, 54).

KITTEL, C. (2005). *Introduction to solid state physics*. 8th ed., John Wiley & Sons (cited on p. 6).

KNIGHT, P. and C. Gerry (2005). *Introductory quantum optics*. Cambridge University Press (cited on p. 89).

KNILL, E., R. Laflamme, and G. J. Milburn (2001). "A scheme for efficient quantum computation with linear optics". *nature* **409**.6816, 46–52 (cited on p. 1).

KONTHASINGHE, K., M. Peiris, Y. Yu, M. F. Li, J. F. He, L. J. Wang, H. Q. Ni, Z. C. Niu, C. K. Shih, and A. Muller (2012a). "Field-Field and Photon-Photon Correlations of Light Scattered by Two Remote Two-Level InAs Quantum Dots on the Same Substrate". *Phys. Rev. Lett.* **109** (26), 267402. DOI: `10.1103/PhysRevLett.109.267402` (cited on p. 21).

KONTHASINGHE, K., J. Walker, M. Peiris, C. K. Shih, Y. Yu, M. F. Li, J. F. He, L. J. Wang, H. Q. Ni, Z. C. Niu, and A. Muller (2012b). "Coherent versus incoherent light scattering from a quantum dot". *Phys. Rev. B* **85** (23), 235315. DOI: `10.1103/PhysRevB.85.235315` (cited on p. 22).

KOTAL, S., A. Artioli, Y. Wang, A. D. Osterkryger, M. Finazzer, R. Fons, Y. Genuist, J. Bleuse, J.-M. Gérard, N. Gregersen, and J. Claudon (2021).

"A nanowire optical nanocavity for broadband enhancement of spontaneous emission". *Applied Physics Letters* **118**.19, 194002. DOI: `10.1063/5.004583` (cited on p. 33).

KUHLMANN, A. V., J. H. Prechtel, J. Houel, A. Ludwig, D. Reuter, A. D. Wieck, and R. J. Warburton (2015). "Transform-limited single photons from a single quantum dot". *Nature Communications* **6**.1, 8204. DOI: `10.1038/ncomms9204` (cited on pp. 21, 22, 33).

KURUMA, K., Y. Ota, M. Kakuda, S. Iwamoto, and Y. Arakawa (2020). "Surface-passivated high-Q GaAs photonic crystal nanocavity with quantum dots". *APL Photonics* **5**.4, 046106. DOI: `10.1063/1.5144959`. eprint: `https://doi.org/10.1063/1.5144959` (cited on p. 45).

LE JEANNIC, H., T. Ramos, S. F. Simonsen, T. Pregnolato, Z. Liu, R. Schott, A. D. Wieck, A. Ludwig, N. Rotenberg, J. J. García-Ripoll, and P. Lodahl (2021). "Experimental Reconstruction of the Few-Photon Nonlinear Scattering Matrix from a Single Quantum Dot in a Nanophotonic Waveguide". *Phys. Rev. Lett.* **126** (2), 023603. DOI: `10.1103/PhysRevLett.126.023603` (cited on p. 86).

LEE, S. et al. (2022). *Is there evidence for exponential quantum advantage in quantum chemistry?* DOI: `10.48550/ARXIV.2208.02199` (cited on p. 1).

LEGERO, T., T. Wilk, A. Kuhn, and G. Rempe (2003). "Time-resolved two-photon quantum interference". *Applied Physics B* **77**.8, 797–802. DOI: `10.1007/s00340-003-1337-x` (cited on p. 17).

LENZINI, F., B. Haylock, J. C. Loredo, R. A. Abrahão, N. A. Zakaria, S. Kasture, I. Sagnes, A. Lemaitre, H.-P. Phan, D. V. Dao, P. Senellart, M. P. Almeida, A. G. White, and M. Lobino (2017). "Active demultiplexing of single photons from a solid-state source". *Laser & Photonics Reviews* **11**.3, 1600297. DOI: `https://doi.org/10.1002/lpor.201600297` (cited on p. 33).

LETTOW, R., Y. L. A. Rezus, A. Renn, G. Zumofen, E. Ikonen, S. Götzinger, and V. Sandoghdar (2010). "Quantum Interference of Tunably Indistinguishable Photons from Remote Organic Molecules". *Phys. Rev. Lett.* **104** (12), 123605. DOI: `10.1103/PhysRevLett.104.123605` (cited on pp. 57, 69, 70).

LI, B., S. E. Economou, and E. Barnes (2022). "Photonic resource state generation from a minimal number of quantum emitters". *npj Quantum Information* **8**.1, 11. DOI: `10.1038/s41534-022-00522-6` (cited on p. 3).

LIU, J., K. Konthasinghe, M. Davanço, J. Lawall, V. Anant, V. Verma, R. Mirin, S. W. Nam, J. D. Song, B. Ma, Z. S. Chen, H. Q. Ni, Z. C. Niu, and K. Srinivasan (2018). "Single Self-Assembled InAs/GaAs Quantum Dots in Photonic Nanostructures: The Role of Nanofabrication". *Phys. Rev. Applied* **9** (6), 064019. DOI: `10.1103/PhysRevApplied.9.064019` (cited on p. 21).

LIU, J., G. Huang, R. N. Wang, J. He, A. S. Raja, T. Liu, N. J. Engelsen, and T. J. Kippenberg (2021). “High-yield, wafer-scale fabrication of ultralow-loss, dispersion-engineered silicon nitride photonic circuits”. *Nature Communications* **12**.1, 2236. DOI: `10.1038/s41467-021-21973-z` (cited on p. 42).

LÖBL, M. C., S. Scholz, I. Söllner, J. Ritzmann, T. Denneulin, A. Kovács, B. E. Kardynał, A. D. Wieck, A. Ludwig, and R. J. Warburton (2019). “Excitons in InGaAs quantum dots without electron wetting layer states”. *Communications Physics* **2**.1, 93. DOI: `10.1038/s42005-019-0194-9` (cited on p. 9).

LÖBL, M. C., I. Söllner, A. Javadi, T. Pregnolato, R. Schott, L. Midolo, A. V. Kuhlmann, S. Stobbe, A. D. Wieck, P. Lodahl, A. Ludwig, and R. J. Warburton (2017). “Narrow optical linewidths and spin pumping on charge-tunable close-to-surface self-assembled quantum dots in an ultrathin diode”. *Phys. Rev. B* **96** (16), 165440. DOI: `10.1103/PhysRevB.96.165440` (cited on p. 23).

LODAHL, P., A. Ludwig, and R. J. Warburton (2022). “A deterministic source of single photons”. *Physics Today* **75**.3, 44–50. DOI: `10.1063/PT.3.4962` (cited on p. 2).

LODAHL, P., S. Mahmoodian, and S. Stobbe (2015). “Interfacing single photons and single quantum dots with photonic nanostructures”. *Rev. Mod. Phys.* **87** (2), 347–400. DOI: `10.1103/RevModPhys.87.347` (cited on pp. 9, 10, 25).

LOMONTE, E., M. A. Wolff, F. Beutel, S. Ferrari, C. Schuck, W. H. P. Pernice, and F. Lenzini (2021). “Single-photon detection and cryogenic reconfigurability in lithium niobate nanophotonic circuits”. *Nature Communications* **12**.1, 6847. DOI: `10.1038/s41467-021-27205-8` (cited on p. 2).

LUO, Y., Z. Nong, S. Gao, H. Huang, Y. Zhu, L. Liu, L. Zhou, J. Xu, L. Liu, S. Yu, and X. Cai (2018). “Low-loss two-dimensional silicon photonic grating coupler with a backside metal mirror”. *Opt. Lett.* **43**.3, 474–477. DOI: `10.1364/OL.43.000474` (cited on p. 49).

MADSEN, L. S. et al. (2022). “Quantum computational advantage with a programmable photonic processor”. *Nature* **606**.7912, 75–81. DOI: `10.1038/s41586-022-04725-x` (cited on p. 2).

MAHMOODIAN, S., P. Lodahl, and A. S. Sørensen (2016). “Quantum Networks with Chiral-Light–Matter Interaction in Waveguides”. *Phys. Rev. Lett.* **117** (24), 240501. DOI: `10.1103/PhysRevLett.117.240501` (cited on p. 101).

MAKHONIN, M. N., J. E. Dixon, R. J. Coles, B. Royall, I. J. Luxmoore, E. Clarke, M. Hugues, M. S. Skolnick, and A. M. Fox (2014). “Waveguide Coupled Resonance Fluorescence from On-Chip Quantum Emitter”. *Nano Letters* **14**.12, 6997–7002. DOI: `10.1021/nl5032937` (cited on p. 15).

MATTHIESEN, C., A. N. Vamivakas, and M. Atatüre (2012). "Subnatural Linewidth Single Photons from a Quantum Dot". *Phys. Rev. Lett.* **108** (9), 093602. DOI: `10.1103/PhysRevLett.108.093602` (cited on p. 15).

MEYSTRE, P. and M. Sargent (2007). *Elements of quantum optics*. Springer Berlin Heidelberg (cited on pp. 12, 13).

MICHLER, P., A. Kiraz, C. Becher, W. V. Schoenfeld, P. M. Petroff, L. Zhang, E. Hu, and A. Imamoğlu (2000). "A Quantum Dot Single-Photon Turnstile Device". *Science* **290**.5500, 2282–2285. DOI: `10.1126/science.290.5500.2282` (cited on p. 30).

MICHLER, P. (2017). *Quantum dots for quantum information technologies*. Springer (cited on pp. 15, 30, 66).

MIDOLO, L., T. Pregnolato, G. Kiršanskė, and S. Stobbe (2015). "Soft-mask fabrication of gallium arsenide nanomembranes for integrated quantum photonics". *Nanotechnology* **26**.48, 484002. DOI: `10.1088/0957-4484/26/48/484002` (cited on p. 39).

MIKKELSEN, M. T. (2021). *Multiphoton and heralded entanglement sources for applications in quantum cryptography*. Msc thesis, University of Copenhagen (cited on p. 91).

MOODY, G. et al. (2022). "2022 Roadmap on integrated quantum photonics". *Journal of Physics: Photonics* **4**.1, 012501. DOI: `10.1088/2515-7647/ac1ef4` (cited on p. 3).

MULLER, A. (2007). *Resonance Fluorescence and Cavity Quantum Electrodynamics with Quantum Dots*. Ph.D. thesis, University of Texas at Austin (cited on pp. 11, 14, 16).

NIELSEN, M. A. (2004). "Optical Quantum Computation Using Cluster States". *Phys. Rev. Lett.* **93** (4), 040503. DOI: `10.1103/PhysRevLett.93.040503` (cited on p. 2).

O'BRIEN, J. L., A. Furusawa, and J. Vučković (2009). "Photonic quantum technologies". *Nature Photonics* **3**.12, 687–695. DOI: `10.1038/nphoton.2009.229` (cited on p. 1).

OCOLA, L. E. and A. Stein (2006). "Effect of cold development on improvement in electron-beam nanopatterning resolution and line roughness". *Journal of Vacuum Science & Technology B: Microelectronics and Nanometer Structures Processing, Measurement, and Phenomena* **24**.6, 3061–3065. DOI: `10.1116/1.2366698` (cited on p. 40).

OLISLAGER, L., J. Safioui, S. Clemmen, K. P. Huy, W. Bogaerts, R. Baets, P. Emplit, and S. Massar (2013). "Silicon-on-insulator integrated source of polarization-entangled photons". *Opt. Lett.* **38**.11, 1960–1962. DOI: `10.1364/OL.38.001960` (cited on p. 49).

OLLIVIER, H., S. E. Thomas, S. C. Wein, I. M. de Buy Wenniger, N. Coste, J. C. Loredo, N. Somaschi, A. Harouri, A. Lemaitre, I. Sagnes, L. Lanco, C. Simon, C. Anton, O. Krebs, and P. Senellart (2021). "Hong-Ou-Mandel Interference with Imperfect Single Photon Sources". *Phys.*

Rev. Lett. **126** (6), 063602. DOI: 10.1103/PhysRevLett.126.063602 (cited on pp. 31, 84).

OLLIVIER, H. et al. (2020). "Reproducibility of High-Performance Quantum Dot Single-Photon Sources". *ACS Photonics* **7**.4, 1050–1059. DOI: 10.1021/acsphotonics.9b01805 (cited on p. 34).

OSKOOI, A. F., D. Roundy, M. Ibanescu, P. Bermel, J. Joannopoulos, and S. G. Johnson (2010). "Meep: A flexible free-software package for electromagnetic simulations by the FDTD method". *Computer Physics Communications* **181**.3, 687–702. DOI: https://doi.org/10.1016/j.cpc.2009.11.008 (cited on p. 29).

ØSTFELDT, F. T., E. M. González-Ruiz, N. Hauff, Y. Wang, A. D. Wieck, A. Ludwig, R. Schott, L. Midolo, A. S. Sørensen, R. Uppu, and P. Lodahl (2022). "On-Demand Source of Dual-Rail Photon Pairs Based on Chiral Interaction in a Nanophotonic Waveguide". *PRX Quantum* **3** (2), 020363. DOI: 10.1103/PRXQuantum.3.020363 (cited on p. 10).

PAPON, C., Y. Wang, R. Uppu, S. Scholz, A. D. Wieck, A. Ludwig, P. Lodahl, and L. Midolo (2022). *Independent operation of two waveguide-integrated single-photon sources*. DOI: 10.48550/ARXIV.2210.09826 (cited on p. 98).

PAPON, C., X. Zhou, H. Thyrrestrup, Z. Liu, S. Stobbe, R. Schott, A. D. Wieck, A. Ludwig, P. Lodahl, and L. Midolo (2019). "Nanomechanical single-photon routing". *Optica* **6**.4, 524–530. DOI: 10.1364/OPTICA.6.000524 (cited on pp. 43, 48, 76, 88, 95, 100).

PARRAIN, D., C. Baker, G. Wang, B. Guha, E. G. Santos, A. Lemaitre, P. Senellart, G. Leo, S. Ducci, and I. Favero (2015). "Origin of optical losses in gallium arsenide disk whispering gallery resonators". *Opt. Express* **23**.15, 19656–19672. DOI: 10.1364/OE.23.019656 (cited on p. 44).

PATEL, R. B., A. J. Bennett, I. Farrer, C. A. Nicoll, D. A. Ritchie, and A. J. Shields (2010). "Two-photon interference of the emission from electrically tunable remote quantum dots". *Nature Photonics* **4**.9, 632–635. DOI: 10.1038/nphoton.2010.161 (cited on pp. 57, 69, 70).

PEDERSEN, F. T., Y. Wang, C. T. Olesen, S. Scholz, A. D. Wieck, A. Ludwig, M. C. Löbl, R. J. Warburton, L. Midolo, R. Uppu, and P. Lodahl (2020). "Near Transform-Limited Quantum Dot Linewidths in a Broadband Photonic Crystal Waveguide". *ACS Photonics* **7**.9, 2343–2349. DOI: 10.1021/acsphotonics.0c00758 (cited on pp. 34, 52, 53).

PEDERSEN, F. T. (2020). *Deterministic single and multi-photon sources with quantum dots in planar nanostructures*. PhD thesis, University of Copenhagen (cited on pp. 58, 59, 83).

PERUZZO, A., J. McClean, P. Shadbolt, M.-H. Yung, X.-Q. Zhou, P. J. Love, A. Aspuru-Guzik, and J. L. O'Brien (2014). "A variational eigenvalue solver on a photonic quantum processor". *Nature Communications* **5**.1, 4213. DOI: 10.1038/ncomms5213 (cited on p. 2).

PETRUZZELLA, M., S. Birindelli, F. M. Pagliano, D. Pellegrino, v. Zobenica, L. H. Li, E. H. Linfield, and A. Fiore (2018). "Quantum photonic integrated circuits based on tunable dots and tunable cavities". *APL Photonics* **3**.10, 106103. DOI: 10.1063/1.5039961 (cited on p. 34).

PITA RUIZ, J. L., L. G. Rocha, J. Yang, c. E. Kocabaş, M.-J. Li, I. Aldaya, M. Ménard, P. Dainese, and L. H. Gabrielli (2022). "Ultracompact Silicon-On-Insulator Couplers for Multicore Fibers". *ACS Photonics* **0**.0, 0. DOI: 10.1021/acsphotonics.2c01008 (cited on p. 100).

PRABHU, M., C. Errando-Herranz, L. De Santis, I. Christen, C. Chen, and D. R. Englund (2022). *Individually Addressable Artificial Atoms in Silicon Photonics*. DOI: 10.48550/ARXIV.2202.02342 (cited on p. 101).

PREGNOLATO, T., X.-L. Chu, T. Schröder, R. Schott, A. D. Wieck, A. Ludwig, P. Lodahl, and N. Rotenberg (2020). "Deterministic positioning of nanophotonic waveguides around single self-assembled quantum dots". *APL Photonics* **5**.8, 086101. DOI: 10.1063/1.5117888 (cited on p. 34).

PREGNOLATO, T. (2019). *Deterministic qantum photonic devices based on self-assembled quantum dots*. PhD thesis, University of Copenhagen (cited on p. 75).

PRESKILL, J. (2022). *The Physics of Quantum Information*. DOI: 10.48550/ARXIV.2208.08064 (cited on p. 1).

PRINDAL-NIELSEN, K. (2017). *Light matter interaction in nanobeam waveguides*. Msc thesis, University of Copenhagen (cited on p. 28).

PROUX, R., M. Maragkou, E. Baudin, C. Voisin, P. Roussignol, and C. Diederichs (2015). "Measuring the Photon Coalescence Time Window in the Continuous-Wave Regime for Resonantly Driven Semiconductor Quantum Dots". *Phys. Rev. Lett.* **114** (6), 067401. DOI: 10.1103/PhysRevLett.114.067401 (cited on pp. 72, 73).

PU, M., L. Ottaviano, E. Semenova, and K. Yvind (2016). "Efficient frequency comb generation in AlGaAs-on-insulator". *Optica* **3**.8, 823–826. DOI: 10.1364/OPTICA.3.000823 (cited on p. 44).

RAMSAY, A. J., A. V. Gopal, E. M. Gauger, A. Nazir, B. W. Lovett, A. M. Fox, and M. S. Skolnick (2010). "Damping of Exciton Rabi Rotations by Acoustic Phonons in Optically Excited InGaAs/GaAs Quantum Dots". *Phys. Rev. Lett.* **104** (1), 017402. DOI: 10.1103/PhysRevLett.104.017402 (cited on pp. 21, 81).

RAUSSENDORF, R. and H. J. Briegel (2001). "A One-Way Quantum Computer". *Phys. Rev. Lett.* **86** (22), 5188–5191. DOI: 10.1103/PhysRevLett.86.5188 (cited on p. 2).

REINDL, M., K. D. Jöns, D. Huber, C. Schimpf, Y. Huo, V. Zwiller, A. Rastelli, and R. Trotta (2017). "Phonon-Assisted Two-Photon Interference from Remote Quantum Emitters". *Nano Letters* **17**.7. PMID: 28557459, 4090–4095. DOI: `10.1021/acs.nanolett.7b00777` (cited on p. 57).

REITHMAIER, G., M. Kaniber, F. Flassig, S. Lichtmannecker, K. Müller, A. Andrejew, J. Vučković, R. Gross, and J. J. Finley (2015). "On-Chip Generation, Routing, and Detection of Resonance Fluorescence". *Nano Letters* **15**.8. PMID: 26102603, 5208–5213. DOI: `10.1021/acs.nanolett.5b01444` (cited on p. 42).

ROELKENS, G., D. Vermeulen, F. Van Laere, S. Selvaraja, S. Scheerlinck, D. Taillaert, W. Bogaerts, P. Dumon, D. Van Thourhout, and R. Baets (2010). "Bridging the gap between nanophotonic waveguide circuits and single mode optical fibers using diffractive grating structures". *J Nanosci Nanotechnol* **10**.3, 1551–1562 (cited on p. 49).

ROTENBERG, N., P. Türschmann, H. R. Haakh, D. Martin-Cano, S. Götzinger, and V. Sandoghdar (2017). "Small slot waveguide rings for on-chip quantum optical circuits". *Opt. Express* **25**.5, 5397–5414. DOI: `10.1364/OE.25.005397` (cited on p. 29).

RUDOLPH, T. (2017). "Why I am optimistic about the silicon-photonic route to quantum computing". *APL Photonics* **2**.3, 030901. DOI: `10.1063/1.4976737`. eprint: `https://doi.org/10.1063/1.4976737` (cited on p. 2).

SANTORI, C., D. Fattal, J. Vučković, G. S. Solomon, and Y. Yamamoto (2002). "Indistinguishable photons from a single-photon device". *Nature* **419**.6907, 594–597. DOI: `10.1038/nature01086` (cited on pp. 30, 31, 84).

SANTORI, C., D. Fattal, and Y. Yamamoto (2010). *Single-photon devices and applications*. Wiley (cited on p. 20).

SBRESNY, F., L. Hanschke, E. Schöll, W. Rauhaus, B. Scaparra, K. Boos, E. Zubizarreta Casalengua, H. Riedl, E. del Valle, J. J. Finley, K. D. Jöns, and K. Müller (2022). "Stimulated Generation of Indistinguishable Single Photons from a Quantum Ladder System". *Phys. Rev. Lett.* **128** (9), 093603. DOI: `10.1103/PhysRevLett.128.093603` (cited on p. 24).

SCHOFIELD, R. C., C. Clear, R. A. Hoggarth, K. D. Major, D. P. S. McCutcheon, and A. S. Clark (2022). "Photon indistinguishability measurements under pulsed and continuous excitation". *Phys. Rev. Research* **4** (1), 013037. DOI: `10.1103/PhysRevResearch.4.013037` (cited on p. 73).

SCHWARTZ, M., U. Rengstl, T. Herzog, M. Paul, J. Kettler, S. L. Portalupi, M. Jetter, and P. Michler (2016). "Generation, guiding and splitting of triggered single photons from a resonantly excited quantum dot in a photonic circuit". *Opt. Express* **24**.3, 3089–3094. DOI: `10.1364/OE.24.003089` (cited on pp. 10, 73).

SCHWARTZ, M., E. Schmidt, U. Rengstl, F. Hornung, S. Hepp, S. L. Portalupi, K. llin, M. Jetter, M. Siegel, and P. Michler (2018). "Fully On-Chip Single-Photon Hanbury-Brown and Twiss Experiment on a Monolithic Semiconductor–Superconductor Platform". *Nano Letters* **18**.11, 6892–6897. DOI: 10.1021/acs.nanolett.8b02794 (cited on p. 67).

SCULLY, M. O. and M. S. Zubairy (1997). *Quantum Optics*. Cambridge University Press. DOI: 10.1017/CBO9780511813993 (cited on pp. 11, 70).

SHADMANI, A., R. A. Thomas, Z. Liu, C. Papon, M. J. R. Heck, N. Volet, S. Scholz, A. D. Wieck, A. Ludwig, P. Lodahl, and L. Midolo (2022). "Integration of GaAs waveguides on a silicon substrate for quantum photonic circuits". *Opt. Express* **30**.21, 37595–37602. DOI: 10.1364/OE.467920 (cited on pp. 43, 97, 100).

SHOR, P. (1997). "Polynomial-time algorithms for prime factorization and discrete logarithms on a quantum computer". *SIAM Journal of Computing* **26**, 1484–1509 (cited on p. 1).

SOMASCHI, N., V. Giesz, L. De Santis, J. Loredo, M. P. Almeida, G. Hornecker, S. L. Portalupi, T. Grange, C. Anton, J. Demory, et al. (2016). "Near-optimal single-photon sources in the solid state". *Nature Photonics* **10**.5, 340–345. DOI: 10.1038/nphoton.2016.23 (cited on p. 33).

SPARROW, C., E. Martín-López, N. Maraviglia, A. Neville, C. Harrold, J. Carolan, Y. N. Joglekar, T. Hashimoto, N. Matsuda, J. L. O'Brien, D. P. Tew, and A. Laing (2018). "Simulating the vibrational quantum dynamics of molecules using photonics". *Nature* **557**.7707, 660–667. DOI: 10.1038/s41586-018-0152-9 (cited on p. 2).

STECK, D. A. (2007). *Quantum and Atom Optics*. Department of Physics, University of Oregon (cited on p. 13).

SUND, P. I., E. Lomonte, S. Paesani, Y. Wang, J. Carolan, N. Bart, A. D. Wieck, A. Ludwig, L. Midolo, W. H. P. Pernice, P. Lodahl, and F. Lenzini (2022). *High-speed thin-film lithium niobate quantum processor driven by a solid-state quantum emitter*. DOI: 10.48550/ARXIV.2211.05703 (cited on p. 100).

SZE, S. M. and K. N. Kwok (2007). *Physics of Semiconductor Devices*. Third Edition, John Wiley & Sons, Hoboken. DOI: 10.1002/0470068329 (cited on pp. 5, 6, 47).

TAFLOVE, A. and S. Hagness (2005). *Computational Electrodynamics: The Finite-Difference Time-Domain Method*. Artech: Norwood, MA. DOI: 10.1016/B978-012170960-0/50046-3 (cited on p. 29).

THOMAS, S. E. et al. (2021). "Bright Polarized Single-Photon Source Based on a Linear Dipole". *Phys. Rev. Lett.* **126** (23), 233601. DOI: 10.1103/PhysRevLett.126.233601 (cited on pp. 21, 24).

THYRRESTRUP, H. et al. (2018). "Quantum Optics with Near-Lifetime-Limited Quantum-Dot Transitions in a Nanophotonic Waveguide". *Nano*

Letters **18**.3, 1801–1806. DOI: `10.1021/acs.nanolett.7b05016` (cited on pp. 28, 33, 85).

TICHY, M. C. (2014). "Interference of identical particles from entanglement to boson-sampling". *Journal of Physics B: Atomic, Molecular and Optical Physics* **47**.10, 103001. DOI: `10.1088/0953-4075/47/10/103001` (cited on p. 93).

TIGHINEANU, P., C. L. Dreeßen, C. Flindt, P. Lodahl, and A. S. Sørensen (2018). "Phonon Decoherence of Quantum Dots in Photonic Structures: Broadening of the Zero-Phonon Line and the Role of Dimensionality". *Phys. Rev. Lett.* **120** (25), 257401. DOI: `10.1103/PhysRevLett.120.257401` (cited on pp. 21, 57).

TIRANOV, A., V. Angelopoulou, C. J. van Diepen, B. Schrinski, O. A. D. Sandberg, Y. Wang, L. Midolo, S. Scholz, A. D. Wieck, A. Ludwig, A. S. Sørensen, and P. Lodahl (2022). *Coherent super- and subradiant dynamics between distant optical quantum emitters*. DOI: `10.48550/ARXIV.2210.02439` (cited on p. 101).

TOMM, N., A. Javadi, N. O. Antoniadis, D. Najer, M. C. Löbl, A. R. Korsch, R. Schott, S. R. Valentin, A. D. Wieck, A. Ludwig, and R. J. Warburton (2021). "A bright and fast source of coherent single photons". *Nature Nanotechnology* **16**.4, 399–403. DOI: `10.1038/s41565-020-00831-x` (cited on p. 32).

TÜRSCHMANN, P., H. L. Jeannic, S. F. Simonsen, H. R. Haakh, S. Götzinger, V. Sandoghdar, P. Lodahl, and N. Rotenberg (2019). "Coherent nonlinear optics of quantum emitters in nanophotonic waveguides". *Nanophotonics* **8**.10, 1641–1657. DOI: `doi:10.1515/nanoph-2019-0126` (cited on p. 85).

UPPU, R., H. T. Eriksen, H. Thyrrestrup, A. D. Uğurlu, Y. Wang, S. Scholz, A. D. Wieck, A. Ludwig, M. C. Löbl, R. J. Warburton, P. Lodahl, and L. Midolo (2020a). "On-chip deterministic operation of quantum dots in dual-mode waveguides for a plug-and-play single-photon source". *Nature Communications* **11**.1, 3782. DOI: `10.1038/s41467-020-17603-9` (cited on pp. 3, 29, 34–36, 59, 61, 69, 75, 85).

UPPU, R., L. Midolo, X. Zhou, J. Carolan, and P. Lodahl (2021). "Quantum-dot-based deterministic photon-emitter interfaces for scalable technology". *Nature Nanotechnology* **16**.12, 1308–1317. DOI: `10.1038/s41565-021-00965-6` (cited on p. 3).

UPPU, R., F. T. Pedersen, Y. Wang, C. T. Olesen, C. Papon, X. Zhou, L. Midolo, S. Scholz, A. D. Wieck, A. Ludwig, and P. Lodahl (2020b). "Scalable integrated single-photon source". *Science Advances* **6**.50, eabc8268. DOI: `10.1126/sciadv.abc8268` (cited on pp. 20, 21, 27, 30, 31, 33, 47, 54, 59, 63, 64, 97).

UĞURLU, A. D. (2021). *Novel optical polymer-based interfaces to quantum photonic integrated circuits*. PhD thesis, University of Copenhagen (cited on pp. 36, 73, 75–77, 88, 98).

UĞURLU, A. D., H. Thyrrestrup, R. Uppu, C. Ouellet-Plamondon, R. Schott, A. D. Wieck, A. Ludwig, P. Lodahl, and L. Midolo (2020). "Suspended Spot-Size Converters for Scalable Single-Photon Devices". *Advanced Quantum Technologies* **3**.2, 1900076. DOI: `https://doi.org/10.1002/qute.201900076` (cited on p. 45).

VANLAERE, F., W. Bogaerts, P. Dumon, G. Roelkens, D. VanThourhout, and R. Baets (2009). "Focusing Polarization Diversity Grating Couplers in Silicon-on-Insulator". *J. Lightwave Technol.* **27**.5, 612–618 (cited on p. 49).

VURAL, H., S. L. Portalupi, and P. Michler (2020). "Perspective of self-assembled InGaAs quantum-dots for multi-source quantum implementations". *Applied Physics Letters* **117**.3, 030501. DOI: `10.1063/5.0010782` (cited on p. 3).

WAN, N. H., T.-J. Lu, K. C. Chen, M. P. Walsh, M. E. Trusheim, L. De Santis, E. A. Bersin, I. B. Harris, S. L. Mouradian, I. R. Christen, E. S. Bielejec, and D. Englund (2020). "Large-scale integration of artificial atoms in hybrid photonic circuits". *Nature* **583**.7815, 226–231. DOI: `10.1038/s41586-020-2441-3` (cited on pp. 33, 100).

WANG, H., J. Qin, X. Ding, M.-C. Chen, S. Chen, X. You, Y.-M. He, X. Jiang, L. You, Z. Wang, C. Schneider, J. J. Renema, S. Höfling, C.-Y. Lu, and J.-W. Pan (2019a). "Boson Sampling with 20 Input Photons and a 60-Mode Interferometer in a 10^{14}-Dimensional Hilbert Space". *Phys. Rev. Lett.* **123** (25), 250503. DOI: `10.1103/PhysRevLett.123.250503` (cited on pp. 30, 33).

WANG, H. et al. (2019b). "Towards optimal single-photon sources from polarized microcavities". *Nature Photonics* **13**.11, 770–775. DOI: `10.1038/s41566-019-0494-3` (cited on p. 32).

WANG, J., D. Bonneau, M. Villa, J. W. Silverstone, R. Santagati, S. Miki, T. Yamashita, M. Fujiwara, M. Sasaki, H. Terai, M. G. Tanner, C. M. Natarajan, R. H. Hadfield, J. L. O'Brien, and M. G. Thompson (2016). "Chip-to-chip quantum photonic interconnect by path-polarization interconversion". *Optica* **3**.4, 407–413. DOI: `10.1364/OPTICA.3.000407` (cited on p. 49).

WANG, J., F. Sciarrino, A. Laing, and M. G. Thompson (2020). "Integrated photonic quantum technologies". *Nature Photonics* **14**.5, 273–284. DOI: `10.1038/s41566-019-0532-1` (cited on p. 2).

WANG, J. et al. (2014). "Gallium arsenide (GaAs) quantum photonic waveguide circuits". *Optics Communications* **327**. Special Issue on Nonlinear Quantum Photonics, 49–55. DOI: `https://doi.org/10.1016/j.optcom.2014.02.040` (cited on p. 95).

WANG, J., Y. Xuan, M. Qi, H. Huang, Y. Li, M. Li, X. Chen, Z. Sheng, A. Wu, W. Li, X. Wang, S. Zou, and F. Gan (2015). "Broadband and fabrication-tolerant on-chip scalable mode-division multiplexing based on mode-evolution counter-tapered couplers". *Opt. Lett.* **40**.9, 1956–1959. DOI: `10.1364/OL.40.001956` (cited on p. 76).

WANG, Q., S. Stobbe, and P. Lodahl (2011). "Mapping the Local Density of Optical States of a Photonic Crystal with Single Quantum Dots". *Phys. Rev. Lett.* **107** (16), 167404. DOI: `10.1103/PhysRevLett.107.167404` (cited on p. 9).

WANG, Y. (2021). *Novel nanofabrication methods and processes for quantum photonic integrated circuits*. PhD thesis, University of Copenhagen (cited on pp. 41, 47, 49).

WANG, Y., R. Uppu, X. Zhou, C. Papon, S. Scholz, A. D. Wieck, A. Ludwig, P. Lodahl, and L. Midolo (2021). "Electroabsorption in gated GaAs nanophotonic waveguides". *Applied Physics Letters* **118**.13, 131106. DOI: `10.1063/5.0039373`. eprint: `https://doi.org/10.1063/5.0039373` (cited on pp. 44, 97).

WARBURTON, R. J., C. Schulhauser, D. Haft, C. Schäflein, K. Karrai, J. M. Garcia, W. Schoenfeld, and P. M. Petroff (2002). "Giant permanent dipole moments of excitons in semiconductor nanostructures". *Phys. Rev. B* **65** (11), 113303. DOI: `10.1103/PhysRevB.65.113303` (cited on p. 23).

WARBURTON, R. J. (2013). "Single spins in self-assembled quantum dots". *Nature Materials* **12**.6, 483–493. DOI: `10.1038/nmat3585` (cited on pp. 2, 10, 23, 24).

WEBER, J. H., B. Kambs, J. Kettler, S. Kern, J. Maisch, H. Vural, M. Jetter, S. L. Portalupi, C. Becher, and P. Michler (2019). "Two-photon interference in the telecom C-band after frequency conversion of photons from remote quantum emitters". *Nature Nanotechnology* **14**.1, 23–26. DOI: `10.1038/s41565-018-0279-8` (cited on p. 57).

WOOLLEY, M. J., C Lang, C Eichler, A Wallraff, and A Blais (2013). "Signatures of Hong–Ou–Mandel interference at microwave frequencies". *New Journal of Physics* **15**.10, 105025. DOI: `10.1088/1367-2630/15/10/105025` (cited on pp. 17, 70).

YUAN, X., F. Weyhausen-Brinkmann, J. Martín-Sánchez, G. Piredda, V. Křápek, Y. Huo, H. Huang, C. Schimpf, O. G. Schmidt, J. Edlinger, G. Bester, R. Trotta, and A. Rastelli (2018). "Uniaxial stress flips the natural quantization axis of a quantum dot for integrated quantum photonics". *Nature Communications* **9**.1, 3058. DOI: `10.1038/s41467-018-05499-5` (cited on p. 26).

ZABEL, H. and M. Farle (2013). *Magnetic Nanostructures*. Springer (cited on p. 8).

ZHAI, L., G. N. Nguyen, C. Spinnler, J. Ritzmann, M. C. Löbl, A. D. Wieck, A. Ludwig, A. Javadi, and R. J. Warburton (2022). "Quantum interference of identical photons from remote GaAs quantum dots". *Nature Nanotechnology* **17**.8, 829–833. DOI: `10.1038/s41565-022-01131-2` (cited on pp. 57, 101).

ZHANG, Q., X.-H. Bao, C.-Y. Lu, X.-Q. Zhou, T. Yang, T. Rudolph, and J.-W. Pan (2008). "Demonstration of a scheme for the generation of "event-ready" entangled photon pairs from a single-photon source". *Phys. Rev. A* **77** (6), 062316. DOI: `10.1103/PhysRevA.77.062316` (cited on p. 91).

ZHONG, H.-S. et al. (2020). "Quantum computational advantage using photons". *Science* **370**.6523, 1460–1463. DOI: `10.1126/science.abe8770` (cited on pp. 2, 33).

ZHOU, X., I. Kulkova, T. Lund-Hansen, S. L. Hansen, P. Lodahl, and L. Midolo (2018). "High-efficiency shallow-etched grating on GaAs membranes for quantum photonic applications". *Applied Physics Letters* **113**.25, 251103. DOI: `10.1063/1.5055622` (cited on pp. 31, 45–47, 49, 50, 54, 97).

ZHOU, X., P. Lodahl, and L. Midolo (2022). "In-plane resonant excitation of quantum dots in a dual-mode photonic-crystal waveguide with high β-factor". *Quantum Science and Technology* **7**.2, 025023. DOI: `10.1088/2058-9565/ac5918` (cited on p. 100).

ZHOU, X., R. Uppu, Z. Liu, C. Papon, R. Schott, A. D. Wieck, A. Ludwig, P. Lodahl, and L. Midolo (2020). "On-Chip Nanomechanical Filtering of Quantum-Dot Single-Photon Sources". *Laser & Photonics Reviews* **14**.7, 1900404. DOI: `https://doi.org/10.1002/lpor.201900404` (cited on p. 100).

ZIELIǸSKI, M. (2021). "Dark-bright excitons mixing in alloyed InGaAs self-assembled quantum dots". *Phys. Rev. B* **103** (15), 155418. DOI: `10.1103/PhysRevB.103.155418` (cited on p. 9).